



Hydrodynamic excitations in a Bose-Einstein condensate

Robert Meppelink

ROBERT MEPPELINK

HYDRODYNAMIC EXCITATIONS
IN A BOSE-EINSTEIN CONDENSATE

Meppelink, Robert

Hydrodynamic excitations in a Bose-Einstein condensate

R. Meppelink - Utrecht

Universiteit Utrecht

Faculteit Bètawetenschappen

Departement Natuur- en Sterrenkunde

Thesis Universiteit Utrecht - With a summary in Dutch

ISBN: 978-90-393-5177-2

Subject heading: atomic physics / laser cooling and trapping /

Bose-Einstein condensation

Druk: PrintPartners Ipskamp, Enschede

HYDRODYNAMIC EXCITATIONS
IN A BOSE-EINSTEIN CONDENSATE

HYDRODYNAMISCHE EXCITATIES IN EEN BOSE-EINSTEIN CONDENSAAT

(met een samenvatting in het Nederlands)

PROEFSCHRIFT

TER VERKRIJGING VAN DE GRAAD VAN DOCTOR
AAN DE UNIVERSITEIT UTRECHT OP GEZAG VAN
DE RECTOR MAGNIFICUS, PROF. DR. J. C. STOOFF,
INGEVOLGE HET BESLUIT VAN HET COLLEGE VOOR PROMOTIES
IN HET OPENBAAR TE VERDEDIGEN
OP DINSDAG 20 OKTOBER 2009
DES MIDDAGS TE 2.30 UUR

door

ROBERT MEPELINK

geboren op 6 maart 1979 te Hengelo

Promotor: Prof. dr. P. van der Straten

This work is part of the research programme of the 'Stichting voor Fundamenteel Onderzoek der Materie (FOM)', which is financially supported by the 'Nederlandse Organisatie voor Wetenschappelijk Onderzoek (NWO)'.

CONTENTS

1	INTRODUCTION	1
1.1	Cold atoms & Bose-Einstein condensation	1
1.2	Thesis outline	2
2	EXPERIMENTAL SETUP	5
2.1	Introduction	5
2.2	Laser cooling of sodium	6
2.3	The source of cold atoms	14
2.4	Evaporative cooling toward BEC	19
2.5	Bose-Einstein condensation	22
2.6	Conclusion & outlook	29
3	PHASE CONTRAST IMAGING OF BOSE-EINSTEIN CONDENSATES	31
3.1	Introduction	31
3.2	Theoretical description of PCI	33
3.3	PCI setup	38
3.4	Density distribution	40
3.5	Experimental results	45
3.6	Conclusion	54
4	A COLLECTIVE EXCITATION: THE QUADRUPOLE MODE	57
4.1	Introduction	57
4.2	Theoretical description of the quadruple mode	58
4.3	The quadrupole mode above T_c	61
4.4	The quadrupole mode below T_c	64
4.5	Higher order excitation	67
4.6	Conclusion & outlook	70
5	THERMAL CONDUCTIVITY IN A COLD THERMAL CLOUD	73
5.1	Introduction	73
5.2	Experiment	75
5.3	Results and discussion	77
5.4	Conclusion	81

6	A THERMAL WAVE IN THE TWO-FLUID REGIME	83
6.1	Introduction	83
6.2	Experiment	84
6.3	Identified modes	90
6.4	Conclusion & outlook	95
7	THE SECOND SOUND DIPOLE MODE IN THE TWO-FLUID REGIME	97
7.1	Introduction	97
7.2	Experiment	98
7.3	Results & discussion	102
7.4	Conclusion	107
8	SOUND PROPAGATION IN THE TWO-FLUID REGIME	109
8.1	Introduction	109
8.2	Sound propagation in a dilute Bose-Einstein condensed gas . . .	111
8.3	Experiment	114
8.4	Results & discussion	116
8.5	Conclusion	121
9	OBSERVATION OF SHOCK WAVES IN A LARGE BEC	123
9.1	Introduction	123
9.2	Experiment	125
9.3	Numerical simulations	129
9.4	Conclusion	135
	BIBLIOGRAPHY	137
	LIST OF PUBLICATIONS	151
	LIST OF CONFERENCE CONTRIBUTIONS	153
	SAMENVATTING IN HET NEDERLANDS	155
	CURRICULUM VITÆ	163
	DANKWOORD	165

INTRODUCTION

1.1 COLD ATOMS & BOSE-EINSTEIN CONDENSATION

In 1925 Satyendra Nath Bose and Albert Einstein predicted that at low temperatures particles in a gas could all collapse into the lowest quantum state. The resulting state of matter, a Bose-Einstein condensate (BEC), was first observed in the laboratory seventy years later by Cornell and Wieman at the NIST-JILA lab using a gas of rubidium atoms cooled to 170 nanoKelvin [1]. Independently, Ketterle at MIT observed Bose-Einstein condensation in a gas of sodium atoms cooled below 2 microKelvin [2]. Cornell, Wieman, and Ketterle were awarded the 2001 Nobel Prize in Physics “for the achievement of Bose-Einstein condensation in dilute gases of alkali atoms, and for early fundamental studies of the properties of the condensates”.

The path that led to the experimental realization of Bose-Einstein condensation in dilute gases exploited powerful techniques for laser cooling of neutral atoms developed in the 1970s and 1980s. A milestone was reached in 1982 when E. L. Raab *et al.* demonstrated cooling and trapping of neutral sodium atoms with radiation pressure in combination with a magnetic field in a so-called magneto-optical trap (MOT) [3]. In 1997 the Nobel Prize in physics was awarded to Chu, Cohen-Tannoudji, and Phillips “for development of methods to cool and trap atoms with laser light”. Both Nobel Prizes boosted the interest in this field illustrated by the number of article featuring “Bose-Einstein” in its title, about 40 000 during the last 15 years; on average almost 10 a day.

Bose-Einstein condensation in a liquid was reached in the laboratory only a few years after the prediction by Bose and Einstein. Around the 1930s, Keesom *et al.* observed that liquid helium exhibits surprising properties when it is cooled below approximately 2.2 Kelvin, where a sharp peak in the specific heat is found [4]. In 1938 Kapitsa [5], and independently Allen and Misener [6], discovered that helium below 2.17 Kelvin can flow almost frictionless and Kapitsa named this behavior superfluidity. In 1978 he was awarded the Nobel Prize “for his basic inventions and discoveries in the area of low-temperature physics”. Soon afterwards, theoretical work by Landau, London and Tisza showed that this

superfluidity was evidence for the formation of a Bose-Einstein condensate. The quantum liquid exhibits macroscopic quantum effects that are visible to the eye such as the ability of the liquid to “creep” up and out of its container. In 1962 Landau was awarded the Nobel Prize “for his pioneering theories for condensed matter, especially liquid helium”. Further studies showed that the superfluid, now called helium II, behaved as a two-fluid system, partly in a low energy ground state, and partly in an excited state. With a little added heat and manipulation of the superfluid, an interaction of the two states was enhanced, producing a fountain effect, as though two fluids existed [7]. However, the interaction between helium atoms is strong and this reduces the number of atoms in the zero-momentum state, even at zero temperature.

In contrast to the case of a gaseous BEC, where the condensate is directly observed and its density can be determined easily, a BEC has not been observed in helium II. Neutron scattering experiments on helium II yield measurements consistent with a condensate fraction below 10%, where it is assumed a condensate exists [8, 9]. The inability to make a clear distinction between the two components complicates the interpretation of experiments studying the predictions of the two-fluid model like collective excitations, first and second sound, and others. This difficulty led to the search for weakly-interacting Bose gases with a higher condensate fraction and was completed in 1995. Research using gaseous BECs is expected to address open questions relating to the many-body aspects of two-component quantum liquids, namely the interaction between the hydrodynamic normal and the superfluid component at finite temperatures.

Among the first experiments on the gaseous BEC were the study of collective excitations and the matter-wave interference of two overlapping BECs [10–12]. The superfluidity of a BEC is demonstrated by observing vortices in a rotating BEC. However, experimental observations in the two-fluid regime are limited [13, 14]. The reason for the lack of detailed experiments in BECs to study quantum liquids and in particular the hydrodynamical aspects of it, is the limited number of atoms (typically 1–10 million) in the experiments leaving the thermal atoms virtually collisionless. Efforts to decrease the mean free path by increasing the confinement decrease the lifetime of the sample, since the density is limited by three-body decay.

In our setup we have reached the hydrodynamic regime in a thermal cloud above and below the transition temperature T_c . As a consequence, this setup is ideal for studying the two-fluid model and for a direct observation of the interactions between the superfluid and normal fluid component.

1.2 THESIS OUTLINE

The work described in this thesis is presented as follows. In the next chapter the experimental setup is described that is used to reach the hydrodynamic regime

in a Bose gas of sodium atoms. The most important ingredient for reaching this regime is a large number of cold atoms. Starting from solid sodium in an oven, the steps to produce the current world record of 300 million Bose-Einstein condensed atoms are subsequently described. In Chapter 3 a sensitive method to measure the density of the cold atoms is presented, allowing for the observation of the static interactions between the excited and the condensed atoms. Chapter 4 presents the study of a collective excitation and its results substantiates the claim that the hydrodynamic regime is reached. A detailed study of the heat conduction in the hydrodynamic regime above T_c is presented in Chapter 5, followed by a chapter on the excitation of a thermal wave in the two-fluid regime. In Chapter 7 the second sound dipole mode is studied in a partially Bose-Einstein condensed gas. This mode is excited by spatially separating and releasing the center-of-mass of the BEC with respect to the thermal cloud. In Chapter 8 the propagation of second sound in the two-fluid regime is observed and the influence of the thermal cloud on its propagation is studied. Finally, the observation of the excitation and propagation of shock waves is presented in Chapter 9.

EXPERIMENTAL SETUP

Abstract

The most important steps to make a condensate with a large atom number are described in this chapter. An oven filled with solid sodium produces a large atom flux, which is efficiently slowed down using a Zeeman slower. The slowed atoms are captured in a dark-spot MOT. Spin polarization of the captured atoms allows us to transfer 60% of the atoms to a magnetic trap. Starting with a large number of atoms allows for efficient evaporative cooling. The number of atoms is reduced by only a factor of 100 before T_c , the transition temperature for Bose-Einstein condensation, is reached with more than $1 \cdot 10^9$ atoms. Depending on the trap configuration, up to $3 \cdot 10^8$ atoms can be cooled down to the Bose-Einstein condensed state. This is by far the largest number of condensed alkali metal atoms to date and an ideal starting point for the study of hydrodynamic thermal clouds and the two-fluid regime.

2.1 INTRODUCTION

In the experiments described in this thesis we study the two-fluid regime in a gaseous BEC at finite temperature, where the thermal cloud is in the hydrodynamic regime. In most experiments with gaseous BECs the mean free path of the thermal atoms is small compared to the size of the thermal cloud leaving these atoms virtually collisionless, with a few notable exceptions [13, 14]. Efforts to decrease the mean free path by increasing the confinement limits the lifetime of the sample, since the density is limited by three-body decay. The way to reach the hydrodynamic regime is to increase the size of the sample by decreasing the confinement in order to make its size larger than the mean free path of the atoms, although the density and thus the mean free path will decrease as well. Since the density is limited, the most hydrodynamic condition is reached by preparing clouds with a large atom number in a weak confinement for which the density is barely below its limiting value. The confinement can be easily controlled and therefore, the challenge is to trap and cool as many atoms as possible. However, compared to liquid helium and hydrogen condensates which start from cryogenic techniques, the number of alkali metal atoms captured with laser cooling and

trapping techniques is small and as a consequence the number of condensed atoms after evaporative cooling is limited (typically 1–10 million).

In this chapter the experimental setup is described, which is used to generate large atom number condensates. Making a BEC is a multi-stage process. First, solid sodium is heated in an oven resulting in a large flux of hot sodium atoms. These atoms are decelerated in a Zeeman slower and subsequently cooled and trapped in a magneto-optical trap (MOT) using laser light and a magnetic field. The atoms in the MOT have a temperature of roughly $100\ \mu\text{K}$ and still need to be cooled further to reach the Bose-Einstein condensation temperature T_c of roughly $1\ \mu\text{K}$. This is achieved by transferring the atoms into a magnetic trap (MT) after which the atoms can be cooled to temperatures below the Bose-Einstein transition temperature T_c by forced evaporative cooling. The number of condensed atoms in this setup is up to 300 million, which to our knowledge is the largest BEC in the world starting from an optical trap. This large atom number Bose-Einstein condensate machine is therefore an ideal starting point for studying the two-fluid regime. Furthermore, a large atom number allows better signal-to-noise ratios and robustness in day-to-day operation.

2.2 LASER COOLING OF SODIUM

2.2.1 *Properties of sodium*

The element studied throughout this thesis is sodium, the second element in the alkali metals group, which has only one stable isotope, ^{23}Na . The alkali metals are the most commonly used elements in laser cooling and trapping experiments; the atoms captured in the first magneto-optical trap (MOT) were sodium atoms, the first BEC was made with rubidium atoms, soon followed by condensates of sodium and lithium. The main reason for choosing alkali metals for laser cooling and trapping experiments lies in their strong D-lines with transition frequencies in the range of modern laser systems. The characteristic yellow/orange color, found in the emission of sodium street lamps is the result of this D-line transition. Due to spin-orbit ($L \cdot S$) coupling in the 3^2P excited state, a fine structure splitting with $J = 1/2, 3/2$ occurs. This results in the typical D line doublet $3^2\text{S}_{1/2} \rightarrow 3^2\text{P}_{1/2}$ (D₁line), $3^2\text{P}_{3/2}$ (D₂line). The wavelength of the D₂ transition is approximately 589.2 nm and the D₁ line has a wavelength of approximately 589.7 nm. The coupling of the nuclear spin (I) with the total angular momentum of the valence electron (J) results in the so-called hyperfine splitting occurs ($F = I + J$). As a result both the ground and the excited state are split. Two $3^2\text{S}_{1/2}$ states exist with $F_g = 0$ and 1, which can both be considered as ground states and there are four $3^2\text{P}_{3/2}$ excited states, with $F_e = 0, 1, 2, 3$. Furthermore, the states have a magnetic sub-structure; each hyperfine state F has $2F + 1$ magnetic sub-levels M_F and as a consequence many transitions are

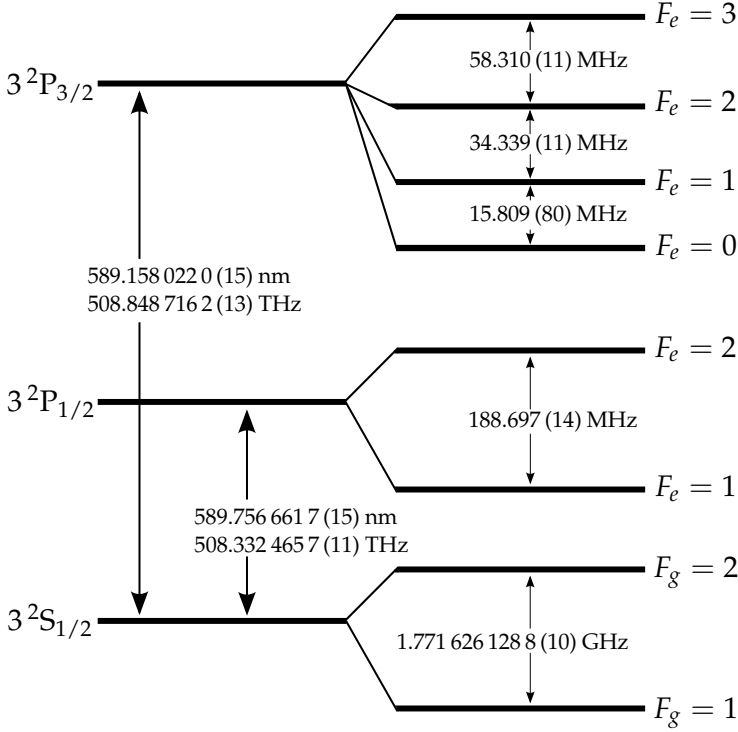


Figure 2.1: A schematic representation of the sodium hyperfine level splitting for the $3^2S_{1/2} \rightarrow 3^2P_{1/2}$ (D_1) and $3^2S_{1/2} \rightarrow 3^2P_{3/2}$ (D_2) transition. Here, the wavelength in vacuum is given. Excited state values are taken from Ref. [15, 16] and the ground state values are taken from Ref. [17]. The D-line values are taken from Ref. [18].

available. A schematic representation of the fine and hyperfine splitting of sodium is shown in Fig. 2.1.

The transition used for cooling ^{23}Na is the $3^2S_{1/2}, F_g = 2 \rightarrow 3^2P_{3/2}, F_e = 3$ transition, which is an almost closed transition. However, this transition is not completely closed due to off-resonant scattering to the $F_e = 2$ excited state, which can decay to the $F_g = 1$ state. If the laser is tuned to the cycling transition it is not resonant with atoms in the lowest ground state, since the linewidth of the laser, typically in the order of 1 MHz, is small compared to the splitting of the ground states, roughly 1.7 GHz for sodium. As a consequence, atoms in the lowest ground state are lost for the cooling process. Although the probability for atoms to decay in the $F_g = 1$ ground state is small, the large number of photon absorption and spontaneous emission cycles needed for the maximum

PROPERTY		
DESCRIPTION	SYMBOL	VALUE
Cycling transition		$3^2S_{1/2}, F_g = 2 \rightarrow 3^2P_{3/2}, F_e = 3$
Repumping transition		$3^2S_{1/2}, F_g = 1 \rightarrow 3^2P_{3/2}, F_e = 2$
Frequency	ω_0	$2\pi \times 508.848\,716\,2\,(13)\text{ THz}$ [18]
Wavelength (vacuum)	λ	$589.158\,022\,0\,(15)\text{ nm}$ [18]
Wavelength (air)	λ_{air}	$589.000\,35\text{ nm}$
Lifetime	τ	$16.254\,(22)\text{ ns}$ [19]
Natural linewidth	Γ	$2\pi \times 9.792\,(13)\text{ MHz}$ [19]
Atomic mass	m	$22.989\,769\,280\,7\,(28)\text{ u}$ [20]
Recoil velocity	v_r	2.9461 cm/s
Recoil Temperature	T_r	$2.2\text{ }\mu\text{K}$
Doppler Temperature	T_D	$235\text{ }\mu\text{K}$
s-wave scattering length	a	$52.98(40)a_0 = 2.804(21)\text{ nm}$ [21]
Saturation intensity (cycling transition)	I_{sat}	$6.2600(21)\text{ mW/cm}^2$ [22]

Table 2.1: Sodium (D_2) properties

deceleration makes laser cooling only feasible if the atoms are pumped out of the lowest ground state, a process often referred to as “repumping”. Generating this repumping frequency can be achieved by frequency shifting the laser light used for the cycling transition with approximately 1.7 GHz by means of Electro-Optical Modulators (EOMs) or Acousto-Optical Modulators (AOMs). Due to the small efficiency to generate light with a large frequency difference and the limited laser power available, we use an additional laser to generate the repumping frequency. Some general properties of sodium are tabulated in Table 2.1 and the values given in this table are used throughout this thesis, where applicable.

2.2.2 Laser system

The laser light needed for laser cooling is generated by two continuous wave (CW) single frequency ring-dye lasers^a, which use Rhodamine 6G as gain medium. The laser used to generate the cooling light ($F_g = 2 \rightarrow F_e = 3$ transition) is pumped by a 5 W solid state CW laser^b and generates up to 750 mW. The other laser, used to generate the repumping frequency ($F_g = 1 \rightarrow F_e = 2$ transition) is pumped by a 5 W Ar⁺ laser^c. This laser is operated at 3 W to generate up to 200 mW of light.

The dye lasers are tuned to the appropriate transition (D_2) and locked to this frequency using a reference cavity^d with a specified bandwidth of 1 MHz. Next, the reference cavity is tuned to the appropriate hyperfine transition and kept at this frequency using the locking method described in § 2.2.3. The laser light is deflected by AOMs^e in order to generate the appropriate frequencies and the light is transported to the vacuum setup through single-mode polarization preserving optical fibers^f. A schematic representation of the laser setup is shown in Fig. 2.2 including the relevant laser frequencies. A third dye laser^g, pumped by a 5 W solid state CW laser^h, is used for experiments after the atoms have been cooled and trapped. The wavelength of this laser can be tuned between approximately $\lambda = 565$ nm and $\lambda = 615$ nm. Its output power is approximately 1 W at $\lambda = 590$ nm.

a Spectra-Physics 380D

b Spectra-Physics Millennia

c Coherent Innova 90

d Spectra-Physics 388 StabiLok interferometer

e Isomet 1205-C2

f Fibercore HB600

g Coherent 699

h Coherent Verdi

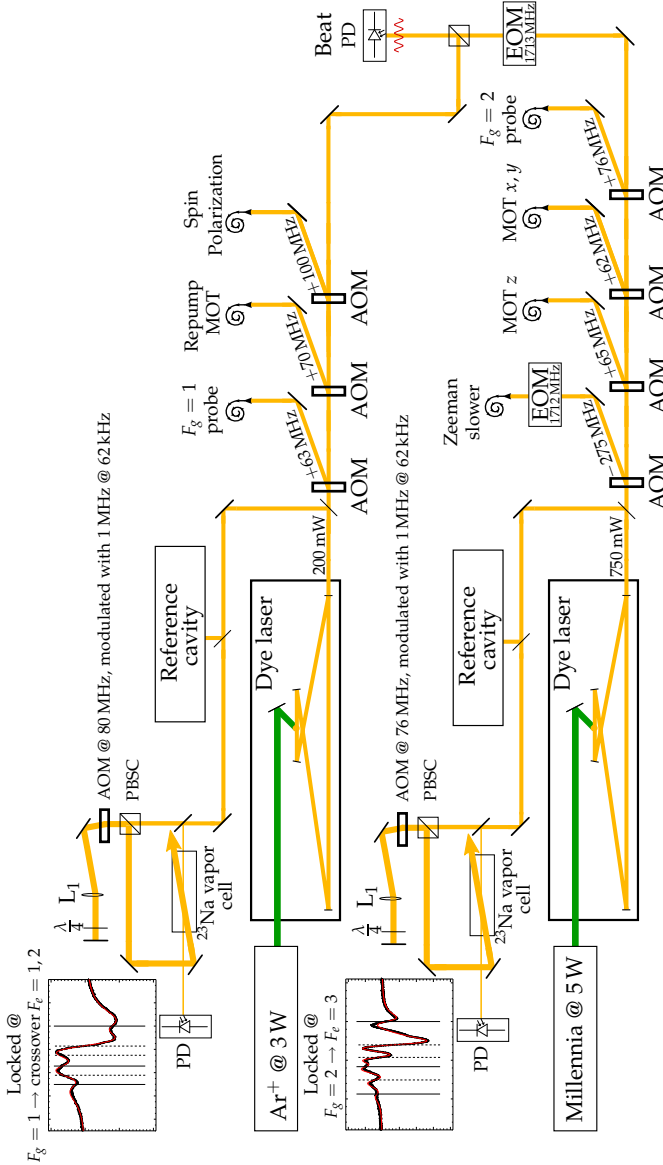


Figure 2.2: Laser setup before the optical fibers. Both lasers are locked using FMS (see § 2.2.3), one (top, “repumper”) to the transition between the $F_g = 1$ and the crossover $F_e = 1$ and the crossover peak between the $F_e = 1$ and $F_e = 2$, the other (bottom, “repumper”) to the $F_g = 2 \rightarrow F_e = 3$ transition. The polarizing beam-splitter cube (PBS) and lens L_1 are used to double-pass the laser light into the FMS setup. The shift induced by this AOM is (partly) compensated for by the AOMs deflecting the laser light into the corresponding fibers. The light used for the Zeeman slower passes an EOM crystal to generate sidebands used for the repumping frequency. The frequency difference between both lasers is monitored by measuring the beat frequency between the light of one laser and the positive first sideband of the other, generated by a second EOM crystal.

2.2.3 Laser locking

Laser locking is based on absorption spectroscopy in a vapor cell. By resolving a narrow atomic transition and using the resulting absorption signal for an electronic feedback circuit to adjust the laser frequency, the laser is kept at a specific transition for many hours.

The method applied in our lab is based on the well-known saturated absorption spectroscopy technique [23]. A small fraction of the laser light is split off directly after the output coupler and used for the spectroscopy. This beam is split into two parts: 5% of the output power is used for a probe beam and 95% is used as a pump (saturation) beam. The probe beam passes a sodium vapor cell and the intensity is measured using a photo diodeⁱ. The pump beam is double-passed through an AOM before counter-propagating the probe beam in the vapor cell. In common saturated absorption spectroscopy a similar setup is used, with the exception that the AOM is replaced by a mechanical chopper.

The frequency of the AOM is modulated at 62 kHz with a 1 MHz amplitude around its center frequency of 76 MHz. The frequency modulation (FM) of the pump beam causes the measured absorption signal (intensity on the photo diode) to modulate, converting the FM signal into an amplitude modulation (am) of the measured absorption. This technique is referred to as frequency-modulation spectroscopy (FMS) [24].

The improvement with respect to common saturated absorption spectroscopy is explained by writing for the measured intensity as a function of the laser frequency ν

$$I(\nu) = I(\nu + A \sin \Omega t), \quad (2.1)$$

where the amplitude A of the dither is small compared to the natural linewidth Γ and ν . A Taylor expansion of the Eq. (2.1) for small A yields

$$I(\nu + A \sin \Omega t) \approx I(\nu) + A \frac{dI(\nu)}{d\nu} \sin \Omega t. \quad (2.2)$$

As a result, the dither causes the measured intensity to contain a DC term and a term oscillating at the dither frequency Ω .

The intensity is converted to a current by the photo diode and this current is measured using a lock-in amplifier^j, which is tuned to the carrier frequency Ω and therefore only the $\sin \Omega t$ term is extracted. In the limit of small dither amplitude A , the measured signal is proportional to the first derivative of the absorption signal. Fig. 2.3 shows the result of a typical scan over the $F_g = 1 \rightarrow F_e = 0, 1, 2$

ⁱ BPX-65

^j Single-board Femto LIA-BV-150-H

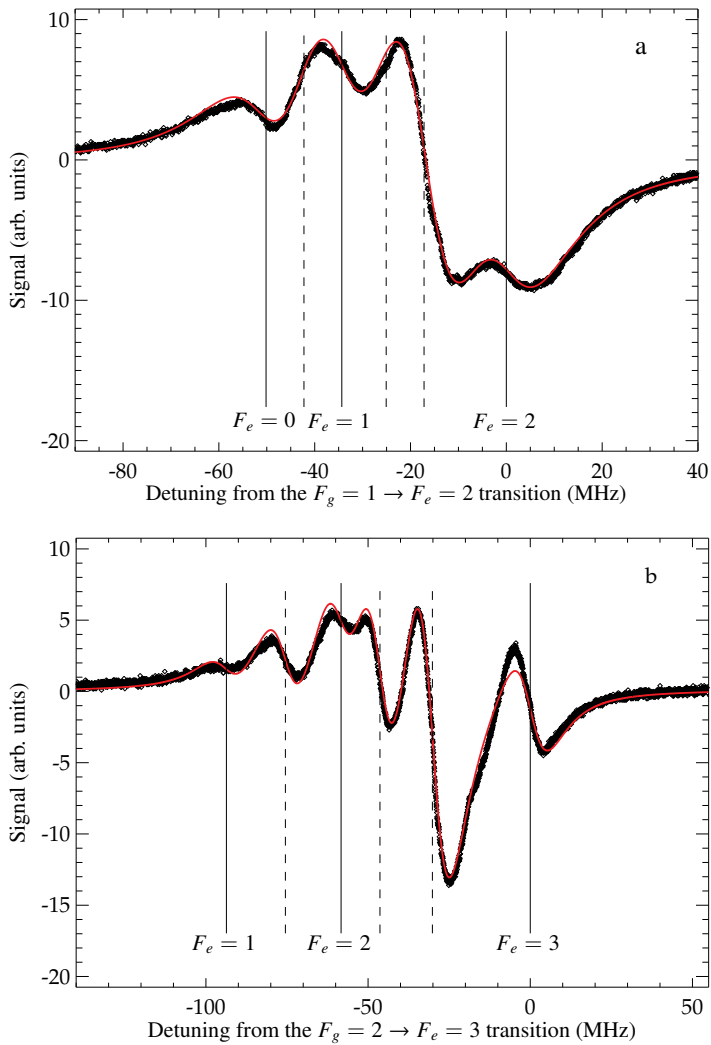


Figure 2.3: Frequency-modulation spectroscopy at the ^{23}Na D_2 line of the $F_g = 1 \rightarrow F_e = 0, 1, 2$ transitions (Fig. a) and $F_g = 2 \rightarrow F_e = 1, 2, 3$ transitions (Fig. b). The solid vertical lines indicate the position of the F_e transitions, the dashed lines indicate the position of the cross-over peaks. The solid line through the data points is the result of a fit of the data to the derivative of Eq. (2.3).

and $F_g = 2 \rightarrow F_e = 1, 2, 3$ transitions using the FMS technique. The data in Fig. 2.3 is fitted to a Lorentzian line profile \mathcal{L} given by

$$\mathcal{L}(\omega) = \frac{(\Gamma_{\text{eff}}/2)^2}{(\omega - \omega_0)^2 + (\Gamma_{\text{eff}}/2)^2} \quad (2.3)$$

where ω is the laser frequency, Γ_{eff} is the effective linewidth, and ω_0 is resonance frequency of the transition. The known splittings of the hyperfine states (see Fig. 2.1) are used to determine the scan rate. The fit yields an effective linewidth $\Gamma_{\text{eff}}/(2\pi) = 26$ MHz (Fig. 2.3a) and $\Gamma_{\text{eff}}/(2\pi) = 19$ MHz (Fig. 2.3b).

FMS has three main advantages over standard saturated absorption spectroscopy. First of all, the noise on the measured signal is greatly reduced by measuring through the lock-in amplifier at a high dither frequency. The use of an AOM to modulate the frequency allows for using higher frequencies than a mechanical chopper can reach, without the vibrations caused by the chopper. Most sources of noise such as pumps, switching of electric relays, etcetera induce noise at frequencies well below the dither frequency and are therefore rejected from the measured signal. Furthermore, the laser intensity noise (typically $1/f$ noise) is more strongly reduced for higher dither frequencies. Secondly, since the measured signal is the first derivative of the individual Lorentzian shaped hyperfine transition peaks, the peak of the absorption corresponds to a zero-crossing, which makes the method insensitive for fluctuations in the beam power. As a result, implementation of an electronic feedback circuit is straight-forward and accurate. Finally, the absolute detuning of the laser is determined by the combination of the choice of the hyperfine state and the center frequency of the AOM and therefore tunable in a wide frequency range (~ 150 MHz). In contrast, detuning from an atomic resonance using saturated absorption spectroscopy requires locking on a slope of the resonance peak, making the method sensitive for fluctuations in the beam power.

Both lasers are locked using the FMS technique: one is locked to the $F_g = 2 \rightarrow F_e = 3$ transition and the other to the $F_g = 1$ to the cross-over peak in between the $F_e = 1$ and $F_e = 2$ transition. Both locks yield a well-known, absolute frequency, which is monitored by the beat frequency between the light of one laser and the first sideband of the other, where the sideband is generated by passing through an EOM crystal^k operated at 1713 MHz. The resulting beat frequency is shifted to the range of 20 MHz, which can be measured with a fast photo diode^l.

The fluctuations in the beat frequency typically have an amplitude between 1 MHz and 1.5 MHz, most probably the result of the bandwidth of the lasers. While both lasers are locked, the beat frequency shows no significant shift within a period of weeks and assures both locks (and therefore both frequencies) are drift-free on the time scale of all experiments.

^k LiTaO₃

^l Hamamatsu InGaAs G3476-01

To further reduce laser induced intensity and frequency noise, FMS can be extended by splitting off an extra probe beam which passes through the vapor cell, not overlapping the pump beam. The intensity of the second probe beam is measured as well and electronically subtracted (balanced) from the signal of the first photo diode before the signal is measured using the lock-in amplifier. Since the measured fluctuation of the beat signal of both lasers is very close to the specified bandwidth of the lasers, we did not choose to implement this extra noise reduction technique.

The method previously used for laser locking in our lab, DFBL [25], is insufficiently capable of resolving the individual hyperfine transitions. The resulting derivative of the absorption peak mainly consisted of one broad, weakly sloped transition, the zero-crossing being sensitive to both laser pointing and spectroscopy alignment resulting in a drift in the beat frequency as large as 5 MHz per hour.

2.3 THE SOURCE OF COLD ATOMS

2.3.1 *Recirculating sodium oven*

In order to create a high flux of sodium atoms, 50 g of solid sodium is placed in the first chamber of a two-chamber oven. The first chamber, which consists of nw-35 conflat parts, is heated to 600 K. The sodium vapor leaves the first chamber through a 6 mm diaphragm, which is heated to 620 K to prevent condensation of sodium atoms around the diaphragm. A collimated atom beam enters the second chamber, which functions as a recycling chamber and consists of a conical adapter to nw-63. At the end of this chamber an extra 10 mm diaphragm is used to remove the atoms with the largest divergence from the collimated atom beam.

The second chamber is connected to the first chamber through a 6 mm internal diameter tube allowing for the back-flow of sodium atoms. The second chamber is heated to 380 K due to heat conduction, slightly above the melting temperature of sodium (371 K). The recirculating tube is kept at 420 K in order to allow the fluid sodium to flow back to the first chamber.

The oven has operated for approximately 10 000 h and since we estimate the operation time of 50 g sodium to be 5000 h we conclude the oven recirculates indeed. After the 10 000 h operating time the pressure in the oven began to increase gradually, resulting in the need to disassemble the oven. We found approximately 20 g of sodium in the oven, confirming that the oven recirculates.

The exterior of the oven showed green deposits (most probable sodium salts) on all flanges of the first chamber, probably caused by diffusion of sodium through the gaskets, which eventually led to sealing problems. We decided to build a new oven made from type 316 stainless steel, since it is found to prevent the diffusion of (even more reactive) lithium through the flanges in the MIT group [26]. The

operation time has not been long enough to draw conclusions on the diffusion of sodium through the flanges in the new oven.

2.3.2 Zeeman slower and atom flux optimization

At 600 K the oven produces a collimated sodium flux of $5 \cdot 10^{12}$ atoms/s. Assuming a Maxwell-Boltzmann distribution of the velocity at this temperature, only a negligible fraction of the atoms has a velocity smaller than the capture velocity of the MOT, which is about 40 m/s. To increase the fraction of atoms with a velocity below the capture velocity, the thermal atomic beam is slowed down using a Zeeman slower [27] designed by Molenaar and Van der Straten [28].

Atoms exiting the oven are decelerated in the Zeeman slower by the momentum transfer of photons from a counter-propagating laser beam. Along the deceleration path the atoms are kept resonant with the applied laser beam by applying an inhomogeneous magnetic field along the propagation direction to compensate the Doppler-effect with the Zeeman-shift of the atomic resonance.

The Zeeman slower only results in longitudinal deceleration, and in absence of radial deceleration the atomic beam will get divergent along the way. In order to get the highest possible flux in the capture area of the MOT, the end of the Zeeman slower has to be close to the MOT chamber. Since a vacuum pumping section is needed in between the MOT chamber and the Zeeman slower, this is achieved by dividing the last stage of the slower in two parts. Atoms are decelerated in the first part to roughly 200 m/s, with limited increase of the divergence. After the pumping section is passed the atoms are decelerated further in the second part.

The two-part slower has advantages over several other techniques to prevent a large divergence such as a magneto-optical compressor and a (2D magneto-optical lens, which are characterized by Van Ooijen [29]). The two-part slower had the disadvantage that it introduces a zero crossing of the magnetic field at the position of the pumping section. In the absence of a large energy splitting between the magnetic sub-levels, off-resonant scattering drives the atoms into the $F_g = 1$ ground state at the position of the zero-crossing and light at the repump frequency has to be applied to prevent losses.

To apply both the slowing frequency and repumping frequency simultaneously and spatially well aligned, we generate the repumping frequency by passing the Zeeman laser beam through an Electro-Optical Modulator (EOM) operating at 1713 MHz. After passage two side-bands at ± 1713 MHz are added with 12% of the intensity of the central frequency.

The EOM crystal used for this purpose by Van der Stam [30] has an effective aperture of $1.5 \text{ mm} \times 1.5 \text{ mm}$ and was exposed to an intensity close to the damage threshold, due to the need of focusing the light through the small crystal. Ideally, the EOM crystal is placed before entering the fiber to facilitate the alignment of the

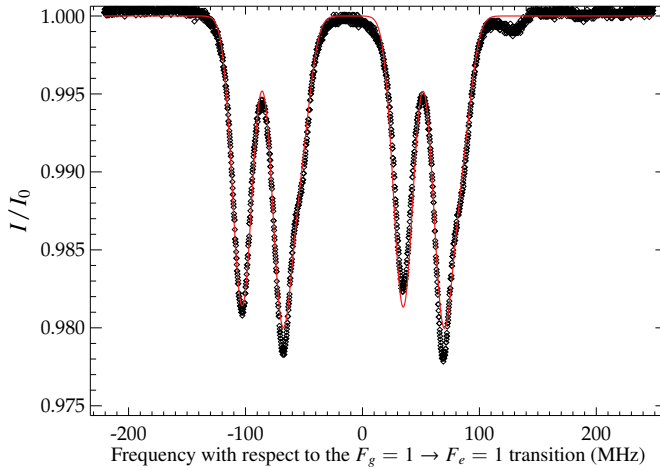


Figure 2.4: Absorption measurement of the cold atom flux on the $F_g = 1 \rightarrow F_e = 1$ transition. The presented data is the average over 16 scans. The solid line is the result of a fit to a combination of Doppler broadened Lorentzian shaped functions for each transition.

slowing beam and ensure the quality of the beam mode. Since the efficiency of the fiber, about 70 %, causes the need to expose the crystal to even higher intensities, the crystal could only be placed behind the fiber. Furthermore, the intensity proved to be still too high and in combination with the small birefringence of the crystal the beam profile worsened over time, decreasing the slowing efficiency.

We replaced the EOM crystal with a $3 \text{ mm} \times 3 \text{ mm}$ crystal^m allowing for a larger beam to pass the crystal and therefore a reduction of the intensity. This crystal can be placed before the light is coupled into the fiber. The quality of the deceleration beam profile dramatically improved, especially after passing the fiber. The improved beam profile and increased intensity resulted in a tenfold increase in the cold atom flux into the MOT chamber.

The flux is determined by a Doppler sensitive absorption measurement of a laser beam. The procedure is described in detail in Ref. [31]. In short, a collimated laser beam (probe beam) is aimed at the atom beam, hitting the atoms at 45 degrees and passes the atoms again after retro-reflection. The frequency of the probe beam is scanned over the $F_g = 1 \rightarrow F_e$ transitions and the absorption is measured.

From such an absorption measurement, shown in Fig. 2.4, the individual transitions can be (partly) identified. The small “shoulder” in Fig. 2.4, around -50 MHz and 90 MHz , is the only sign of the almost unresolved (due to Doppler

^m LiTaO₃

broadening) $F_g = 1 \rightarrow F_e = 0$ transition. The small feature around 130 MHz is present in all taken spectra and of unknown origin. Since it cannot correspond to any $F_g = 1 \rightarrow F_e$ transition this feature is not included in the fit function. Knowing the splitting of these hyperfine states (see Fig. 2.1), the scan rate is determined and the Doppler shift can be derived from the absolute frequency shifts. Note that both transitions are seen twice due to the retro-reflection of the probe beam. The flux of atoms is determined by making a least square fit to Lambert-Beer's law given by

$$I = I_{\text{bg}} + I_0 \left(e^{-\sigma_{\text{eff}} \rho L} \right), \quad (2.4)$$

with I_0 the incident light intensity, I_{bg} the offset on the signal, ρ the density, σ_{eff} the scattering cross section and L the distance through the atom beam. From the absorption the cold atom flux Φ is determined, as it is related to the density as

$$\rho = \frac{\Phi}{\pi r^2 v}, \quad (2.5)$$

with $r = 9.5$ mm the atom beam radius and v the atom velocity. The distance L is $2r / \sin(\pi/4) = \sqrt{8}r$ and σ_{eff} is given by

$$\sigma_{\text{eff}} = \frac{3\lambda^2}{2\pi} \sum_e C_{ge} \left[1 + \left(\frac{2\delta_{ge}}{\Gamma} \right)^2 \right]^{-1}, \quad (2.6)$$

with C_{ge} the Clebsch-Gordan coefficient from a state g to e , λ the wavelength of the light and δ_{ge} the detuning from resonance. The intensity of the incident light is so low, $I \simeq 10^{-4} I_{\text{sat}}$ with I_{sat} the saturation intensity, that saturation can therefore be neglected.

The atom flux is found by fitting the data shown in Fig. 2.4 to Eq. (2.4) which yields $\Phi = (3.4 \pm 0.1) \cdot 10^{11}$ atoms/s, the central velocity is 58.2 ± 0.2 m/s with a spread of 6.95 ± 0.06 m/s. The measured velocity spread is only slightly above the velocity spread of 6 m/s corresponding to the natural linewidth for sodium.

The measured cold atom flux is roughly 40 times larger than the estimated value found by Van der Stam [30]. We attribute this enlarged flux to the improvement of the Zeeman slowing beam, achieved by installing the new EOM crystal in front of the optical fiber (a tenfold increase) and a 20 K higher operation temperature of the sodium oven (a twofold increase).

2.3.3 MOT loading

The large cold atom flux is captured in the MOT. This MOT consists of three retro-reflected laser beams and a magnetic quadrupole field to slow down and capture the atoms.

The light for two of the directions, the x - and y -direction, is generated with the same AOM and detuned $\delta = -1.4\Gamma$ with respect to the cycling transition $F_g = 2 \rightarrow F_e = 3$. The light in the z -direction has passed a separate AOM driver, which is not phase-locked to the driver generating the light for the x - and y -direction. The detuning of the light in the z -direction is $\delta = -1.1\Gamma$ with respect to the cycling transition. In this coordinate system, gravity works in the $(\hat{x} + \hat{y})$ direction. Note that the detuning used in this setup is small compared to the value reported by most laser cooling groups: $\delta \approx -2\Gamma$.

Atoms are pumped out of the $F_g = 1$ state by a separate laser beam, which is detuned 0.7Γ with respect to the $F_g = 1 \rightarrow F_e = 1$ transition. The center part of this beam is blocked by a 12 mm diameter opaque dot to create a dark-spot MOT [32]. The atoms in the center of the MOT end up in the dark $F_g = 1$ state, thereby reducing the radiation pressure, which is the dominating loss process in a normal (bright) MOT.

The magnetic quadrupole field needed for the MOT to function is generated by two coils placed in anti-Helmholtz configuration producing a 5 G/cm gradient at the typical current of 15 A.

Photo diodesⁿ are used to measure the power of each individual beam at the end of the fiber after passing a Glan-Taylor prism (Zeeman slower, MOT- z) or a polarizing beam-splitter cube (PBSC) (MOT- x,y , probe beams). The measured intensity is used in an electronic feedback circuit to adjust the amplitude of the corresponding AOM driver, thereby controlling the amount of light through the fiber. This procedure assures reproducible and stable intensities during each loading cycle of the MOT. Details of the intensity feedback are given in Ref. [33]. By measuring the intensity after the light has passed the Glan-Taylor prism or PBSC, both intensity and polarization fluctuations can be compensated for. Under typical conditions, the MOT is loaded for four seconds and with the intensity stabilization active the number of atoms in the MOT varies less than 5% between different loading cycles within a few hours. Typically, we make a MOT containing approximately $3 \cdot 10^{11}$ atoms at a temperature of $120 \pm 20 \mu\text{K}$. The number of atoms in the MOT is extrapolated from absorption imaging measurements of evaporatively cooled clouds.

In Fig. 2.5 the loading and decay curves of the dark-spot MOT are shown, where loading (decay) is initiated by opening (closing) a valve in between the MOT chamber and the oven starting with no atoms (a fully loaded cloud). The load and decay rate is determined by fitting the measured curves to the solution of the differential equation for the number of atoms $N(t)$

$$\frac{dN(t)}{dt} = \Phi - AN(t) - BN^2(t), \quad (2.7)$$

ⁿ BPX 65

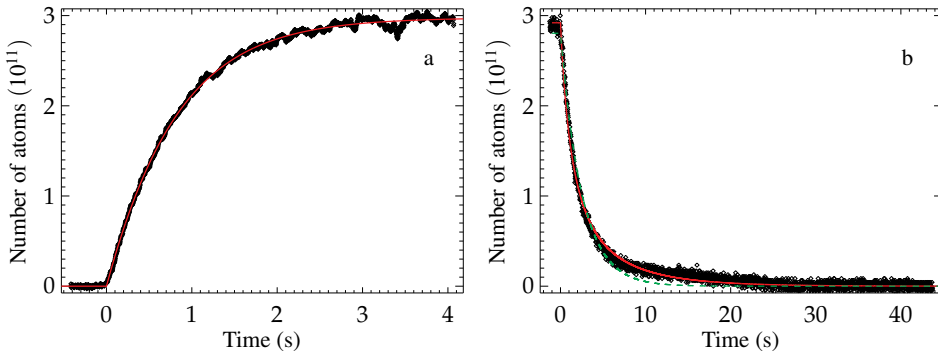


Figure 2.5: Loading curve (Fig. a) and decay curve (Fig. b) of a dark-spot MOT. The solid lines are the result of a fit of the data to the solution of Eq. (2.7).

describing the balance between the incoming flux Φ , collisions with background atoms at rate A and intra-MOT collisions at rate B . The fit to the loading curve (Fig. 2.5a) indicates the loss rate is dominated by collisions with background atoms and the $(1/e)$ load time is given by $\tau = A^{-1} = 0.956(7)$ s. The fit to the decay curve (Fig. 2.5b) shows the decay time is roughly seven times longer than the load time. We attribute this reduction in the loss rate A to the absence of the sodium beam during the decay measurement. Due to the reduced loss term A , the intra-MOT loss rate B can be observed in the loss process. The fit yields $A^{-1} = 6.84(6)$ s and $B^{-1} = 5.38(4) \cdot 10^{11}$ s.

2.4 EVAPORATIVE COOLING TOWARD BOSE-EINSTEIN CONDENSATION

2.4.1 From MOT to MT

The atoms captured in the MOT are transferred to a magnetic trap (MT) in clover leaf configuration after being spin-polarized to achieve a typical transfer efficiency of about 60%. The efficiency increases for lower MOT densities to about 75% [34].

The switching of the MT, the laser beams (by switching the AOMs) and the other time-critical components in the experiment is controlled by a computer. A computer program with an intuitive graphical user interface^o is used to create a sequence and send it to two National Instruments cards, which clock out the

^o based on WordGenerator 3.14, developed at MIT

digital^p and analog^q signals. The clock frequency of the output board limits the time resolution to $2\ \mu\text{s}$.

Since the capacity of the memory of the cards is insufficient to sequence the complete experiment ($\sim 100\ \text{s}$) at $2\ \mu\text{s}$ resolution, a variable clock speed is used to save memory in stages, which are not time-critical at the μs level such as MOT loading and the first stages of the evaporative cooling. The variable clock speed is implemented using the frequency shift keying (FSK) function of the clock on the analog output board, allowing to decrease the clock frequency by a factor of 100 on-demand, controlled by a digital line [35].

During the transfer of the atoms to the MT, all light is turned off by switching the AOM drivers and concurrently closing mechanical shutters in front of the optical fibers. The shutters have to be opened shortly before driving the AOM and vibrations due to the opening have been seen to cause a frequency fluctuation of dye laser light ($\pm 3\ \text{MHz}$) for roughly 250 ms. This fluctuation is only relevant for the probe beam used for absorption imaging, which is tuned to the $F_g = 1 \rightarrow F_e = 1$ resonance within 1 MHz and critical within the time window the frequency fluctuates. By adding a rubber connector to the post holder, opening the shutter no longer influences the beat frequency.

2.4.2 Characterization of the MT

The details of the MT can be found in Ref. [29]. With this configuration a field gradient of $118\ \text{G/cm}$ in the radial direction is generated at the maximum available current of 300 A. The curvature field in the axial direction is $42\ \text{G/cm}^2$ at the maximum available current of 200 A. At maximum current, this yields a harmonic trapping potential characterized by the radial frequencies $\omega_{\text{rad}}/(2\pi) = 95.56(7)\ \text{Hz}$ and axial frequency $\omega_{\text{ax}}/(2\pi) = 15.71(2)\ \text{Hz}$, which are determined experimentally (see Fig. 2.6 for typical trap frequency measurements). Both gradient and curvature coils are equipped with an in-house designed switch, which allows the magnetic field be turned off with a $(1/e)$ time constant of $750\ \mu\text{s}$ [30].

The pressure in the MOT/BEC chamber is less than $1 \cdot 10^{-11}\ \text{mbar}$, which is the lowest value the pressure gauge can measure. This background pressure results in a 280 s lifetime. Typical evaporation times are 60 s, which is much shorter than the lifetime. The background pressure is determined by lifetime measurements and found to be $4_{-1}^{+2} \cdot 10^{-12}\ \text{mbar}$.

We begin the evaporation after the atoms in the MT are allowed to rethermalize for 4 s, after which a linear rf-field frequency ramp is applied, generated by a direct digital synthesizer^r (DDS), starting at 60 MHz and decreasing to 2.5 MHz

p PCI-6534

q PCI-6713

r Novatech Instruments Inc. DDS8m, 100 MHz

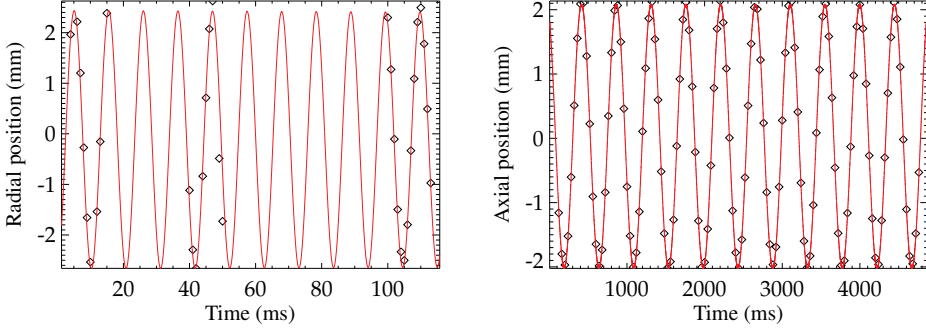


Figure 2.6: Determination of the trap frequencies in the radial (left) and axial (right) direction. Here, $\omega_{\text{rad}}/(2\pi) = 95.56(7)$ Hz and $\omega_{\text{ax}}/(2\pi) = 2.2325(3)$ Hz. A center-of-mass oscillation is induced by a fast displacement of center of the trap in one of the directions. The position of the cloud is measured as a function of time after the oscillation is induced using (destructive) absorption imaging (see § 2.5.3).

with respect to the bottom of the trap in 40 s. With only one rf-field frequency antenna placed outside the vacuum chamber, we use a 15 W rf-field amplifier^s to ensure thermal atoms with a velocity above the threshold set by the rf-field frequency have a large probability to be spin-flipped. During this ramp the efficiency parameter $\eta = (\dot{T}/T)(\dot{N}/N) \approx 2$.

The final evaporative cooling stage depends on the type of experiments we want to perform. In order to get the largest number of condensed atoms we have to reduce the three-body losses, which limit the density. Due to avalanche enhanced losses, we have to decompress the MT in the axial direction to reduce both the density and the avalanches [36].

Fig. 2.7 shows the number of particles as a function of the temperature in the final stage of the evaporative cooling. All measurements shown are done above the transition temperature T_c . The data in Fig. 2.7 show the efficiency parameter η increases around $7 \mu\text{K}$ and shows the onset of runaway evaporation. The data shown in Fig. 2.7 is provided as a benchmark for our setup.

Typically, we work with traps characterized by axial trap frequencies ranging from $\omega_{\text{ax}}/(2\pi) = 4$ Hz to $\omega_{\text{ax}}/(2\pi) = 1.1$ Hz in the final stage of the evaporation. Trap frequencies are measured by inducing a center-of-mass oscillation in one direction, as shown in Fig. 2.6 for both the radial and axial direction. The frequency is determined by making a least-square fit to a damped sinusoid. In both directions, no significant damping is found. The fit yields for

^s Ophir 5303055, 150 kHz–230 MHz, operated at 15 W

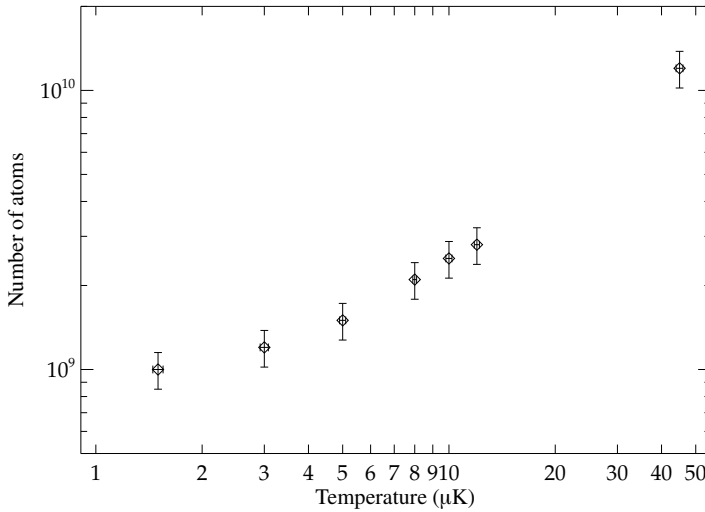


Figure 2.7: Number of atoms as a function of temperature during the evaporative cooling. The rightmost point corresponds to a rf-field frequency of 47.5 MHz (with respect to the bottom of the trap), the leftmost point corresponds to $T \approx 1.2T_c$ at a rf-field frequency of 300 kHz.

the radial frequency $\omega_{\text{rad}} / (2\pi) = 95.56(7)$ Hz and for the axial frequency (after decompression) $\omega_{\text{ax}} / (2\pi) = 2.2325(3)$ Hz. Due to the decompression, the clouds become cigar-shaped with an aspect ratio of up to 1 : 85 for the lowest axial trap frequency.

2.5 BOSE-EINSTEIN CONDENSATION

2.5.1 Observation of the BEC

As can be seen from the data presented in Fig. 2.7, we are able to reach T_c with approximately $1 \cdot 10^9$ atoms. Due to three-body recombination losses we lose a large fraction of the atoms going from T_c to a pure condensate, depending on the final axial trap frequency. We cannot reach axial trap frequencies below 1 Hz, probably due to a residual curvature field produced by the gradient coils. Even at this very low axial trap frequency, the density is found to be limited by three-body losses. In order to observe the formation of a BEC the temperature is decreased by decreasing the final rf-field frequency. Absorption imaging is used in the vast majority of the Bose-Einstein setups around the world to image the atom cloud and our lab is no exception. In absorption imaging, a collimated laser beam (probe beam) is spatially overlapped with the cloud of atoms and the

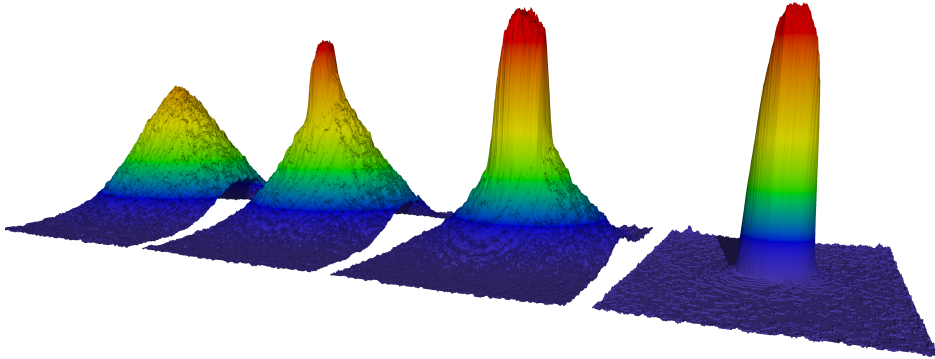


Figure 2.8: A 3D representation of absorption images of (from left to right) a cloud of roughly $1 \cdot 10^9$ atoms cooled to just above the transition temperature, a cloud just after the condensate has formed, a cloud at roughly $T = 0.5T_c$ and an almost pure condensate, containing approximately $2.5 \cdot 10^8$ atoms.

shadow cast by the atoms is recorded on a CCD camera^t. The line-of-sight of the imaging path is along the direction of gravity, which is in the $(\hat{x} + \hat{y})$ direction in our coordinate system. As soon as a BEC has formed, a sharp peak in the density profile is observed in the absorption images. Images taken after the cloud has expanded during a 80 ms time-of-flight have been taken in the final stage of the evaporation process and a 3D false color representation of these images is shown in Fig. 2.8. The distinct difference of the density distribution of the thermal cloud and the BEC seen in these images is used throughout this thesis to distinguish between both components.

Depending on the final axial trap frequency, the final stage of the evaporative cooling is adjusted to prevent shock cooling [37]. If the final stage is executed too fast, size oscillations of the condensate are observed, as well density fluctuations in time-of-flight, indicating phase fluctuations along the axial direction of the cloud [38]. These effects are prevented if the rf-field ramp speed is less than 20 kHz/s close to and below T_c . In table 2.2 the approximate number of condensed atoms is given for typical axial trap parameters, the condensate fraction being approximately 95%. An accurate determination of the number of condensed atoms will be described in detail in Chapter 3.

^t Apogee AP1E, KAF-0401E

AXIAL TRAP FREQUENCY	NUMBER OF CONDENSED ATOMS
15.7 Hz	$40 \cdot 10^6$
3.9 Hz	$140 \cdot 10^6$
2.2 Hz	$200 \cdot 10^6$
1.1 Hz	$300 \cdot 10^6$

Table 2.2: Typical number of condensed atoms for different axial trap frequency ω_{ax} and radial trap frequency $\omega_{\text{rad}}/(2\pi) = 95.6$ Hz.

2.5.2 Atom number and reproducibility optimization

Optimization of the number of captured atoms in the dark-spot MOT is not straight-forward, since the majority of the captured atoms are in the dark-state and do not contribute to the fluorescence. Making the dark-spot less opaque for instance will enlarge the fluorescence, but decrease the density. Coarse optimization of the MOT is done by optimizing the amount of fluorescence found by destructive fluorescence imaging. Fine tuning is done by rapidly cooling to a final rf-field frequency of 2.5 MHz with respect to the bottom of the trap and taking absorption images of the cloud. At this rf-field frequency, the temperature of the cloud is about 15 μK and the optical density is roughly 1. By cooling fast compared to the typical rethermalization times, the efficiency of the evaporative cooling is very sensitive to the initial conditions (collision rate) and therefore a sensitive measure for the densities in the MOT and MT.

In Fig. 2.9 the measured number of atoms is shown for two ramp speeds and different initial number of atoms in the MT. The numbers found here are used as benchmarks for the experimental conditions. The fluctuations in the initial conditions (number of atoms in the MOT and temperature) is estimated from these measurements to be less than 5%. The reproducibility is also influenced by the absorption imaging method used to image the atoms. This method is estimated to yield a shot-to-shot fluctuation of approximately 3% (see § 2.5.3).

The efficiency of spin-polarization is also determined. The increase in the number of atoms after evaporative cooling is larger when starting with a small number of atoms. For typical conditions (roughly $1 \cdot 10^9$ atoms at $T = T_c$), the number of atoms is 1.7 times larger when atoms are spin-polarized before being transferred to the MT.

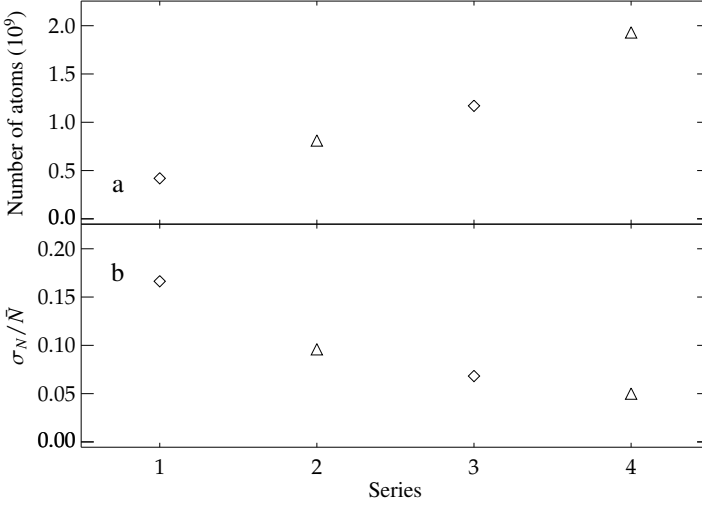


Figure 2.9: The number of atoms \bar{N} (Fig. a) and relative spread in the number of atoms σ_N/\bar{N} (Fig. b) for four different conditions, each point is the average of five measurements taken under the same conditions. Series 1 and 2 correspond to a 15 s (fast) rf-field frequency ramp, enlarging the initial fluctuations. Series 3 and 4 correspond to the same rf-field frequency ramp, but clocked out in 30 s. Measurements 1 and 3 (diamonds) differ from measurements 2 and 4 (triangles) only by the absence of spin-polarization prior to the transfer to the MT and the efficiency of spin-polarization is determined to be a factor of 2 and 1.7 for the fast and slow rf-field ramp speed, respectively. The relative spread is used as a measure of the stability in the initial conditions.

2.5.3 Absorption imaging calibration

Imaging the atoms consists of taking a sequence of three images. The first image obtains the intensity profile $I_{\text{atoms}}(x, y)$ of the probe beam in the presence of the atoms. The second image contains the intensity profile $I_0(x, y)$ of the probe field in absence of the atoms. This image is generally taken after the magnetic trap has been turned off for two seconds. The third image is the intensity profile $I_{\text{bg}}(x, y)$ with neither the probe beam nor the atoms and functions as a background image. The resulting normalized intensity profile $I(x, y)$ of the atoms is given by

$$I(x, y) = \frac{I_{\text{atoms}}(x, y) - I_{\text{bg}}(x, y)}{I_0(x, y) - I_{\text{bg}}(x, y)} \quad (2.8)$$

where the subtraction and division is performed on a pixel-by-pixel basis.

The probe beam is tuned on resonance with the $F_g = 1 \rightarrow F_e = 1$ transition, has an intensity of $I = 10^{-4}s_0$ and is pulsed on for 200 μs to avoid heating of the

cloud. Measuring these dense clouds with absorption imaging can be challenging, since high optical densities ($OD \gtrsim 4$) cannot be accurately determined due to the limited dynamic range of the absorption imaging scheme in combination with the noise of the CCD camera. Since the *in situ* optical density of a BEC is of the order of 500 the density has to be decreased by a large amount.

A straight-forward way to decrease the density is by turning off the confinement, causing the cloud to expand and fall due to gravity. Detuning the laser from resonance lowers the optical density as well, but the real part of the index of refraction will no longer be (close to) zero and the resulting lensing effect of the cloud distorts the absorption image.

Expansion initiated by switching down the magnetic confinement complicates the retrieval of the column density due to the finite time needed to switch the magnetic fields. Furthermore, shot-to-shot fluctuations as well as systematic errors can be introduced in determining σ_{eff} (Eq. (2.6)) due to the strong dependence on δ and the dependence of C_{ge} and the (initial) state the atoms are in; as long as the MT is on, all atoms are in the $|F_g = 1, m_F = -1\rangle$ state and when probing with linear polarized light yields $C_{ge} = 5/12$. During expansion and in absence of the magnetic field the quantization axis of the atoms is no longer well defined and assuming random distribution over the magnetic sub-levels $C_{ge} = 5/18$. However, residual magnetic fields can cause the atoms to be polarized in some direction. As the atoms fall due to gravity during time-of-flight, the quantization axis might be time dependent. To prevent extra uncertainties due to this effect, we apply a small extra magnetic field during time-of-flight along the z-axis. Furthermore, since the atoms fall a significant distance toward the camera, the position of the imaging lens is adjusted for each expansion time. The absorption imaging method is calibrated to prevent systematic errors caused, for instance, by incorrectly applying the magnetic field that maintains the quantization axis or due to an incorrect probe frequency.

The calibration is achieved by generating clouds just below the transition temperature, the condensate fraction never exceeding 5%. The increase or decrease of the condensate fraction is a sensitive measure of the stability of final conditions since it approximately scales with the temperature as

$$N_c \approx N \left(1 - \left(\frac{T}{T_c} \right)^3 \right), \quad (2.9)$$

with N_c the number of condensed atoms and $N = (N_c + N_{\text{ex}})$, where N_{ex} is the number of excited (thermal, non-condensed) atoms. Furthermore, the number of atoms at T_c is approximated by

$$N(T = T_c) = \beta \left(\frac{k_B T_c^0}{\hbar \bar{\omega}} \right)^3 \zeta(3), \quad (2.10)$$

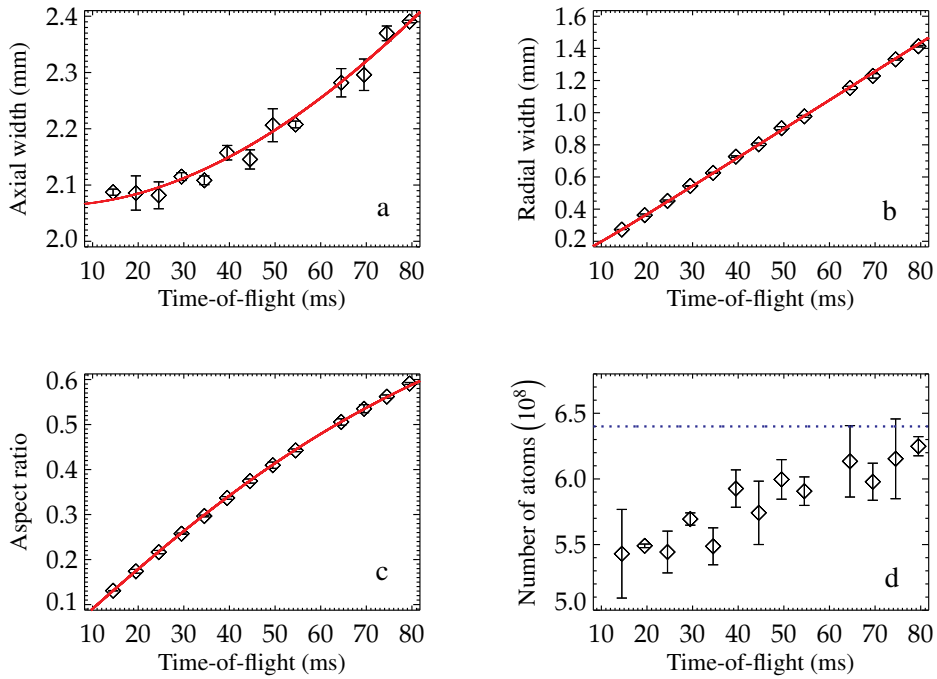


Figure 2.10: Temperature measurement of clouds at the transition temperature. Figure a shows the axial width of the thermal cloud as a function of time-of-flight. In Fig. b the radial width of the thermal cloud is shown as a function of time-of-flight. The solid lines in Fig. a and Fig. b are the result of a least-square fit of the data to Eq. (2.11). The aspect ratio as a function of time-of-flight is shown in Fig. c and Fig. d shows the number of atoms based on the measured absorption profile and Eq. (2.12). The dotted line gives the calculated number of atoms based on the measured temperature and Eq. (2.10). Note that the number of atoms is halved with respect to our typical atom numbers to reduce the optical density.

where $\bar{\omega}$ is the geometric mean of the three trap frequencies in the Cartesian directions, $\zeta(x)$ is the Riemann zeta function and β is a density dependent parameter to compensate for the down shift of the transition temperature T_c with respect to T_c^0 , the transition temperature in the absence of interactions. The effect of static interaction between the thermal cloud and the BEC is studied in Chapter 3. The parameter β is typically in the range between $1.04 < \beta < 1.08$.

The clouds at T_c are imaged after free expansion at different time-of-flight τ and the measured width $\rho(\tau)$ is fitted to

$$\rho(\tau) = \sqrt{\rho_0^2 + \frac{k_B T}{m} \tau^2}, \quad (2.11)$$

where $\rho_0^2 = k_B T / (m\omega^2)$ is the initial width. The results of the measurement are shown in Fig. 2.10.

The expansion of the cloud in the axial and radial direction as a function of the time-of-flight is shown in Figs. 2.10a and 2.10b. In the radial direction the initial size of the cloud is negligible compared to the size during expansion, and the size in this direction is used to determine the temperature of the cloud, yielding $T = 0.887(3) \mu\text{K}$, in agreement with the temperature determined when using the axial expansion. All measurements contain a small condensate and therefore confirm the temperature T is below the transition temperature. We assume $T \approx T_c$ and Eq. (2.10) to determine the number of atoms. The total absorption in each image is a measure of the number of atoms as well. The intensity distribution in absorption imaging is found using Eq. (2.4), written as

$$I(x, z) = I_0(x, z)e^{-\sigma_{\text{eff}} n_c(x, z)}, \quad (2.12)$$

where $n_c(x, z)$ is the column density and the effective cross section σ_{eff} is given by Eq. (2.6). The number of atoms based on the total absorption is shown in Fig. 2.10d, as well as the number of atoms based on the transition temperature. The ratio between both measures is used to calibrate the absorption imaging technique and reduces the systematical error. With this procedure, the shot-to-shot stability of absorption imaging is determined at approximately 3%. This value is in agreement with the estimated stability of the probe frequency, $\delta = 0 \pm 1.0 \text{ MHz}$ corresponding to a 4% fluctuation in the measured absorption. The increase in the number of atoms as a function of expansion time is attributed to the difficulty of measuring high optical densities. We find the $\text{OD} > 4$ for expansion times less than 45 ms, but accurate measurements are expected for $\text{OD} \lesssim 3$. Note that the number of atoms in the measurements presented in Fig. 2.10 is halved with respect to typical atom numbers to reduce the optical density. The stability of both frequency and intensity of the laser light used for cooling and trapping the atoms allows us to generate cold clouds with only small fluctuations in the final conditions. The stability is of great importance, since we use imaging techniques that are destructive. Typically, a new cloud

is prepared every 90 s and most measurement series take between 30 minutes and a few hours. The accuracy of the measurement series is determined by the reproducibility of the preparation of new clouds on this time scale.

2.6 CONCLUSION & OUTLOOK

In this chapter the most important steps to make a large atom number Bose-Einstein condensate are described.

A sodium oven, which produces a large flux of $5 \cdot 10^{12}$ atoms/s is efficiently slowed down using a Zeeman slower resulting in an atom flux of $3 \cdot 10^{11}$ atoms/s passing the capture area of the MOT at a velocity close to the capture velocity of the MOT.

The dark-spot MOT technique is used to reach high densities in the MOT. Spin polarization of the captured atoms allows us to transfer 60 % of these atoms to the MT. Starting with this large a number of atoms allows for efficient evaporative cooling, and the number of atoms is reduced only by a factor of 100 before T_c is reached. To limit the density, the trap has to be decompressed, resulting in highly elongated cigar-shaped clouds with an aspect ratio up to 1 : 85. T_c is reached with more than $1 \cdot 10^9$ atoms, and depending on the trap configuration, up to $3 \cdot 10^8$ atoms can be cooled down to the Bose-Einstein condensed state. This is by far the largest number of condensed alkali metal atoms and an ideal starting point for the study of properties of a hydrodynamic thermal clouds and the two-fluid regime.

PHASE CONTRAST IMAGING OF BOSE-EINSTEIN CONDENSATES AT FINITE TEMPERATURES

Abstract

Phase contrast imaging is used to observe Bose-Einstein condensates (BECs) at finite temperatures *in situ*. The imaging technique is used to accurately derive the absolute phase shift of a probe laser beam due to both the condensate and the thermal cloud. The accuracy of the method is enhanced by using the periodicity of the intensity signal as a function of the accumulated phase. The measured density profiles can be described using a two relevant parameter fit, in which only the chemical potential and the temperature are to be determined. This allows us to directly compare the measured density profiles to different mean-field models in which the interaction between the condensed and thermal atoms is taken into account to various degrees.

3.1 INTRODUCTION

In the field of ultra-cold atomic physics the two commonly used techniques to image a cloud of atoms are absorption imaging and fluorescence imaging, i. e. imaging the cloud's absorbed or radiated intensity, respectively. In absorption imaging the shadow cast in a probe beam by the cloud of atoms is recorded on a CCD camera. From the resulting image the spatial extent of the cloud and the optical density, proportional to the column density along the line-of-sight of the probe beam, can be derived. For dense clouds absorption imaging becomes unreliable, since for optical densities of the order of 4 the dynamic range of the absorption imaging technique is insufficient to accurately determine the intensity in the shadowed region [39]. For Bose-Einstein condensates (BECs) the typical *in situ* optical density is of the order of 500 and the image gets completely "blacked out", making it impossible to extract the column density from the image. The fluorescence imaging technique critically depends on the intensity and the frequency of the probe beam. Furthermore, for high densities the cloud becomes

This chapter is based on a paper, which is submitted to Physical Review A as *Phase contrast imaging of Bose-Einstein condensed clouds*, R. Meppelink, R. A. Rozendaal, S. B. Koller, J. M. Vogels, and P. van der Straten

opaque and atoms in the center of the cloud are not subjected to the same intensity as atoms on the edge of the cloud.

One way to reduce the optical density is to reduce the atom-photon cross section by choosing a large probe beam detuning. However, for nonzero detuning the real part of the index of refraction of the atoms becomes nonzero and the cloud behaves like a gradient-index lens. This results in a refraction of the probe beam and leads to distortion of the images. The resulting images cannot be used for a relative or absolute column density measurement, since the magnitude of this effect has a spatial dependence. Detuning the probe beam further from resonance reduces the index of refraction but leaves the cloud virtually transparent before the refraction is sufficiently reduced.

The optical density can successfully be decreased by reducing the atomic density. The cloud is allowed to expand during a specific time-of-flight (tof) and an image is recorded as soon as the optical density is of the order of 2. Although absorption imaging after expansion is the commonly used technique in this field, expansion of the cloud introduces some difficulties as well. First, if the cloud is a BEC at finite temperature there is no accurate description available of the expansion of the cloud. Second, the quantization axis of the cloud is no longer well-defined since the magnetic fields are turned off. As a result, the effective cross section for the polarized probe beam becomes ambiguous. As a consequence both absorption imaging and fluorescence imaging cannot be applied to accurately determine the column density of dense clouds.

Some techniques have been developed to image dense clouds by using strong saturation in both absorption [40] and fluorescence [41] imaging. However, the high-intensity regime has to be calibrated based on the low-intensity regime and the latter regime is imaged after expansion. As a consequence the issues raised above about imaging after expansion apply to the strong saturation techniques as well, although cloud can be imaged *in situ*.

Alternatively, phase contrast imaging (PCI) has been successfully applied to image dense atomic clouds [42–44]. In PCI the real part of the index of refraction is measured. The detuning can be chosen in such a way that the refraction is small but the phase shift due to the index of refraction remains substantial. PCI can be used to image BECs in a nondestructive way, since the number of scattered photons becomes negligible for large detuning. Other techniques based on dispersive light scattering, such as diffraction-contrast imaging of cold atoms [45] and nondestructive spatial heterodyne imaging of cold atoms [46] have been demonstrated on dense thermal clouds.

Here, we use PCI to measure the *in situ* density distribution of dense BECs at finite temperatures absolutely and accurately. By choosing a smaller detuning compared to the nondestructive PCI schemes, the density of the thermal cloud and the BEC are determined accurately for all typical temperatures. This allows

us to directly study the interplay between the condensed and thermal atoms and the influence of this interaction on the transition temperature for condensation.

This chapter begins with a detailed description of the PCI technique and the way it is applied to a cold Bose gas. Next, the accuracy is demonstrated in two experiments. In the first experiment, described in § 3.5.3, the number of condensed atoms is measured with an accuracy below 5% in a single shot. In the second experiment, described in § 3.5.4 the growth of the condensate is studied as a function of the temperature. In this measurement, the interaction between the condensed and thermal atoms is studied directly. Furthermore, measurements around the temperature where a BEC is formed are used to determine the transition temperature.

3.2 THEORETICAL DESCRIPTION OF PCI

3.2.1 *Imaging the phase*

It is possible to image a cloud of atoms by illuminating the cloud with a probe beam and record the shadow cast due to the absorption of the atoms on a CCD camera. Since the optical density is measured, this technique probes the imaginary part of the complex index of refraction \mathcal{N} of the atomic cloud. In contrast, the imaging technique described in this chapter probes the real part of \mathcal{N} . This technique is used in the phase contrast microscope which is developed by Zernike in 1933. In 1953 Zernike was awarded the Nobel prize “for his demonstration of the phase contrast method, especially for his invention of the phase contrast microscope” [47].

In general, the complex phase ϕ accumulated by the light in a medium such as a cloud of atoms can be expressed as $\phi_{\text{atoms}} = \phi' + i\phi''/2$, with ϕ'' the optical density. Writing the electric field of the probe beam as $E_{\text{probe}} = E_0 \exp(i\phi)$ with E_0 the amplitude of the light field, the electric field after passing a cloud of atoms can be written as

$$E = E_{\text{probe}} + E_{\text{atoms}} = E_{\text{probe}} + E_{\text{probe}}(e^{i\phi_{\text{atoms}}} - 1), \quad (3.1)$$

where the electric field is split in two parts: the part that is diffracted by the atoms, E_{atoms} , and the part that is not, E_{probe} . In absorption imaging the phase information is lost on a CCD camera, since the intensity I is measured as $I = c\varepsilon_0 EE^*/2 = I_0 e^{-\phi''}$ where $I_0 = c\varepsilon_0 |E_0|^2/2$, c is the speed of light and ε_0 is the vacuum permittivity. So the real phase term ϕ' cancels and only the absorption is measured. In the simplest form of PCI, the non-diffracted part of the probe light (first term on the RHS of Eq. (3.1)) is blocked. The light that arrives at the camera is the light which is diffracted by the atoms, $E = E_{\text{probe}}(\exp(i\phi_{\text{atoms}}) - 1)$. Now

the phase information no longer cancels and the intensity on the camera is given by

$$I = 2I_0(1 - \cos(\phi_{\text{atoms}})), \quad (3.2)$$

where the arbitrary phase of the probe beam cancels. This technique is referred to as dark-field imaging and has been successfully used to image ^{23}Na atoms in the early days of experimental BEC physics [44]. An important experimental drawback of this method is the absence of probe light on the camera preventing the normalization of the intensity profile, which makes this technique not suitable to measure the absolute phase shift. However, the relative signal can be used to study the spatial distribution.

A more elaborate way of converting the accumulated phase into an intensity profile is by phase shifting the non-diffracted light instead of blocking it, in the same way as the phase contrast microscope works. The non-diffracted light is the plane wave part of the beam, which can be phase-shifted by placing a small transparent object with a refractive index in the probe beam in such a way that only the plane wave part of the beam propagates through it. This object will be called a phase spot. The plane wave part propagating through the phase spot accumulates a phase θ , changing Eq. (3.1) to

$$E = E_{\text{probe}}e^{i\theta} + E_{\text{probe}}(e^{i\phi_{\text{atoms}}} - 1). \quad (3.3)$$

Now, the intensity is given by

$$I = I_0(3 - 2\cos(\theta) + 2\cos(\theta - \phi_{\text{atoms}}) - 2\cos(\phi_{\text{atoms}})), \quad (3.4)$$

where the arbitrary phase of the probe beam cancels. The probe beam is not blocked and it is possible to derive the absolute phase shift, since the intensity profile I_0 can be measured and used for normalization. This technique has also been successfully applied to image ^{23}Na atoms [43]. The implementation of PCI described in Ref. [43] uses a detuning of the probe beam, which is large compared to the atomic resonance and the absorption of the light by the atoms is therefore reduced to a degree that it is no longer destructive. This allows for taking multiple images of the same BEC.

In our experiment we do not focus on the ability to make a nondestructive image but we use the periodicity of the intensity as a function of ϕ_{atoms} (see Eq. (3.4)) to accurately determine the accumulated phase of both the BEC and the thermal cloud. In recent years, different schemes are proposed derive the phase information of a cloud of cold atoms [46, 48], but the accumulated phase has never been used for accurate quantitative measurements of the density distribution of BECs at finite temperatures.

3.2.2 Index of refraction of a cold gas

We continue with a detailed description of the phase shift of an electro-magnetic wave propagating through a cloud of spin-polarized atoms in order to relate ϕ_{atoms} to the atomic density. The phase shift is caused by the modification of the probe field by the atomic dipoles, so we start with an expression of the polarizability of one atom. The polarizability tensor $\overleftarrow{\alpha}$ in the low-intensity limit and $\delta \ll \omega$ is given by [49]

$$\overleftarrow{\alpha} = \sum_{g,g',e} \frac{i}{\hbar} \frac{1}{\gamma/2 - i\delta} \langle g | \vec{\mu}_{ge} | e \rangle \langle e | \vec{\mu}_{eg} | g' \rangle \langle g' | \sigma_{gg} | g \rangle, \quad (3.5)$$

where the natural linewidth γ is given by

$$\gamma = \frac{\omega^3 \mu^2}{3\pi\epsilon_0 \hbar c^3}. \quad (3.6)$$

Here, $\vec{\mu}_{eg,ge}$ are the electric-dipole operators, σ_{gg} is the density matrix, δ is the detuning and ω is the probe frequency. In the experiment various linear polarizations of the light field have to be dealt with, so the dependence of the polarizability $\overleftarrow{\alpha}$ on the polarization has to be determined. We define the angle β as the angle between the z -axis of the atomic cloud and the (linear) polarization direction of the light field which is in the (x, z) plane. In this system, the line-of-sight is along the y -axis. In order to evaluate Eq. (3.5) for different polarizations, a fixed polarization axis is chosen parallel to the polarization of the light field and Eq. (3.5) is evaluated in this frame, in which conveniently only $\Delta M = 0$ transitions are induced. Furthermore, only one component of the polarizability tensor will contribute in this frame and the polarizability becomes a scalar. Since all atoms in the trap are in the $|F_g, M_g\rangle = |1, -1\rangle$ state with respect to the z -axis of the magnetic field confining the atoms, the density matrix σ_{gg} only has one nonzero element, which makes the calculation of the rotation from the magnetic z -axis to the polarization axis of the light field straight-forward.

Rotating the density matrix of the ground state σ_{gg} is achieved using

$$\hat{\sigma}_{gg}(\beta) = \mathcal{R}_y(\beta)^\dagger \sigma_{gg} \mathcal{R}_y(\beta), \quad (3.7)$$

where the rotation matrix $\mathcal{R}_y(\beta)$ for rotating a system around the y -axis over an angle β for a system with $J_g = 1$ can be found using Wigner's formula as [50]

$$\mathcal{R}_y(\beta) = \begin{pmatrix} \cos^2(\frac{\beta}{2}) & \frac{\sin(\beta)}{\sqrt{2}} & \sin^2(\frac{\beta}{2}) \\ -\frac{\sin(\beta)}{\sqrt{2}} & \cos(\beta) & \frac{\sin(\beta)}{\sqrt{2}} \\ \sin^2(\frac{\beta}{2}) & -\frac{\sin(\beta)}{\sqrt{2}} & \cos^2(\frac{\beta}{2}) \end{pmatrix}, \quad (3.8)$$

Since the two dipole moment operators $\vec{\mu}_{eg}$ do not change the M -state of the atoms, only the diagonal elements of Eq. (3.5) play a role and we end up with

$$\alpha = \frac{2i}{\hbar\gamma} \sum_{g,e} \frac{\langle F_g, M_g | \vec{\mu}_{ge} | F_e, M_e \rangle^2 \langle F_g, M_g | \hat{\sigma}_{gg}(\beta) | F_g, M_g \rangle}{1 - 2i\delta_e/\gamma}. \quad (3.9)$$

Furthermore, we can define the square of the Clebsch-Gordan coefficients C_{F_e, M_e} (transition strength) as

$$C_{g,e} = \langle F_g, M_g | \vec{\mu}_{ge} | F_e, M_e \rangle^2 / \mu^2, \quad (3.10)$$

and obtain using Eq. (3.6)

$$\alpha = \frac{i\epsilon_0 c \sigma_\lambda}{\omega} \sum_{g,e} \frac{C_{g,e} \langle F_g, M_g | \hat{\sigma}_{gg}(\beta) | F_g, M_g \rangle}{1 - 2i\delta_e/\gamma}, \quad (3.11)$$

where δ_e is the detuning with respect to transition $F_g \rightarrow F_e$ and σ_λ the cross section for absorption of light:

$$\sigma_\lambda \equiv \frac{3\lambda^2}{2\pi}. \quad (3.12)$$

For sodium atoms in the $|F_g, M_g\rangle = |1, -1\rangle$ state this results in

$$\alpha = \frac{i\epsilon_0 c \sigma_\lambda}{\omega} \sum_e \frac{D_{F_e}(\beta)}{1 - 2i\delta_e/\gamma}, \quad (3.13)$$

where

$$D_0(\beta) = \frac{4}{24} \sin^2(\beta), \quad (3.14a)$$

$$D_1(\beta) = \frac{5}{24} (1 + \cos^2(\beta)) + \frac{6}{24}, \quad (3.14b)$$

$$D_2(\beta) = \frac{6}{24} + \frac{1}{24} \sin^2(\beta). \quad (3.14c)$$

For alkali metal atoms the polarizability is independent of the angle β if the detuning δ is large compared to the hyperfine splitting of the excited state. In that limit the numerator of the sum in Eq. (3.13) is $\frac{2}{3}$ with no angular dependence. Finally, the complex index of refraction \mathcal{N} is given by

$$\mathcal{N}^2 = 1 + \frac{\rho\alpha}{\epsilon_0}, \quad (3.15)$$

with ρ the density. Note that for atoms confined in a potential the density is not homogeneous and ρ depends on the position, $\rho = \rho(x, y, z)$.

The index of refraction given by Eq. (3.15) is only valid for low densities. For higher densities, the dipole moment of an atoms is influenced by the internal field of the surrounding atoms. This results in a modification of the refractive index, which is accounted for by the Lorentz-Lorenz equation [51]

$$\mathcal{N}^2 = 1 + \frac{\rho\alpha/\varepsilon_0}{1+C}, \quad (3.16)$$

where C is given by

$$C = -\frac{1}{3}\rho\alpha/\varepsilon_0. \quad (3.17)$$

Since the atoms being imaged are bosons instead of classical particles, the index of refraction will be modified further due to bunching of the atoms. Two terms are added to Eq. (3.17). The first term accounts for modifications due to the enhanced photon scattering cross section caused by the quantum statistics of the atoms. The second term describes the modified refractive index induced by resonant Van der Waals interaction, resulting in an increase of almost 10% in both the real part and the imaginary part of the refractive index [52].

We have derived the modifications along the lines of Ref. [52] and have confirmed the result for the detuning and densities reported in that paper. We found modifications to the complex index of refraction strongly depend on the chosen detuning and therefore on α . In Ref. [52], $\delta \sim \gamma$, while we are in the regime $\delta \gg \gamma$. For our parameters, the real part of the index of refraction does not change significantly. However, we do find an enhancement of the absorption by a factor of 3. Since the overall absorption is very small, up to four percent at the detuning used, enhanced absorption does not influences the intensity profile significantly. As a result, we expect the measured phase to change less than one percent due to this effect.

3.2.3 *Imaging the atomic density*

The image of a cloud of atoms recorded on a CCD camera yields the column density of the cloud, that is the density profile integrated along the probe line-of-sight. The column density can be linked to the complex index of refraction in the following way. In general, light passing through a medium with an index of refraction \mathcal{N} over a distance l accumulates a complex phase ϕ given by

$$\phi = k(\mathcal{N} - 1)l, \quad (3.18)$$

where $k = 2\pi/\lambda$. Since the index of refraction depends on the position, the accumulated phase is written as

$$\phi(x,z) = k \int \left(\sqrt{1 + \frac{\rho(x,y,z)\alpha/\varepsilon_0}{1+C}} - 1 \right) dy. \quad (3.19)$$

Since $|\rho\alpha/\varepsilon_0| \ll 1$ the index of refraction can be approximated as

$$\mathcal{N} = \sqrt{1 + \frac{\rho\alpha/\varepsilon_0}{1+C}} \approx 1 + \frac{\rho\alpha}{2\varepsilon_0}. \quad (3.20)$$

Under typical experimental conditions $|\rho\alpha/\varepsilon_0|$ is 10^{-2} , introducing only a small error by using this approximation. Now, Eq. (3.19) can be written as

$$\phi(x, z) = k \frac{\alpha}{2\varepsilon_0} \int \rho(x, y, z) dy = k \frac{\alpha}{2\varepsilon_0} \rho_c(x, z), \quad (3.21)$$

where the integration is along the line-of-sight y and $\rho_c(x, z)$ is the column density.

The real part of $\phi(x, z)$, proportional to $\text{Re}(\alpha)$, yields the phase shift, whereas the imaginary part, proportional to $\text{Im}(\alpha)$, yields the absorption. Since α is constant for fixed detuning δ , the phase shift is directly proportional to the column density. Since Eq. (3.13) satisfies the Kramers-Kronig relation

$$\text{Re}(\mathcal{N}) - 1 = \left(\frac{2\delta}{\gamma} \right) \text{Im}(\mathcal{N}), \quad (3.22)$$

the ratio between the phase shift and the absorption is constant for a given detuning.

3.3 PCI SETUP

In order to create a phase contrast image of the atoms, the plane wave part of the probe field has to be phase shifted as is described in § 3.2.1. This is commonly achieved by Fourier transformation using a lens. The concept of the imaging setup used in our experiment is schematically shown in Fig. 3.1. A two-lens setup is used to generate a sharp image of the atoms on a camera. The first lens L_1 with focal distance $f_1 = 250$ mm is placed at a distance f_1 from the center of the magnetic trap. The second lens L_2 with focal distance $f_2 = 750$ mm is placed at a distance f_2 from the CCD camera. The distance between both lenses is $d = 150$ mm. The combination of both lenses creates a sharp image of the cloud on the CCD camera with a magnification $M = f_2/f_1 = 3.0 \pm 0.05$ where the uncertainty is the result of the uncertainty in the focal distance of the lenses.

In order to shift the phase of the plane wave part of the light a phase spot is placed in the back focal plane (Fourier plane) of the two lenses, which lies for these parameters beyond the second lens L_2 . This position can be found easily in the experiment, since the parallel probe beam has its waist at the back focal plane and therefore the phase spot is placed at this position.

Figure 3.2 shows the intensity I/I_0 as a function of the accumulated phase ϕ_{atoms} for different values of θ based on Eq. (3.4). In all experiments described

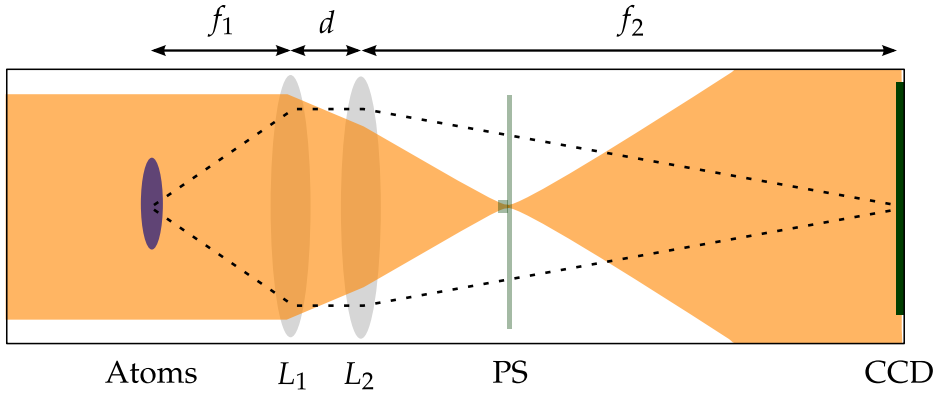


Figure 3.1: Schematic representation of the PCI setup. The atoms located at the center of the trap are imaged with lens L_1 with focal distance f_1 which is placed at a distance f_1 from the center. A sharp image is created by placing the lens L_2 at distance d from L_1 with focal length f_2 at a distance f_2 from the CCD camera. The phase spot (PS) is placed in the focal plain of the non-diffracted probe beam.

here, $\theta = \pi/3$ is used. This value is chosen since it yields a maximum visibility $(I_{\max} - I_{\min}) / (I_{\max} + I_{\min}) = 1$ and a dynamic range $I_{\max} - I_{\min} = 4I_0$. A visibility of 1 is reached only for $\theta = \pi/3$, as can be seen in Fig. 3.2. Furthermore the response is approximately linear for small accumulated phases.

For technical reasons, the $\pi/3$ spot consists of a glass plate with a dimple instead of a spot on top. This dimple is made by dry-etching a $50\ \mu\text{m}$ diameter round dimple with a depth of $5\lambda / (6(\mathcal{N} - 1)) = 1071 \pm 15\ \text{nm}$ in a $50\ \text{mm}$ round fused silica glass plate of $4\ \text{mm}$ thickness [53]. Light propagating through the dimple accumulates $5\pi/3$ less phase than the light propagating through the full thickness of the plate and thus $\theta = +\pi/3$.

The atoms are imaged using an Apogee AP1E camera with a Kodak KAF-0401E chip camera with a pixel size of $9 \times 9\ \mu\text{m}^2$. At the magnification $M = 3.0$, the effective camera resolution of $3.0\ \mu\text{m}$ per pixel is comparable to the diffraction limit $x_{\text{res}} \approx 1.22\lambda f_1 / (2r) \approx 3.6\ \mu\text{m}$ of the imaging lens L_1 with radius $r = 25\ \text{mm}$ for probe light with a wavelength $\lambda = 589\ \text{nm}$.

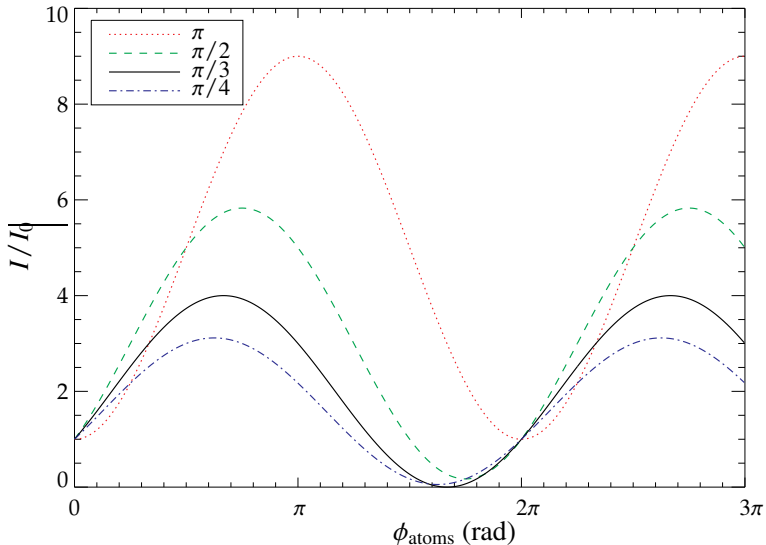


Figure 3.2: The phase contrast signal I/I_0 as a function of the accumulated phase ϕ_{atoms} for different phases $\theta = \pi, \pi/2, \pi/3, \pi/4$ of the phase spot.

3.4 DENSITY DISTRIBUTION

3.4.1 Three models for BECs at finite temperatures

A phase contrast image of a BEC at nonzero temperature contains the column density distribution of the two-component cloud, i.e. a BEC and a thermal cloud which can be distinguished from each other due to their distinct density distributions. In order to derive the relevant parameters from such an image, like the thermal (excited) density n_{ex} , the condensate (ground state) density n_{c} , and the temperature T , the measured profiles are fitted to a theoretical model describing the cloud. Various models exist in literature in which the interaction between the condensed and thermal atoms are taken into account to various degrees. In this chapter we compare our measurements to three of these models. The first model is the commonly used bimodal distribution in which all interactions between the two components are ignored. This model is used in to describe the vast majority of the experiments of cold Bose gases [39]. In the second model only the effect of the condensed atoms on the thermal atoms is taken into account. The third model incorporates the effect of the density distribution of the thermal atoms on the condensed atoms as well. Below, the density distribution of the thermal cloud and the BEC in each of these models are described consecutively.

In the first model, referred to as the ideal model, the chemical potential is given by $\mu = V_{\text{ext}}(\mathbf{r}) + n_c(\mathbf{r})U_0$, where $U_0 = 4\pi\hbar^2 a/m$ is the interaction parameter for bosons with s -wave scattering length a and mass m [54]. Since there are no interactions between condensed atoms with density n_c and thermal atoms with density n_{ex} , μ does not depend on n_{ex} . In the ideal model n_{ex} is given by

$$n_{\text{ex}}(\mathbf{r}) = \int \frac{d\mathbf{p}}{(2\pi\hbar)^3} \frac{1}{e^{(\varepsilon(\mathbf{r})-\mu)/k_B T} - 1}, \quad (3.23)$$

where ε is given by

$$\varepsilon(\mathbf{r}) = \frac{p^2}{2m} + V_{\text{ext}}(\mathbf{r}). \quad (3.24)$$

In this approximation both n_{ex} and n_c can be derived analytically yielding the bimodal density distribution, the sum of a Maxwell-Bose distribution modeling the thermal cloud and a Thomas-Fermi (TF) distribution modeling the BEC. In this approximation n_{ex} is given by

$$n_{\text{ex}}(\mathbf{r}) = \text{Li}_{3/2}(\tilde{z}e^{-V_{\text{ext}}(\mathbf{r})/k_B T}) / \lambda_{\text{dB}}^3, \quad (3.25)$$

where the de Broglie wavelength is given by $\lambda_{\text{dB}} = \sqrt{(2\pi\hbar^2)/(mk_B T)}$ and $\tilde{z} = \exp(\mu/(k_B T))$ is the fugacity. $\text{Li}_{3/2}(z)$ is the Bose function, given by $\text{Li}_n(z) \equiv \sum_{k=1}^{\infty} z^k/k^n$ and

$$V_{\text{ext}} = \frac{1}{2}m(\omega_{\text{rad}}^2 r_x^2 + \omega_{\text{rad}}^2 r_y^2 + \omega_{\text{ax}}^2 r_z^2), \quad (3.26)$$

is the external potential. In the TF approximation n_c is given by

$$n_c(\mathbf{r}) = \frac{\mu}{U_0} \left[1 - \left(\frac{r_x}{R_{\text{rad}}} \right)^2 - \left(\frac{r_y}{R_{\text{rad}}} \right)^2 - \left(\frac{r_z}{R_{\text{ax}}} \right)^2 \right], \quad (3.27)$$

where $R_{\text{rad,ax}}$ are the TF radii of the condensate given by

$$R_{\text{rad}} = \sqrt{\frac{2\mu}{m\omega_{\text{rad}}^2}}, \quad (3.28a)$$

$$R_{\text{ax}} = \sqrt{\frac{2\mu}{m\omega_{\text{ax}}^2}}. \quad (3.28b)$$

Since $\omega_{\text{rad}}/\omega_{\text{ax}} \approx 50$ in the experiments described here and thus $R_{\text{rad}} \ll R_{\text{ax}}$ the clouds are cigar shaped. The number of condensed atoms N_c is found by integrating n_c over \mathbf{r} and yields

$$N_c = \int n_c(\mathbf{r}) d\mathbf{r} = \frac{8\pi}{15} \left(\frac{2\mu}{m\bar{\omega}^2} \right)^{3/2} \frac{\mu}{U_0}. \quad (3.29)$$

Integration of the density over the line-of-sight yields the column density, which is the property being measured in the experiments.

The second model, denoted as the semi-ideal model, does include interactions, but only the contribution of the mean-field potential of the condensate to the thermal density distribution is taken into account [55]. Therefore, μ remains unchanged: $\mu = V_{\text{ext}}(\mathbf{r}) + n_c(\mathbf{r})U_0$, but the energy of the thermal atoms is changed due to the mean-field potential of the condensed atoms and written as

$$\varepsilon^2(\mathbf{r}) = \left(p^2/(2m) + 2n_c(\mathbf{r})U_0 + V_{\text{ext}}(\mathbf{r}) - \mu \right)^2 - (n_c(\mathbf{r})U_0)^2. \quad (3.30)$$

We calculate the density distribution in this semi-ideal model by numerical integration of Eq. (3.23), where $\varepsilon(\mathbf{r})$ is given by Eq. (3.30) [54]. The shape of the density distribution of the condensate remains unchanged, but the repulsion of the mean-field potential of the condensate causes the thermal atoms to be repelled from the center, which results in the shape shown in Fig. 3.3. In order to have the same total number of atoms and temperature in Fig. 3.3, the chemical potential is different in both models. The decrease in density in the center is the result of the repulsion due to the mean-field potential of the condensed atoms and therefore absent in the noninteracting distribution. Due to the lower central density the resulting condensate fraction is lower in the semi-ideal model compared to the noninteracting model for the same total number of atoms $N = N_{\text{ex}} + N_c$ and temperature T .

In the third model the mean-field effect of the thermal cloud on the condensate is taken into account as well. This model corresponds to the Popov approximation in the TF limit, so we refer to this model as the Popov model [54]. The chemical potential is now given by $\mu = V_{\text{ext}}(\mathbf{r}) + [n_c(\mathbf{r}) + 2n_{\text{ex}}(\mathbf{r})]U_0$. The expression for the density of the excited atoms in the Popov approximation is given by

$$n_{\text{ex}}(\mathbf{r}) = \int \frac{d\mathbf{p}}{(2\pi\hbar)^3} \frac{p^2/2m + 2n(\mathbf{r})U_0 + V_{\text{ext}}(\mathbf{r}) - \mu}{\varepsilon(\mathbf{r})} \frac{1}{e^{\varepsilon(\mathbf{r})/k_B T} - 1}, \quad (3.31)$$

with $n = n_{\text{ex}} + n_c$ and where, in the semi-classical approximation, $\varepsilon(\mathbf{r})$ is given by

$$\varepsilon^2(\mathbf{r}) = \left(p^2/(2m) + 2n(\mathbf{r})U_0 + V_{\text{ext}}(\mathbf{r}) - \mu \right)^2 - (n_c(\mathbf{r})U_0)^2. \quad (3.32)$$

Now, the resulting density distribution of both n_{ex} and n_c is found by numerical integration of Eq. (3.31), where an iterative procedure is used to find a self-consistent solution. The difference between the semi-ideal model and the Popov model is shown in Fig. 3.4, focusing on the density distribution of the condensed atoms. The density distribution of the thermal atoms as shown in Fig. 3.3 results in a higher effective potential for the condensed atoms. This effect results in a compression of the density distribution of the condensate compared to the distribution calculated using the semi-ideal model.

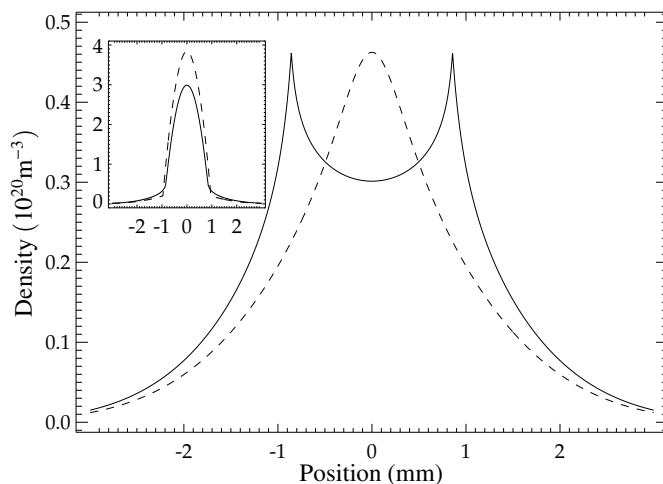


Figure 3.3: The density distribution of a thermal cloud n_{ex} calculated using the noninteracting model (dashed line) and the semi-ideal model (solid line), for $T = 0.9 \mu\text{K}$, $N = 1 \cdot 10^9$ atoms for the typical experimental trap parameters. The inset shows the total density distribution $n_{\text{ex}} + n_{\text{c}}$ for both models.

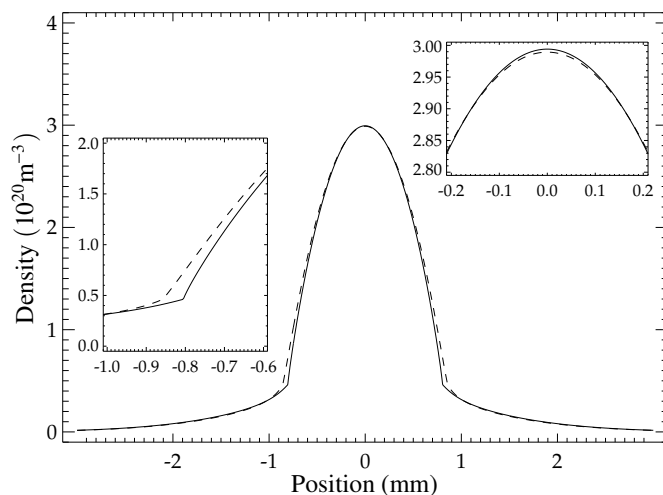


Figure 3.4: The combined density distribution of the thermal cloud and condensate $n_{\text{ex}} + n_{\text{c}}$ calculated using the semi-ideal model (dashed line) and the Popov model (solid line) for $T = 0.9 \mu\text{K}$, $N = 1 \cdot 10^9$ atoms and the typical experimental trap parameters. The left and right insets show an enlargement of the edges and the center of the condensate, respectively.

3.4.2 *Determining the chemical potential in the experiment*

In the theoretical models the density profile is determined by the parameters μ and T in a harmonic confinement given by V_{ext} . Therefore, it seems evident to analyze the measured density profiles by fitting them to a theoretical model in which only μ and T are to be determined. However, this approach can be applied only if the size and the height of the measured profiles can be determined absolutely. Since the aforementioned PCI method is expected to do so, we can apply such a fit procedure here.

In the commonly used imaging methods the size or the height of the density profiles is not measured absolutely, and one has to fit the size and height of signal of both the BEC and the thermal cloud separately. In that case, μ and T are derived from the height and size of the measured density profiles. The experimental conditions favor the use of one of these measures above the others.

Being able to describe the complete cloud by μ and T , as is done in the theoretical models, is expected to yield a higher accuracy, since different measures for the chemical potential and temperature are combined which depend differently on experimental parameters such as the magnification, detuning and the trap frequencies. Furthermore, it allows for taking the interaction between the condensed and thermal atoms into account. This interaction is ignored in the vast majority of experiments in this field, in contrast to the theoretical description of a condensate at finite temperature found in many textbooks. Our PCI setup is expected to yield an accurate and absolute determination of both the density and the size of the cloud and measuring *in situ* prevents the need to account for the expansion of the cloud. Therefore, since all measures are absolute, μ and T are expected to fully describe the measured density profiles, given the fixed experimental parameters such as the magnification and the trap frequencies. This allows us to directly compare our measured density profiles to the three mean-field models described in the previous section.

The PCI method not only yields absolute density profiles, it is expected to yield a more accurate determination of the thermal fraction for low temperatures compared to absorption imaging as well. Since the accumulated phase for the dense BEC can be multiple times π , a significant phase is accumulated in the thermal cloud, without saturating the signal in the BEC. In absorption imaging on the other hand, the optical density of the thermal cloud is strongly reduced in order to reduce the optical density of the BEC to the order of 4. Especially for low temperatures, when only the low density tail of the thermal distribution spatially extends the BEC, it turns out to be difficult to distinguish between both components in the experiment. Various schemes have been used to enhance the contrast between the thermal cloud and the condensate, for example by making a two-pass fit routine, first only on the thermal cloud, followed by the condensate and thermal cloud while fixing the temperature found in the first

pass [56]. Another scheme used is spatial separation of both components using Bragg spectroscopy and fitting both parts separately [56]. In the PCI method the contrast between both components is sufficient for all measured temperatures and prevents the need to introduce elaborate schemes to enhance the contrast.

3.5 EXPERIMENTAL RESULTS

3.5.1 *Experimental parameters*

Imaging the atoms is conducted in such a way that the periodicity of the intensity of the PCI technique is used. Since the intensity signal varies periodically as a function of ϕ_{atoms} (Eq. (3.4)), the intensity signal shows rings in the intensity profile for sufficiently large values of ϕ_{atoms} (see Fig. 3.2). The number of rings depends on ϕ_{atoms} , which scales with the density and the detuning δ as can be seen from Eqs. (3.21) and 3.13. The detuning is a parameter which can be tuned accurately in a wide range (up to 400 MHz) using acoustic-optical modulators (AOMs) allowing us to make images with an adjustable number of rings. Due to the ring pattern the imaging lens can be put in position very sensitively allowing us to resolve features down to $4\ \mu\text{m}$. Furthermore, δ can be chosen in such a way that the intensity profile of the BEC shows rings and the less dense thermal cloud yields a significant intensity signal as well, even for low temperatures. The resulting effective dynamic range of this method is therefore increased by the periodic dependence of the intensity on the accumulated phase.

A drawback of this method lies in the fact that the BEC acts as a gradient index lens, the lensing being stronger for smaller δ . The effect of the lensing on the imaging resolution is estimated by a computer simulation in which the Fresnel-Kirchhoff diffraction integral is numerically integrated. In this simulation the finite size of the imaging lenses is explicitly taken into account. The mutual distances between the BEC, lenses, phase spot and image plane are chosen identical to the values used in the experiment. The intensity distribution at the image plane is used to estimate the effects of the refraction of the BEC on the imaging resolution. If the diffraction is too large, the higher diffraction orders can miss the aperture of the imaging lenses and will degrade the resolution of the image. This simulation yields an upper limit for the allowed phase shift of the BEC and therefore a lower limit of the applied detuning given the condensate density and dimensions. In the experiment we are in the regime in which the aperture of the lenses is not limiting the resolution, although the onset of a slight deformation of the density profile is observed for the highest condensate densities. For the typical parameters, the maximum focal length of the BEC is found to be of the order of $100\ \mu\text{m}$. Even though the diffraction is not too large for the apertures in the imaging path, the imaging lenses have to be placed in focus

within a few tens of micrometers to prevent distortions of the imaged intensity profile, since the imaged object itself acts like a lens.

The phase spot has to be aligned accurately as well, since all of the plane wave light has to propagate through the phase spot. In the long axis of the cloud the diffraction is weak, and for too large a phase spot the diffracted light propagates through the phase spot as well. In order to make a off between the two criteria that the phase spot should be large enough that the non-diffracted light is phase-shifted, but small enough that the diffracted light is not, the phase spot has a size of only a few times the waist of the probe beam. As a consequence, the phase spot is easily misaligned. Misalignment of the phase spot leads to reflection of the probe beam on the edges of the phase spot and possibly shifting the phase of the light, which is diffracted by the atoms. As a result of the misalignment we notice a higher, tilted intensity profile, which is easily detected, since we have several maxima in the intensity profile. The common way to apply PCI is by using a large detuning and the intensity signal never reaches the first maximum value. Without a well-defined maximum in the image, (slightly) more intensity due to misalignments may be unnoticed and the method can no longer be used to determine the absolute phase.

As can be seen in Fig. 3.2, the intensity as a function of the phase varies in certain ranges rapidly. Choosing a detuning in such a way that the maximum phase lies in this range, a slight increase in the density leading to a slight increase in the maximum phase leads to a large change in the intensity in the center of the cloud making the method very sensitive to small density changes.

In the experiment imaging the atoms consists of taking a sequence of three images. The first image obtains the intensity profile $I_{\text{atoms}}(x, z)$ of the probe field and the atoms. The second image contains the intensity profile $I_0(x, z)$ of the probe field in absence of the atoms. This image is generally shot after the magnetic trap has been turned off for two seconds and no atoms are left. The third image is the intensity profile $I_{\text{bg}}(x, z)$ with neither the probe field nor the atoms and is used as a background image. The normalized intensity profile $I(x, z)$ of the atoms is given by

$$I(x, z) = \frac{I_{\text{atoms}}(x, z) - I_{\text{bg}}(x, z)}{I_0(x, z) - I_{\text{bg}}(x, z)}, \quad (3.33)$$

where the subtraction and division is performed on a pixel-by-pixel basis. The magnification scheme used causes the probe beam to get blown up to such an extent that the beam profile is no longer smooth on the camera due to interference effects caused by dust and small scratches on the imaging optics. In principle, these imperfections are canceled in the final images, but since the imaging path is not interferometrically stable in between the acquisition of the three images, some distortions remain.

3.5.2 Phase contrast images

To demonstrate the PCI method, atoms are cooled below the critical temperature T_c in a $95.57 \text{ Hz} \times 95.57 \text{ Hz} \times 2.234 \text{ Hz}$ trap and imaged with a probe beam with an intensity $I_0 \simeq 6 \cdot 10^{-2} I_{\text{sat}}$ for $50 \mu\text{s}$. The probe beam is detuned 28.1γ below the $|F_g = 1\rangle \rightarrow |F_e = 1\rangle$ transition and results in typical intensity profile $I(x, z)$ as shown in Fig. 3.5. The high frequency noise found in these images is caused by the distorted profile of the probe beam. Small fringes close to the BEC are the result of the lenses being slightly out of focus.

3.5.3 Accurate determination of the number of condensed atoms

Accuracy using absorption imaging

The usual way to determine the number of condensed atoms is by taking a series of absorption images in time-of-flight. Absorption imaging turns out to become unreliable when the optical density exceeds 4 due to the limited dynamic range of the CCD camera [39]. If the cloud of atoms is a BEC, the typical optical density is in the order of 500 when the probe is on-resonance. Imaging the atoms off-resonance to take advantage of the reduced photon scattering cross section turns out to be complicated since the cloud behaves as a gradient-index lens in this regime. The optical density can be lowered by turning off the confinement causing the atoms to expand during a certain time-of-flight, until the density is low enough that the optical density is in the order of 4. However, expansion complicates the interpretation of the measured density profiles, since it consists of the convoluted momentum and spatial distribution of the atoms and the expansion of the cloud cannot be described exactly.

Furthermore, the switching of the magnetic confinement complicates the retrieval of the column density due to the finite time needed to switch the magnetic fields. In the absence of the magnetic field, the quantization axis of the atoms is no longer well defined causing the atoms to align along small residual magnetic fields during time-of-flight. This changes the effective cross section of the atoms for the applied polarized probe light. The magnitude and direction of the residual magnetic fields are expected to be spatially dependent. Since the atoms fall during time-of-flight due to gravity, the effective cross section is also expected to depend on the time-of-flight duration. Furthermore, the imaging lenses have to be repositioned for each time-of-flight duration. A final complication is that the accuracy of detuning of the probe light is limited to 1 MHz, corresponding to a reduction of the absorption up to 4%. All these effects cause uncertainties in the measured number of atoms up to 20%.

A technique is proposed based on the nonlinear response of atoms on the applied probe intensity in order to lower the optical density of the cloud without

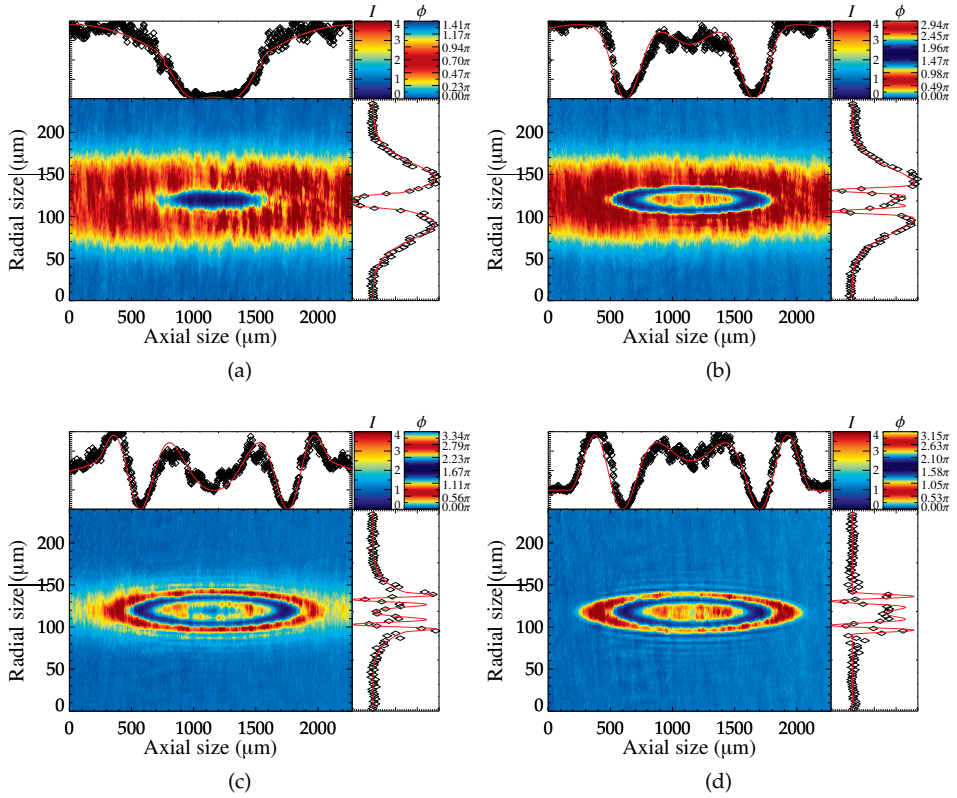


Figure 3.5: A set of four phase contrast images during the final stage of the evaporation process: (a) $\mu/h = 2.6 \text{ kHz}$, $T = 1.01 \mu\text{K}$, $N = 7 \cdot 10^8$ atoms, $N_c/N < 1\%$; (b) $\mu/h = 4.4 \text{ kHz}$, $T = 0.95 \mu\text{K}$, $N = 6 \cdot 10^8$ atoms, $N_c/N \approx 15\%$; (c) $\mu/h = 5.2 \text{ kHz}$, $T = 0.58 \mu\text{K}$, $N = 4 \cdot 10^8$ atoms, $N_c/N \approx 50\%$; (d) $\mu/h = 4.8 \text{ kHz}$, $T = 0.25 \mu\text{K}$, $N = 2 \cdot 10^8$ atoms, $N_c/N > 95\%$.

the use of expansion. This allows for quantitative *in situ* absorption imaging, although the precise calibration required has to be done after time-of-flight, reducing the accuracy of this method [40]. Moreover, the required reduction of the optical density of the condensate results in a reduction of the optical density of the thermal cloud as well, complicating the determination of both density profiles simultaneously. The high intensity needed to reach the strong saturation regime, $I \propto OD \times I_{\text{sat}} \approx 8 \text{ W/cm}^2$, with I_{sat} the saturation intensity, complicates the implementation of the method as well.

Accuracy using PCI

Using the PCI technique circumvents the issues raised above. The detuning is large compared to the uncertainty, $\delta = 281 \pm 1 \text{ MHz}$, and since the measurement is conducted *in situ* the confinement is not switched off and the quantization axis of the atoms remains well defined. The Zeeman shift caused by the confinement is less than 2 MHz and therefore negligible compared to the detuning.

An image of a BEC taken with PCI technique yields the accumulated phase and the size of the condensate. Analyzing all known systematic and statistical errors show that the largest contribution to the error in the size originates from the magnification of the imaging system. We determined the magnification to be $M = 3.05 \pm 0.05$. Since the condensate radius R is proportional to M , the number of condensed atoms scales as $N_c \propto M^5$ (see Eq. (3.28b) and Eq. (3.29)). The trap frequencies are derived from a center-of-mass oscillation measurements yielding the trap frequency with a statistical uncertainty below 10^{-3} .

The largest contribution to the error in the accumulated phase originates from the lensing effect of the condensate and is estimated to be less than 5% in the measured phase based on the computer simulation we conducted. This effect does not influence the axial size of the cloud since the density varies slowly in this direction making the lensing negligible. Since the number of atoms scales with the accumulated phase as $N \propto \phi^{5/3}$, lensing is expected to yield an error up to 8% in the number of atoms for the highest densities.

We analyze measured clouds for similar parameters as the ones shown in Fig. 3.5, where the condensate fraction is at least 90% by making a least square fit to the ideal model. We conclude both the determined size and phase of the condensate yield the same chemical potential μ within 3% for the typical number of condensed atoms $N_c \sim 2.5 \cdot 10^8$. Since the thermal fraction is small, interactions are expected to be of minor importance in this regime.

We expect that the small discrepancy between the measures for μ is caused by the lensing effect of the condensate, which slightly alters the density profile. If the imaging lens is aligned incorrectly, more lensing is observed and the discrepancy between the chemical potential based on the phase and sizes increases.

3.5.4 Observation of interactions between the thermal cloud and the BEC

The effect of interactions between the thermal cloud and the BEC becomes important if a significant thermal fraction is present. As pointed out in Ref. [57], the thermodynamic behavior of the cloud is fixed by two parameters: the reduced temperature $t = T/T_c^0$ and the ratio η given by

$$\eta = \frac{\mu_0^{\text{TF}}}{k_B T_c^0} \approx 1.57 \left(N^{1/6} \frac{a}{\bar{a}} \right)^{2/5}. \quad (3.34)$$

Here $T_c^0 = \hbar\bar{\omega}(N/\zeta(3))^{1/3}$ denotes the transition temperature in the absence of interactions and $\bar{a} = \sqrt{\hbar/(m\bar{\omega})}$ is the harmonic oscillator length.

Under our typical conditions $\eta = 0.3$, which is less than its value in other experiments studying the interactions [56, 58]. There it is shown that interactions between the atoms shift the transition temperature T_c downward. Ref. [56] measured the effects of the interactions by spatially separating the thermal cloud from the BEC using Bragg spectroscopy to avoid the need to incorporate interactions in the description of the measured density profiles. The separation of both clouds depends sensitively on the applied Bragg pulse, and introduces an extra uncertainty. Furthermore, the accuracy is limited by the absence of an exact theory describing the expansion of the BEC.

Using PCI these interaction can be measured directly and more accurately than in these previous studies, although η is smaller. The measurements are conducted as follows. Using evaporative cooling we obtain a cold cloud of atoms at a temperature T below T_c under the same experimental conditions as the measurement shown in Fig. 3.5. A phase contrast image of this elongated cloud is taken with each cloud cooled to different temperatures. Each image is fitted to all three 2D models described in § 3.4.1 and yield a temperature and chemical potential. We find the best fit can be made, determined by the smallest sum-of-squares, using the Popov model and the semi-ideal model. The noninteracting model gives inferior results and cannot be used to accurately describe the measured profiles. This has already been noticed in previous work [56, 58].

In this experiment we can also see the effect of the mean-field potential of the thermal cloud on the condensed atoms although less prominent than the modification of the thermal distribution. This effect is already hinted at in Ref. [56]. The density distribution of the thermal cloud causes an effectively larger potential for the condensed atoms. The effect of the resulting distribution is analogous to increasing the trap frequency: the cloud gets smaller and denser. Since we can measure both density and size separate and with a high accuracy, we measure the effect of the interactions by comparing the chemical potential based on the axial size and the accumulated phase. The axial size is favored above

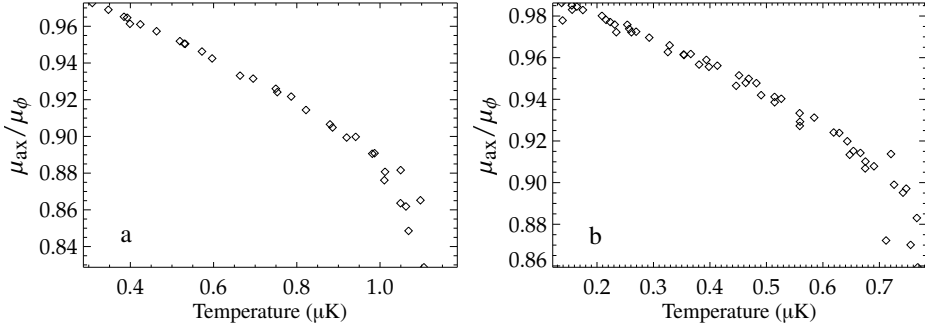


Figure 3.6: The ratio $\mu_{\text{ax}}/\mu_{\phi}$ of the chemical potential based on the axial size R_{ax} and phase ϕ as function of the temperature. Figure a corresponds to $\eta = 0.3$ and Fig. b corresponds to $\eta = 0.25$. In the second series η is reduced by reducing the number of atoms.

the radial size for two reasons: lensing effects in this direction are negligible and the size is large compared to the resolution of the imaging setup.

From the fit results we determine the axial size and phase of the condensed part of the cloud and calculate its chemical potential based only on the accumulated phase, yielding μ_{ϕ} or the axial size, yielding μ_{ax} . The ratio $\mu_{\text{ax}}/\mu_{\phi}$ is plotted against the temperature T and shown in Fig. 3.6. We find the chemical potential based on the axial size for temperatures close to T_c to be approximately 15% too small compared to the chemical potential based on the accumulated phase. As the temperature decreases, this effect gets smaller until at low temperatures (low thermal densities) we find correspondence between both measures within a few percent, consistent with the results found in the previous section. Since our standard fitting procedure uses μ and T to fully describe the density profile, we find the sum-of-squares to be 10% smaller at temperatures where a significant thermal fraction is present (condensate fractions up to 80%) for the fit using the Popov model compared to a fit using the semi-ideal model.

Since this shows that the Popov model yields the most consistent results all measurements in the remainder of this chapter are analyzed using the Popov model.

3.5.5 Accuracy and reproducibility

Repeated measurements are done in the regime where three-body losses limit the density of condensed atoms. The total number of condensed atoms N_c is therefore approximately constant and the results are used to determine the sensitivity as

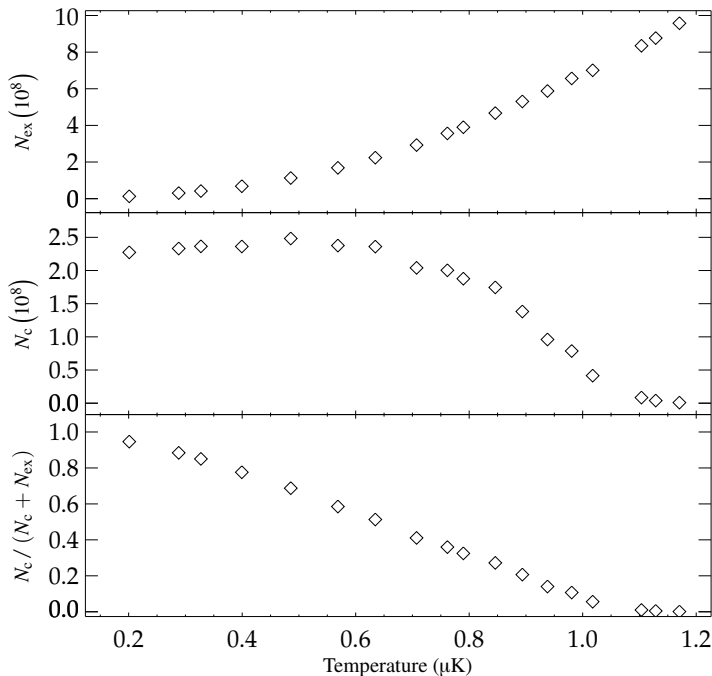


Figure 3.7: The number of thermal atoms N_{ex} , condensed atoms N_c and the condensate fraction as a function of the temperature T . Each point is the result of a fit to the Popov model on a single measurement. The statistical uncertainty is smaller than the size of the symbol.

well as the reproducibility of the PCI method. The measurement series takes over two hours and during this time the temperature of the cloud changes from $T = 0.573 \pm 0.004 \mu\text{K}$ to $T = 0.387 \pm 0.004 \mu\text{K}$ due to the apparatus heating up. However, in the density limited regime the number condensed atoms is roughly constant in this temperature range. The measured number of condensed atoms is found to change less than 3% during the two measurement time on a cloud containing $N_c = (250 \pm 10) \cdot 10^8$ condensed atoms. For measurements shot back-to-back the number of condensed atoms changes approximately 1%. Since we assume the largest contribution is caused by the difference in the environmental conditions, this result sets the upper limit of 1% for the shot-to-shot reproducibility of the PCI method using the two parameter fit.

Our fit procedure, in which μ and T are determined by both phase and size simultaneously using the Popov model, yields statistical errors below one percent, smaller than the estimated systematic error. The uncertainty in the number of condensed atoms, which scales as $N_c \sim \mu^{5/2}$, is therefore estimated from the

discrepancy between μ_{ax} and μ_{ϕ} , which is roughly 3% and yields an uncertainty in the number of condensed atoms of 5%.

In an experiment we set up to determine the accuracy of the method on a single shot for various temperatures, we produce clouds at various temperatures below T_c . The resulting number of thermal and condensed atoms, as well as the condensate fraction determined on the fitted μ and T is shown in Fig. 3.7, where each point corresponds to a single measurement. The fluctuations in these results are only a few percent for both the number of thermal and condensed atoms and this measurement shows the accuracy of the PCI method over the full temperature range.

3.5.6 Transition temperature for condensation

Generating clouds above as well as below the transition temperature allows us to determine the temperature at which condensation sets in. The Popov model yields μ and T in both regions, where μ becomes negative for temperatures above T_c^0 . Note that our implementation of the Popov model reduces to the Hartree-Fock model for $T > T_c$ [54].

For $T - T_c^0 \ll T_c^0$ the chemical potential as a function of temperature for a noninteracting Bose gas can be written as [54]

$$\mu \approx 3 \frac{\zeta(3)}{\zeta(2)} k_B (T - T_c^0), \quad (3.35)$$

where ζ is the Riemann-Zeta function. Equation (3.35) can be used to estimate T_c^0 . Note that the repulsive interactions lower the central density and therefore reduce the transition temperature. Therefore, condensation does not set in at T_c^0 , where $\mu = 0$, but for $\mu = 2U_0 n_{\text{ex}}$.

In the experiment we generate clouds at different temperatures above as well as below the transition temperatures and derive T and μ from a fit to the Popov model. The results presented in Fig. 3.8 show positive values of μ for all temperatures, although no BEC is observed in the five points with the highest temperatures. The seven data points with the highest temperature are used to make a fit to Eq. (3.35) with T_c^0 being the only free parameter. This yields $T_c^0 = 0.998 \pm 0.007 \mu\text{K}$. The thermal density is determined by averaging the two measurements which are the closest to the temperature where a condensate is formed. Both n_{ex} and T_c^0 are used to find the temperature in Eq. (3.35), where $\mu = 2U_0 n_{\text{ex}} = h(1.65 \pm 0.05 \text{ kHz})$. This yields $T_c = 0.972 \pm 0.008 \mu\text{K}$.

The measured shift due to the interactions is $(T_c^0 - T_c)/T_c = 0.027 \pm 0.001$, which agrees well with the theoretical prediction based on the Hartree-Fock mean-field theory, $\Delta T_c/T_c \approx -1.33a/\bar{a}N^{1/6} \approx 0.025$ [54].

In order to confirm the systematic errors are well estimated, we compare the value of T_c to the highest temperature where we observe a bimodal distribution

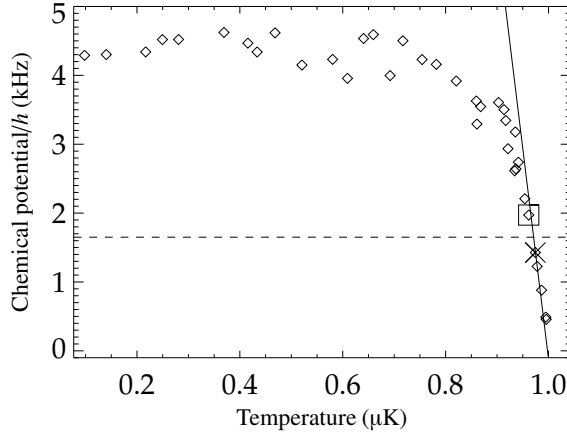


Figure 3.8: The chemical potential of a cold cloud derived from the fit to the Popov-model as a function of temperature, both above and below T_c . The line is the result of a fit to Eq. (3.35) on the seven data points where $\mu/h < 2.5$ kHz. The data point accentuated by the box marks the observation of a small BEC. The point accentuated by the cross is the point with the lowest temperature, in which no bimodal distribution is observed. The dashed line indicates $\mu = 2U_0n_{ex}$, calculated using the average thermal density of the two accentuated points.

in the image, both by fitting the cloud and by examining line profiles through the center of the cloud. The highest temperature where a BEC is observed is determined at $T = 0.963 \pm 0.005 \mu\text{K}$, where the lowest temperature without a BEC yields $T = 0.975 \pm 0.003 \mu\text{K}$ and the determined value of T_c indeed lies in between these two temperatures. The consistency of these numbers suggest the systematic errors are well estimated.

3.6 CONCLUSION

In conclusion, this chapter describes the accurate determination of the density distribution of condensates at finite temperatures using PCI. A detailed description is given of the amount of phase a probe beam accumulates when a cloud of atoms is passed. The resulting images show a periodic variation of the intensity as a function of the accumulated phase and the resulting high dynamic range is used to measure both the density distribution of a thermal cloud and a condensate simultaneously at high accuracy. Since all measurements are done *in situ*, there is no need to describe the expansion of the cloud. The size of the condensate, also a measure for its density, can therefore be determined accurately as well. The size of the thermal cloud, the measure for the temperature of the cloud, is also

determined from the same image. Only two relevant parameters, μ and T , are needed to describe the measured clouds given the harmonic confinement as μ and T determine both the peak density and size of both components of the cloud. This procedure is used to discriminate between three models describing the equilibrium properties of trapped clouds at nonzero temperatures, each model incorporating the interactions between thermal atoms and condensed atoms differently.

We resolve the effect of the interaction on the density distribution of thermal cloud as well as the smaller effect the interaction has on the density distribution of the condensate. The model accounting for these effects gives consistent results over the complete temperature range. The imaging scheme is used to determine the number of atoms within one percent from shot-to-shot at our typical number of condensed atoms between $2 \cdot 10^8$ and $3 \cdot 10^8$. Systematic errors are estimated by comparing the different measures for the chemical potential and we find the uncertainty in the number of number of condensed atoms to be roughly five percent. PCI can be used both below and above the transition temperature and we used it to determine T_c and derived the shift of the transition temperature due to the interactions. The agreement with the theoretical value of this shift indicates the systematic errors are smaller than the uncertainty in the determination of T .

A COLLECTIVE EXCITATION: THE QUADRUPOLE MODE

Abstract

We study the quadrupole mode of a cloud of atoms. The crossover from the collisionless toward the hydrodynamic regime is observed for temperatures above T_c . We find the frequency and damping rate of this mode to agree well with both previous work and a theoretical description. From this measurement we conclude that the thermal cloud is already highly hydrodynamic above T_c . The cloud becomes even more hydrodynamic when it is cooled to temperatures below the transition temperature and the BEC forms. We have measured the frequency and damping rate of both the thermal cloud and condensate at various temperatures. For strong excitation of the cloud a periodic density modulation is observed in the BEC. We find the wavelength of this modulation to be constant for different axial confinements.

4.1 INTRODUCTION

In the previous chapter the static properties of Bose-Einstein condensates at finite temperatures are studied. The dynamics of the condensate and thermal cloud are the subject of the following chapters. In this chapter the time-dependent behavior of a cold cloud is studied, both above and below the transition temperature, after it has been subjected to a variation of the trapping potential. This excitation results in a collective oscillation of the atoms: the quadrupole oscillation.

The study of collective excitations is some of the first experiments conducted after the experimental realization of Bose-Einstein condensation in dilute gases in 1995 [1, 2]. Pioneering experiments by the JILA group [10, 59] and the MIT group [11] studied low-lying excitations below T_c in the collisionless regime. The mean free path of the thermal atoms is much larger than the size of the cloud in the collisionless regime, thus collisions between thermal atoms do not dominate the time-dependent behavior. The results at low temperatures have been found to be in good agreement with zero temperature calculations [60, 61]. Above the transition temperature, calculations of the frequency [62] and damping rate [63] of the quadrupole oscillation in a thermal cloud shows that these experiments are consistent with collisionless behavior. In the following years, the MIT group

managed to increase the density and reached the hydrodynamic regime, in which the mean free path of the thermal atoms is smaller than one of the sizes of the cloud. They studied several collective excitations above and below T_c , including the quadrupole oscillation [13]. However, the measured frequencies above T_c indicate the cloud is not deep in the hydrodynamic regime.

The hydrodynamic regime is deeply entered above T_c in experiments conducted by the ENS group [64] and the AMOLF group [14]. Their data shows good agreement with calculations of the frequency and damping rate both in the collisionless regime, the hydrodynamic regime, as well as the crossover between both regimes [65]. However, both groups have not extended their work to temperatures below the transition temperature.

There are two regimes in which the measurements of the quadrupole oscillation frequency shows good agreement with the available theoretical descriptions. Above T_c , where no condensate exists and below T_c at sufficient low temperatures that the thermal fraction becomes negligible. However, the situation is less satisfactory at finite temperature where a description of the coupled dynamics of condensed and fluid-like thermal atoms is required. Several finite-temperature models exist describing these coupled dynamics, where only the ZGN theory incorporates the two-fluid regime [66, 67].

First, a short summary of a mean-field theory is given that accounts for the measured frequencies of the collective excitations both above T_c and at $T = 0$. A detailed description of this procedure can be found in Refs. [54, 61, 62, 68].

4.2 THEORETICAL DESCRIPTION OF THE QUADRUPOLE MODE

Dynamics of a Bose-Einstein condensate at zero temperature can be described by the time-dependent Gross-Pitaevskii equation (GPE)

$$i\hbar\Psi(\mathbf{r}, t) = \left[-\frac{\hbar^2}{2m}\nabla^2 + V_{\text{ext}}(\mathbf{r}) + U_0|\Psi(\mathbf{r}, t)|^2 - \mu \right] \Psi(\mathbf{r}, t), \quad (4.1)$$

where Ψ is the wave function of the condensate, m is the mass, V_{ext} is the external trapping potential, U_0 is the interaction parameter and μ is the chemical potential. Eq. (4.1) can be reformulated as a pair of hydrodynamic equations which can be used to determine the excitation spectrum of the condensate [54]. Here, we follow the approach described by Pethick & Smith [54] to determine the frequency of the quadrupole oscillation.

By writing $\Psi = f e^{i\phi}$, with the density $n = |f|^2$ and the velocity $\mathbf{v} = \frac{\hbar}{m}\nabla\phi$, the equations of motion can be found by inserting Ψ into Eq. (4.1)

$$\dot{n} + \nabla \cdot (n\mathbf{v}) = 0, \quad (4.2)$$

which is the continuity equation for the particle density n and

$$m\dot{\mathbf{v}}(\mathbf{r}, t) = -\nabla \left(\tilde{\mu}(\mathbf{r}, t) + \frac{1}{2}m|\mathbf{v}(\mathbf{r}, t)|^2 \right), \quad (4.3)$$

where

$$\tilde{\mu}(\mathbf{r}, t) = V_{\text{ext}} + U_0 n(\mathbf{r}, t) - \frac{\hbar^2 \nabla^2 \sqrt{n(\mathbf{r}, t)}}{2m \sqrt{n(\mathbf{r}, t)}}. \quad (4.4)$$

Equation (4.3) is the analog of the Euler equation. These two equations are the quantum analog of the hydrodynamic equations and are used to describe the collective motion of the cloud [54].

The hydrodynamic equations Eq. (4.2) and Eq. (4.3) are solved by considering the approximate linearized equations by writing $n(\mathbf{r}, t) = n_0(\mathbf{r}) + \delta n(\mathbf{r}, t)$, $\mathbf{v}(\mathbf{r}, t) = \delta \mathbf{v}(\mathbf{r}, t)$ and $\tilde{\mu} = \tilde{\mu}_0 + \delta \tilde{\mu}$. After taking the time derivative of Eq. (4.2) and eliminating the velocity by means of Eq. (4.3) the equation of motion is found, resulting in

$$m\ddot{n} = -\nabla \cdot (n_0 \nabla \delta \tilde{\mu}). \quad (4.5)$$

If the number of atoms is sufficiently large the quantum pressure term (last term in Eq. (4.4)) can be neglected, $\delta \tilde{\mu} = U_0 \delta n$. To find time dependent, oscillating solutions, the Ansatz $\delta n \propto \delta n e^{-i\omega t}$ is inserted in Eq. (4.5) resulting in

$$\omega^2 \delta n = \frac{1}{m} \left\{ \nabla V_{\text{ext}}(\mathbf{r}) \cdot \nabla \delta n - (\mu - V_{\text{ext}}(\mathbf{r})) \nabla^2 \delta n \right\}, \quad (4.6)$$

where the equilibrium density $n(\mathbf{r}) = (\mu - V_{\text{ext}}(\mathbf{r})) / U_0$ in the TF-approximation is used. The eigen frequencies of this equation of motion strongly depend on the confining potential, as can be seen from Eq. (4.6).

The experiments are conducted in a harmonic anisotropic trap with the z -axis the axis of symmetry. The potential is written in the form

$$V_{\text{ext}}(x, y, z) = \frac{1}{2}m \left(\omega_{\text{rad}}^2 x^2 + \omega_{\text{rad}}^2 y^2 + \omega_{\text{ax}}^2 z^2 \right) = \frac{1}{2}m\omega_{\text{rad}}^2 \left(\rho^2 + \lambda^2 z^2 \right), \quad (4.7)$$

where the anisotropy parameter $\lambda = \omega_{\text{ax}} / \omega_{\text{rad}}$, the subscripts rad and ax denote the radial and axial direction, respectively and $\rho^2 = x^2 + y^2$.

We excite a collective excitation by abruptly increasing the axial trap frequency. Due to the repulsive interactions, compression in the axial directions results in decompression in the radial direction. The mode that is predominantly excited is a mode in which the axial width of the cloud oscillates out-of-phase with respect to the radial width. We refer to this mode as the quadrupole mode. A schematic representation of the motion of the cloud is given in Fig. 4.1. The frequency of the quadrupole oscillation is calculated by searching solutions of Eq. (4.6) of the form

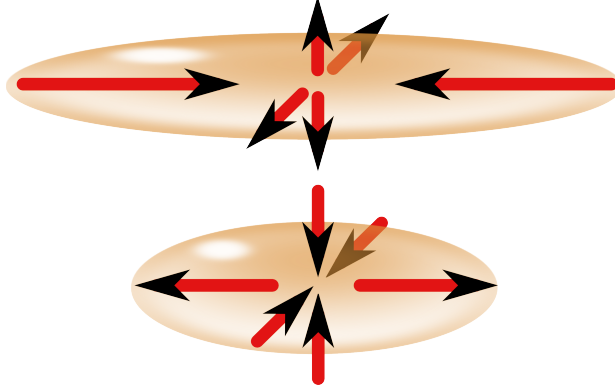


Figure 4.1: A schematic representation of the quadrupole mode. The arrows indicate the velocity of the atoms and show the out-of-phase oscillation of the axial and radial size of the cloud.

$\delta n = 1 + \alpha\rho^2 - \beta z^2$, independent of the azimuth angle ϕ , where the coordinates are expressed in terms of cylindrical coordinates (ρ, ϕ, z) . The eigen frequency of this mode is found to be

$$\omega_{\text{q}}^2 = \omega_{\text{rad}}^2 \left(2 + \frac{3}{2}\lambda^2 - \frac{1}{2}\sqrt{16 - 16\lambda^2 + 9\lambda^4} \right), \quad (4.8)$$

a result first derived by Stringari *et al.* [61]. In the limit of $\lambda \rightarrow 0$ Eq. (4.8) reduces to

$$\omega_{\text{q}} = \sqrt{\frac{5}{2}}\omega_{\text{ax}}. \quad (4.9)$$

The quadrupole mode described above also exists above the transition temperature. In the case of a Bose-Einstein condensate, the motion is expressed in terms of the local density and velocity, since the only degrees of freedom are those of the condensate wave function. For a Bose gas above T_c there are many degrees of freedom and a microscopic description has to be employed. However, if the number of collisions is sufficiently large to achieve a local thermodynamic equilibrium, a description in terms of local particle density, temperature and velocity can be made using the hydrodynamic equations. In this limit the equation of motion and resulting eigen equation can be derived in a similar way as in the case of a BEC [62]. The resulting expression of the quadrupole mode eigen frequency is first derived in Ref. [62] and given by

$$\omega_{\text{q}}^2 = \frac{\omega_{\text{rad}}^2}{3} \left(5 + 4\lambda^2 - \sqrt{25 - 32\lambda^2 + 16\lambda^4} \right). \quad (4.10)$$

In the limit of $\lambda \rightarrow 0$ Eq. (4.10) reduces to

$$\omega_q = \sqrt{\frac{12}{5}} \omega_{ax}. \quad (4.11)$$

The calculated eigen frequency of this mode is only valid in the hydrodynamic limit. In the absence of collisions a compression of the cloud will only exhibit an oscillation due to the harmonic confinement, although this motion is better to refer to as a coherent motion than a collective shape oscillation. The frequency of this motion is $2\omega_{ax}$, since the cloud will reach its smallest axial size a quarter of a trap period after the initial excitation and after half a trap period the cloud reaches its original axial size again. In the collisionless regime the damping is proportional to the collision rate. The damping rate will increase for increasing number of collisions until the hydrodynamic regime is entered and the damping rate decreases again [65].

We introduce a measure for the hydrodynamicity in the axial direction $\bar{\gamma} \equiv \gamma_{col}/\omega_{ax}$, where the collision rate $\gamma_{col} = n_{eff} \sigma v_{rel}$ is the average number of collisions. Here, the relative velocity $v_{rel} = \sqrt{2} \bar{v}_{th}$, where $\bar{v}_{th} = \sqrt{8k_B T/m\pi}$ is the average thermal velocity at temperature T with m the mass and k_B the Boltzmann constant. Furthermore, $n_{eff} = \int n^2(\mathbf{r}) dV / \int n(\mathbf{r}) dV = n_0/\sqrt{8}$ for an equilibrium distribution in a harmonic potential, where n_0 is the peak density. Written in terms of the number of atoms $N = n_0 2\pi k_B T / \sqrt[3]{m\bar{\omega}^2}$ and the geometric mean of the angular trap frequencies $\bar{\omega}^3 \equiv \omega_{rad}^2 \omega_{ax}$, this results in $\gamma_{col} = Nm\sigma\bar{\omega}^3/(2\pi^2 k_B T)$.

4.3 EXPERIMENTAL OBSERVATION OF THE QUADRUPOLE MODE ABOVE T_C

First the measurements above T_C are presented. We compare our results to the work of Buggle and coworkers [14], where the crossover from the collisionless to the hydrodynamic regime is observed and found to be in good agreement to the theoretical model of this crossover derived by Guéry-Odelin and coworkers [65]. In a second experiment the temperature is decreased and a condensate forms. The quadrupole oscillation is then studied as a function of the temperature and condensate fraction, as described in the next section. In order to enter the hydrodynamic regime as deep as possible we evaporatively cool the atoms in a trap which is weak along one direction (axial) and strong along the other directions (radial) to suppress avalanche enhanced losses [36]. This procedure cuts both ways; the number of atoms (collision rate) stays high, while the trap frequency is lowered, both enlarging $\bar{\gamma}$. The final confinement is highly asymmetric, $\lambda \approx 1/85$, resulting in cigar-shaped clouds. Typical experimental conditions allow us to cool up to $1.3 \cdot 10^9$ atoms in a clover leaf type Magnetic Trap (MT) characterized by the radial trap frequencies $\omega_{rad}/(2\pi) = 95.6$ Hz and the axial trap frequency

$\omega_{\text{ax}}/(2\pi) = 1.10 \text{ Hz}$ at a temperature of approximately $T = 1.2 \mu\text{K}$, equivalent to $T \approx 1.2T_{\text{c}}$.

These experimental parameters yield a hydrodynamicity of $\bar{\gamma} \lesssim 10$ in the axial direction. In the radial direction, this parameter is $\bar{\gamma}_{\text{rad}} \approx 0.2$. Since the hydrodynamic regime is only entered in the axial direction, $\bar{\gamma}$ will implicitly refer to the hydrodynamicity in the axial direction. Even at the highest hydrodynamicity the lifetime of the cloud, limited by three-body decay, is more than 60 s, which is more than sufficient for the experiments described below. By decreasing the number of atoms, the crossover from the hydrodynamic to the collisionless regime is studied.

We excite the shape oscillation by diabatically changing the axial trapping potential, which causes an axial compression of the cloud. We typically ramp up the axial confinement to $\omega_{\text{ax}}/(2\pi) = 1.3 \text{ Hz}$ in 20 ms and ramp it back down in 20 ms to the original value $\omega_{\text{ax}}/(2\pi) = 1.10 \text{ Hz}$. Once the cloud is excited, it is allowed to oscillate in the original trap geometry for a hold time τ . Next, the confinement is turned off and an absorption image is recorded on the CCD camera after the cloud has expanded during a certain time-of-flight. In order to prevent nonlinear excitation, we only make small excitations. Typically, the oscillations have a relative oscillation amplitude up to 10%. Under these conditions, the oscillation amplitude is expected to have an effect on oscillation frequency and damping rate of less than 0.5% [69]. Inadvertently, a small center-of-mass motion is induced by the change of the axial confinement, probably caused by a slight misalignments of the coils which produce the confinement. In these experiments this is advantageous, since this motion does not couple to the quadrupole motion and it can be measured separately. The center-of-mass oscillation can therefore be used to measure the axial trap frequency in every measurement series.

The imaged clouds are analyzed using a least square fit to a 2D Gaussian distribution. This fit yields the optical density, the axial and radial width and the axial and radial position. The total absorption is used as a measure for the number of atoms, the widths are used to determine the aspect ratio and the temperature and finally the axial position is used to measure the center-of-mass oscillation.

A series of measurements consists of about 50 sequential shots at various hold times τ , from which the aspect ratio is determined. We plot the aspect ratio as a function of τ in Fig. 4.2 and it shows a damped oscillation of the aspect ratio. Fitting the aspect ratio as a function of τ to a damped sinusoidal function yields both an oscillation frequency ω_{q} and a damping rate Γ_{q} . Furthermore, the center-of-mass motion is fitted to an undamped sinusoid and yields the axial trap frequency ω_{ax} . The number of atoms and temperature is determined from an average over all shots, taking the oscillating width into account and yields the hydrodynamicity $\bar{\gamma}$. We measure ω_{q} and Γ_{q} for various values of $\bar{\gamma}$ by changing the number of atoms.

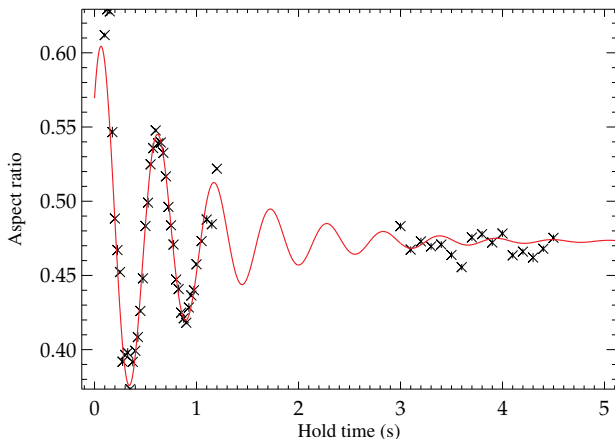


Figure 4.2: The aspect ratio of a thermal cloud in the hydrodynamic regime with $\bar{\gamma} \approx 8$ as a function of the hold time τ , showing the quadrupole oscillation of the thermal cloud. Absorption imaging is used to image the atoms after the cloud is allowed to expand during time-of-flight for 60 ms. The solid line is the result of a fit of the data to a damped sinusoid. Due to the destructive imaging used each point represents the aspect ratio of a newly prepared cloud.

The measured normalized quadrupole oscillation frequency ω_q/ω_{ax} and normalized damping rate Γ_q/ω_{ax} as a function of the hydrodynamicity are shown in Fig. 4.3. The measured frequencies for small values of $\bar{\gamma}$ is $\omega_q/\omega_{ax} \approx 2.01 \pm 0.02$ and almost undamped, as expected. For the highest values of $\bar{\gamma}$ we find $\omega_q/\omega_{ax} \approx 1.59 \pm 0.03$, close to theoretical value given by Eq. (4.11). Furthermore, the normalized frequency and damping rate shows good agreement with the theoretical values given in Ref. [65] and the experimental results of Ref. [14]. However, the theoretical damping rates appear to be slightly lower compared to the measured values. We have measured the center-of-mass oscillation of the thermal cloud for different oscillation amplitudes and find an undamped motion with no significant dependence of the oscillation frequency on the amplitude. As a consequence, we exclude anharmonicities of the trapping potential as a source of apparent damping. The trap frequency, determined in each series, is confirmed to remain constant over all series within the accuracy of the measurement.

Results presented in Ref. [70] show that a Bose gas is slightly more hydrodynamic than a classical gas close to T_c . The three measurements at the most hydrodynamic conditions have been measured at $T \approx 1.2T_c$, where we expect the cloud to be even slightly more hydrodynamic than our calculation based on the number of atoms and temperature due to Bose enhancement.

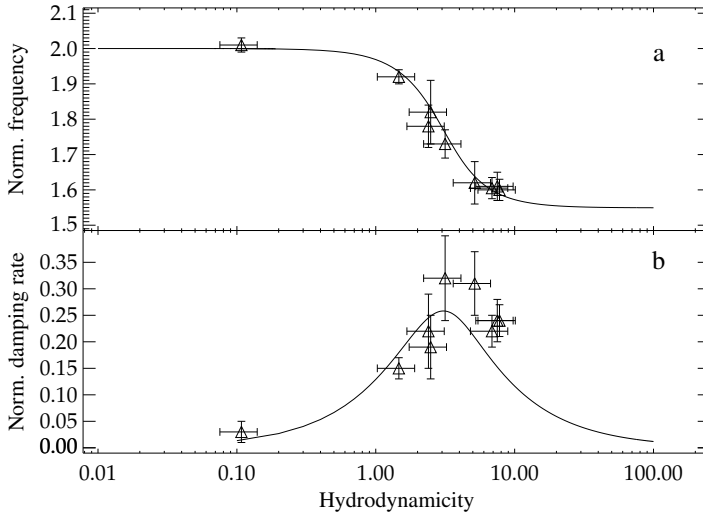


Figure 4.3: The normalized frequency ω_q/ω_{ax} (Fig. a) and normalized damping rate Γ_q/ω_{ax} (Fig. b) as a function of the hydrodynamicity parameter $\bar{\gamma}$. The solid lines are the result of the theoretical description of the frequency and damping rate given in Ref. [65].

In conclusion of the measurements above T_c , we have measured the crossover from the collisionless to the hydrodynamic regime and find the measured frequency and damping rate of the quadrupole motion in agreement with previous work.

4.4 EXPERIMENTAL OBSERVATION OF THE QUADRUPOLE MODE BELOW T_c

For the measurements described in this section the experimental settings are used that yield the highest hydrodynamicity. The cloud is subsequently cooled to temperatures below the transition temperature T_c , where a thermal cloud and a BEC co-exist. In Ref. [71] it is noted that if one is already close to the hydrodynamic domain above T_c , one will be deeply in the hydrodynamic region when the Bose-Einstein condensate forms. The mechanism behind this enhanced hydrodynamicity lies in the relevant collisions, which are the collisions between condensed atoms and thermal atoms instead of collisions between thermal atoms. Due to the higher density of the condensed atoms, even just below T_c , the effective collision rate of the cloud increases. Thus, we expect to be in the fully hydrodynamic regime in the axial direction for $T \leq T_c$. At temperatures below the transition temperature we are able to measure the column density distribution of the cloud using *in situ* phase contrast imaging, as well as absorption imaging

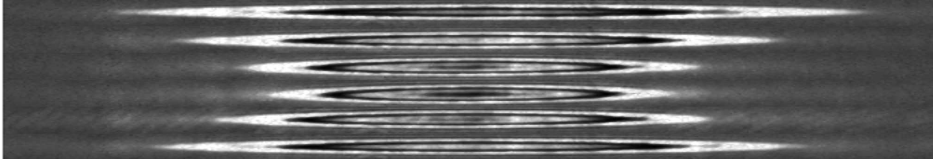


Figure 4.4: A series of six *in situ* phase contrast images of a BEC and thermal cloud during a quadrupole oscillation. The difference in hold time between these images is a ninth of a trap period. For clearness this oscillation is excited stronger, resulting in a higher oscillation amplitude than used in the other measurements presented in this chapter.

after time-of-flight. A series of *in situ* phase contrast images of the cloud during a quadrupole oscillation is shown in Fig. 4.4, illustrating the typical motion of the trapped cloud. For technical reasons, absorption imaging is used in the other experiments presented in this chapter.

The absorption images are analyzed using a least square fit to a 2D bimodal distribution: the sum of a Thomas-Fermi shaped density profile to model the condensate and a Maxwell-Bose distribution to model the thermal cloud [39]. The thermal cloud can easily be distinguished from the condensate due to the difference in the density distribution. The fit yields the optical density and the axial and radial width. A center-of-mass oscillation is excited below T_c , as is the case above T_c . The axial position of the cloud is determined and used to analyze the center-of-mass oscillation, from which the axial trap frequency is derived. Clouds are prepared at different temperatures by varying the final frequency of the rf-field. The temperature is set in the range from $T \approx T_c$ to the lowest temperature reachable with evaporative cooling, $k_B T \approx \mu$.

A series of measurements consists of about 50 sequential shots at a certain temperature for various hold times τ , from which the aspect ratio of both the thermal cloud and the condensate is determined. Fig. 4.5 shows the aspect ratio of the thermal cloud and the condensate as a function of τ . The change in aspect ratio of both components is subsequently fitted to a damped sinusoid, which yields the oscillation frequency $\omega_{q, \text{bec}}$ ($\omega_{q, \text{ex}}$) and a damping rate $\Gamma_{q, \text{bec}}$ ($\Gamma_{q, \text{ex}}$) of the quadrupole mode for the condensate (thermal cloud). In each series the axial trap frequency is determined by fitting the axial center-of-mass oscillation, which is found to be undamped within the accuracy of the measurement. We have measured the quadrupole oscillation for five different temperatures and tabulated the normalized measured frequencies and damping rates of both components in Table 4.1.

As above T_c , we find the measured quadrupole frequency of the thermal fraction to agree well with the expected value in the hydrodynamic limit; at

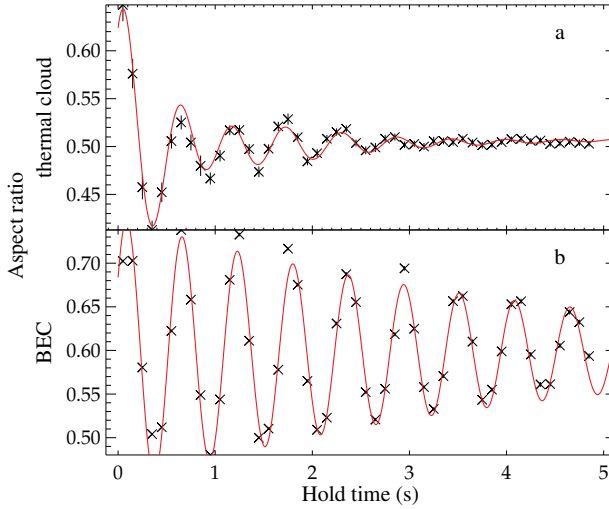


Figure 4.5: The aspect ratio of the thermal cloud (Fig. a) and condensate (Fig. b) as a function of the hold time. The clouds are imaged using absorption imaging after the cloud is allowed to expand during time-of-flight for 80 ms. The solid line in both figures is the result of a fit to a damped sinusoid.

$T/T_c = 0.66$ we measure $\omega_{q,ex}/\omega_{ax} = 1.54(3)$ compared to the predicted value of 1.549 of Eq. (4.11). The damping rate of the quadrupole oscillation in the thermal cloud is smaller than the measured damping rate above T_c . This confirms that the hydrodynamicity is increased, although the number of collisions between thermal atoms has decreased due to the lower thermal density. This result substantiates the claim in Ref. [71] that the thermal cloud behaves more hydrodynamic due to collisions with condensed atoms.

The frequency of the quadrupole oscillation of the condensate at the lowest temperature measured ($T/T_c \approx 0.2$) is $\omega_{q,bec}/\omega_{ax} = 1.577(9)$, in excellent agreement with the value $\omega_q/\omega_{ax} \approx 1.581$ given by Eq. (4.9). At higher temperatures this frequency shows a small but significant shift.

The quadrupole oscillation of the BEC damps slowly; at the lowest temperature no significant damping is observed within 5 oscillation periods. The reduced lifetime caused by three-body losses, about 60 s, complicates measuring more periods on an almost pure condensate. Although the number of condensed atoms is only slightly reduced within 5 oscillation periods, these losses cause the temperature of the cloud to increase substantially. At higher temperature the damping rate increases and at these temperatures a significant damping is observed within a few oscillation periods, allowing for a more accurate determination of the damping rate compared to lower temperatures. We attribute the

T/T_c	$N_c/(N_c + N_{ex})$	$\omega_{q,ex}/\omega_{ax}$	$\Gamma_{q,ex}/\omega_{ax}$	$\omega_{q,bec}/\omega_{ax}$	$\Gamma_{q,bec}/\omega_{ax}$
0.66 (6)	0.3	1.54 (3)	0.20 (3)	1.55 (3)	0.06 (2)
0.32 (3)	0.8	1.69 (2)	0.18 (2)	1.582 (9)	0.043 (9)
0.25 (5)	0.9	1.63 (2)	0.14 (2)	1.567 (9)	0.033 (9)
0.22 (5)	0.9	1.63 (2)	0.21 (3)	1.558 (8)	0.025 (9)
0.19 (5)	> 0.95	1.60 (2)	0.16 (3)	1.577 (9)	0.009 (9)

Table 4.1: The measured normalized frequency $\omega_{q,ex}/\omega_{ax}$ and the normalized damping rate $\Gamma_{q,ex}/\omega_{ax}$ of the thermal cloud and the normalized frequency $\omega_{q,bec}/\omega_{ax}$ and the normalized damping rate $\Gamma_{q,bec}/\omega_{ax}$ of the BEC for various temperatures T in terms of the transition temperature T_c . The condensate fraction $N_c/(N_c + N_{ex})$ is determined from the total absorption of both clouds.

increase in the damping rate to the interaction with the thermal cloud, since the density of the condensate is only slightly lower at higher temperatures.

A theoretical description of the quadrupole oscillation at finite temperature is given in Ref. [70]. Numerical results presented in that paper are based on the ENS trap parameters [64] and we have not calculated the damping rates for our parameters. Calculated damping rates for the condensate oscillation found in Fig. 5 of Ref. [70] show rates between $\Gamma_q/\omega_{ax} = 5 \cdot 10^{-4}$ and $1 \cdot 10^{-3}$. The rates found in our experiments are two orders of magnitude higher. Since the thermal cloud is well within the hydrodynamic regime, the regime in which the model is valid, we conclude additional damping mechanisms may play an important role, which are not included in the description given in Ref. [70], for instance damping due to fluctuations [72].

4.5 HIGHER ORDER EXCITATION

We observe a strong reduction of the condensate fraction if the cloud is excited too strong. Heating of the cloud is expected due to the strong excitation, but shortly after the excitation the density profile of the condensate shows an unexpected periodic density modulation. For a strong excitation we typically apply a large change in the trap frequency, $\Delta\omega/\omega \approx 50\%$, for a short duration, $t \approx 0.05/\omega$, although the density modulations are observed for a vast range of excitation parameters. We found one report of a similar excitation in Ref. [39]. In that paper the observation of similar density modulations is reported in the process of exciting a radial center-of-mass oscillation.

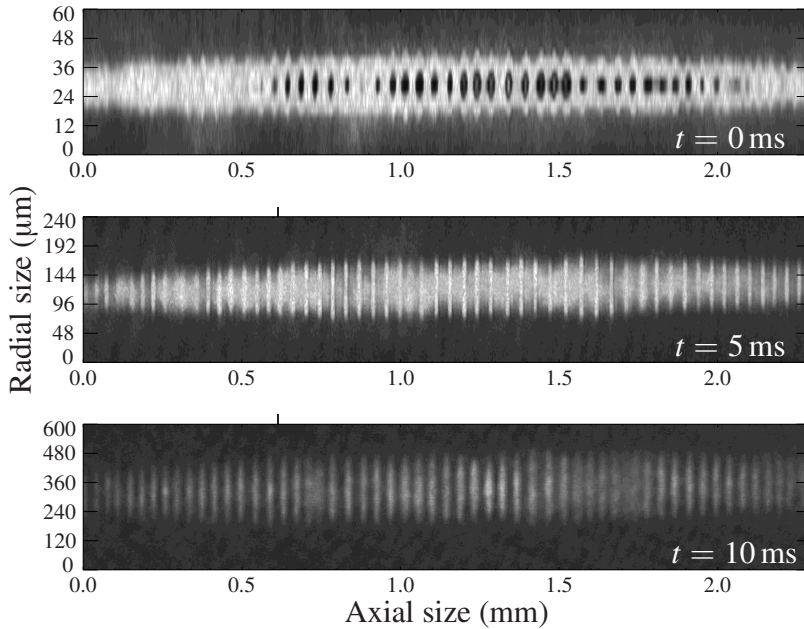


Figure 4.6: A series of phase contrast images of a BEC a third of a trap period after excitation. A periodic density modulation is observed *in situ* (top), after 5 ms time-of-flight (middle) and after 10 ms time-of-flight (bottom). Since the condensate expands mainly in the radial, vertical direction, the vertical scale is different in each image.

A third of a trap period after the initial excitation the highest contrast of the modulation is observed. The modulation vanishes equally over the entire cloud and reoccurs in the next oscillation, although the cloud is heated to such an extent that the condensate fraction becomes small and barely visible. We have not been able to excite any comparable density modulation in the thermal cloud. To make sure these density modulations are not the effect of phase fluctuations, which can also cause density modulations in time-of-flight, we examined the clouds *in situ*. The result of such a measurement, taken a third of a trap period after the excitation using the phase contrast imaging method (see Chapter 3) is shown in Fig. 4.6 for different expansion times.

We have excited clouds trapped in different axial confinements and find the number of nodes in the density profile to scale proportional to the length of the cloud. In Fig. 4.7 the number of nodes is plotted as a function of the axial length of the cloud. The maximum number of nodes, about 60, is found in a trap characterized by the axial trap frequency $\omega_{ax}/(2\pi) = 1.1$ Hz. For reasons unknown to us, we are unable to observe these excitations for the trap frequencies

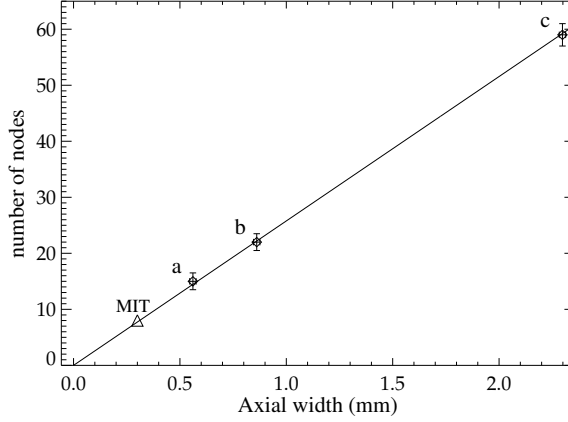


Figure 4.7: The number of nodes in the condensate density as function of the axial size of the condensate. The axial size is changed by varying the axial trap frequency; in Fig. a $\omega_{\text{ax}}/(2\pi) = 7.78$ Hz, in Fig. b $\omega_{\text{ax}}/(2\pi) = 3.91$ Hz and in (c) $\omega_{\text{ax}}/(2\pi) = 1.1$ Hz. The solid line is the result of a fit to a linear function in which the only free parameter is the slope, yielding 26 ± 1 nodes/mm, corresponding to a modulation wavelength $\lambda/2 = 39 \pm 2 \mu\text{m}$. The triangle is the result of the MIT group [39] and not used for in the fit.

$\omega_{\text{ax}}/(2\pi) \gtrsim 10$ Hz, although we expect to observe roughly ten nodes based on the extrapolation of the data points in Fig. 4.7. The number of nodes per unit length is determined by fitting the data points shown in Fig. 4.7 to a line going through the origin. From its slope we determine 26 ± 1 nodes/mm, corresponding to a wavelength $\lambda/2 = 39 \pm 2 \mu\text{m}$. In Ref. [39] the observation of 8 nodes is reported in a $300 \mu\text{m}$ long condensate of sodium atoms in a harmonic trap characterized by $\omega_{\text{rad}}/(2\pi) = 250$ Hz and $\omega_{\text{ax}}/(2\pi) = 17$ Hz. Surprisingly, the observed number of nodes per unit length, and thus λ , is the same as in our experiment, even though the trap parameters are different. λ is therefore expected to be independent of both the axial and radial confinement. In the experiment we are able to excite the density modulations in the BEC in a broad range of temperatures, also at temperatures where the condensate fraction exceeds 90%. λ differs from the typical length scales in our system: the thermal de Broglie wavelength $\Lambda_{\text{dB}} = (2\pi\hbar^2/mk_{\text{B}}T)^{1/2} < 1 \mu\text{m}$, the harmonic oscillator length $\bar{a} = (\hbar/(m\omega))^{1/2}$ is $2 \mu\text{m}$ in the radial direction and between $20 \mu\text{m}$ and $8 \mu\text{m}$ in the axial direction, and the healing length $\zeta = 1/\sqrt{8\pi an_c} \approx 0.1 \mu\text{m}$.

In order to determine the origin of the density modulation we have set up a computer based simulation in which the GPE (see Eq. (4.1)) is solved numerically using the time-splitting spectral method described in Ref. [73]. Since the experiments are done on very elongated, cigar-shaped BECs and all effects are

found in the axial directions, the calculation time can be reduced by solving an effective 1D equation in the limit of strong coupling [74]. Many experiments on both the statics and dynamics of BECs have shown that experiments can be modeled accurately by numerically solving the GPE, for example in experiments on interferometry [75] and superfluidity [76].

The simulations show excellent agreement of the oscillation frequency of the undamped quadrupole oscillation with the frequency given by Eq. (4.9), as long as the oscillation amplitude is small. For higher amplitudes the frequency slightly shifts, in agreement with findings in Ref. [69]. For stronger excitations the density profiles found in the simulation do not exhibit the characteristic strong, periodic modulations. We changed the excitation strength from values corresponding to the parameters for which the density modulations are observed in the experiment, to values up to a tenfold of this parameter. We also included a center-of-mass oscillation of the same magnitude as is observed in the experiments, but we found no influence of this motion on the quadrupole oscillation frequency, nor on the excitation of the density modulations. The inability to observe the density modulations in the model, whereas the quadrupole oscillation is correctly modeled, suggests the modulations are caused by effects not incorporated in the simulations, for instance 2D/3D effects or the interplay with the thermal cloud.

After the completion of this chapter it has come to our attention that similar density patterns have been observed by Engels and coworkers [77]. In their experiment a periodic modulation of the radial confinement excites the density modulation in the axial direction. They have shown that these modulations are the result of Faraday waves, which are caused by the nonlinear interactions in the BEC.

4.6 CONCLUSION & OUTLOOK

In conclusion, the quadrupole oscillation of the cloud of atoms is used to study the crossover from the collisionless regime to the hydrodynamic regime. We find the shift of the frequency and damping rate of this mode to agree well with both previous experimental work and theory. This measurement shows that the thermal cloud is already highly hydrodynamic above T_c . By cooling below the transition temperature we enter the hydrodynamic regime even deeper and we have succeeded in measuring the frequencies and damping rates of both the thermal cloud and condensate at various temperatures. We find good agreement with the theoretical prediction at low temperature, for which the thermal density becomes negligible. For higher temperatures the damping rate increases, which is attributed to the interactions between the hydrodynamic thermal cloud and the condensate.

Strong excitation of the cloud results in periodic density modulation in the condensate and we find the wavelength of this oscillation to be constant for

different axial and radial confinements. The density modulation, found in the experiment for a broad range of excitation parameters, has not been reproduced in a numerical 1D GPE simulation. Similar density patterns are shown to be the result of Faraday waves by Engels and coworkers. We are currently comparing our results with their findings.

Phase contrast imaging has been successfully used to image these oscillating clouds below T_c . Since this technique can be used to image the clouds in a non-destructive way, multiple images can be made of a single condensate during its oscillation. As an outlook, we plan to buy a new camera equipped with a “kinetics-mode” feature, allowing us to record multiple images of a single cloud, which reduces the measuring time dramatically. Furthermore, observing the dynamic behavior of a single cloud ensures the initial conditions are equal for all images in the batch. This reduces the measurement uncertainty and thus the measurement time. As a result, non-destructive imaging will allow us to make a more thorough measurement of the frequency and damping rate as a function of the temperature, condensate fraction or hydrodynamicity.

THERMAL CONDUCTIVITY IN A COLD THERMAL CLOUD

Abstract

We study the heat conduction of a cold, thermal cloud in a highly asymmetric trap. The cloud is axially hydrodynamic, but due to the asymmetric trap radially collisionless. By locally heating the cloud we excite a thermal dipole mode and measure its oscillation frequency and damping rate. We find an unexpectedly large heat conduction compared to the homogeneous case. The enhanced heat conduction in this regime is partially caused by atoms with a high angular momentum spiraling in trajectories around the core of the cloud. Since atoms in these trajectories are almost collisionless they strongly contribute to the heat transfer. We observe a second, oscillating hydrodynamic mode, which we identify as a standing wave sound mode.

5.1 INTRODUCTION

The field of Bose-Einstein condensation in dilute atomic gases provides a fruitful playground to test well-developed theories of quantum fluids. Research using Bose-Einstein condensates (BECs) can address open questions relating to the many-body aspects of two-component quantum liquids, namely the interaction between the hydrodynamic normal and the superfluid component at finite temperature [78]. After the first realization of BEC some pilot experiments have been carried out, but detailed experiments are missing [13, 59]. This has to be compared to the case of liquid helium below the λ point, where many experiments since the 1950s have added to our understanding of novel phenomena in quantum liquids, like collective excitations, first and second sound, and others. One of the drawbacks of liquid helium is that the interactions are so strong that a clear distinction between the two components is difficult.

The reason for the lack of detailed experiments in BECs to study quantum liquids and in particular the hydrodynamical aspects of it, is the limited number of atoms (typically 1–10 million) in the experiments leaving the thermal atoms virtually collisionless. Efforts to decrease the mean free path by increasing the

This chapter is based on the publication *Enhanced heat flow in the hydrodynamic-collisionless regime*, R. Meppelink, R. van Rooij, J. M. Vogels, and P. van der Straten, Phys. Rev. Lett. **103**: 095301, 2009.

confinement limits the lifetime of the sample, since the density is limited by three-body decay. This makes the observation of sound propagation in a BEC a challenge.

As to theory, hydrodynamical damping of trapped Bose gases has been described above and below the transition temperature T_c [78, 79]. These theories yield the oscillation frequencies and damping rates of several low-lying modes, where it is assumed that the sample is fully hydrodynamic in all directions. Experiments on dilute clouds of cold atoms are generally conducted in highly asymmetric traps. In these elongated, cigar-shaped geometries the mean free path of the atoms can become much shorter than the size of the cloud in the long, axial direction, but at the same time exceeds the size in the other, radial directions. In this so-called hydrodynamic-collisionless regime the system is axially hydrodynamic and radially collisionless. In our setup, described in detail in Chapter 2, we have created BECs containing up to $3 \cdot 10^8$ sodium atoms by evaporation of atoms in an axially strongly decompressed trap with an aspect ratio of 1 : 65. Hot atoms created in three-body collisions are able to leave the sample in this highly asymmetric trap, before they can heat other atoms in an avalanche [36]. The sample is axially hydrodynamic, but due to the large aspect ratio collisionless in the radial direction. Such samples seem ideal for the observation of sound propagation in the axial direction, since the axial length of the condensates exceeds a few mm. However, neither experiments nor theoretical descriptions exist to determine if the collisions in the radial direction will affect the damping rates to a degree that the observation of sound remains elusive.

From a practical point of view, the hydrodynamic-collisionless regime is of relevance for the realization of a continuous atom laser by evaporatively cooling a magnetically guided atom beam [80]. Here the efficiency of the cooling process is expected to be limited by the heat transfer between the hot, upstream and cold, downstream parts of the beam.

In this chapter we report the experimental determination of the heat conduction in a cold, thermal gas above the transition temperature T_c , which is hydrodynamic in the axial direction, but collisionless in the radial directions. The heat conduction is determined by locally heating the cloud and subsequently observing the equilibration of the temperature distribution. Two previously unobserved hydrodynamic modes are reported; a thermal dipole mode and a standing wave sound mode. Furthermore, by reducing the number of atoms the crossover in the axial direction from the hydrodynamic regime to the collisionless regime is observed. We find that the heat conduction is five times stronger than calculations for the homogeneous case predict.

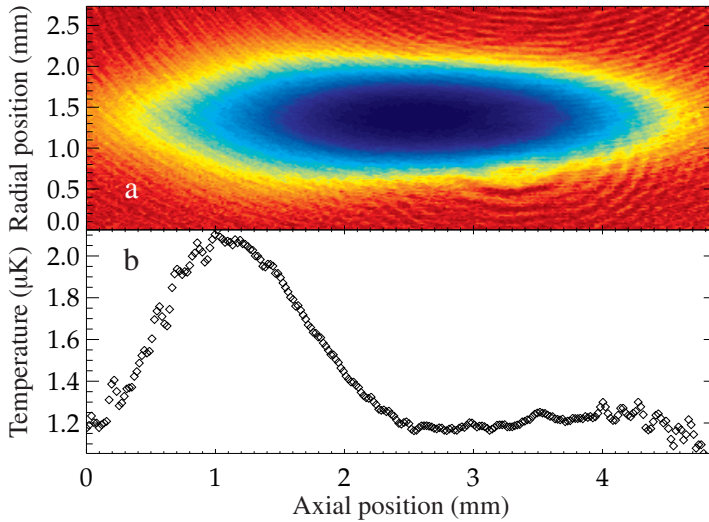


Figure 5.1: A locally heated cloud immediately after the excitation procedure is applied. The cloud in Fig. a is imaged after a time-of-flight of 40 ms. Figure b shows the temperature of the cloud as a function of its axial position.

5.2 EXPERIMENT

We measure the heat flow by locally heating the thermal cloud, after which the equilibration is studied. The heat is induced by exciting the thermal cloud using Bragg scattering with a laser beam aligned perpendicular to the axial axis of the cloud, which is aimed at its tail and retro-reflected [81]. The $(1/e)$ -width of the intensity of this beam is 0.8 mm, which is close to half of the axial $(1/e)$ -size of the cloud. The asymmetric excitation is chosen, since it yields the maximum separation between the cold, unperturbed part and the heated part of the cloud, resulting in a long observation time. The laser beam is detuned 2 nm below of the $^{23}\text{Na } D_2$ transition in order to reduce resonant scattering and prevent superradiant scattering. The excited particles will locally redistribute their momentum and energy through collisions with the other particles, resulting after a few collisions in a *local* thermal equilibrium. In the experiment the laser beam with an intensity $I = 100 \text{ mW/cm}^2$ is pulsed on five times for $500 \mu\text{s}$ with 1 ms in between the sequential pulses. A single pulse can transfer at maximum $\pm 2\hbar k$ of momentum per atom; rethermalization in between the pulses allows for transferring more energy to the cloud. We have confirmed that when the beam contains only one frequency, i. e. not satisfying the Bragg condition, that the temperature and the number of atoms remain unchanged. Figure 5.1 shows a locally heated cloud immediately after the excitation procedure is applied.

The experiments are conducted on a cloud containing up to $1.3 \cdot 10^9$ atoms confined in a clover leaf type magnetic trap (MT) characterized by the radial trap frequencies $\omega_{\text{rad}}/(2\pi) = 95.6 \text{ Hz}$ and the axial trap frequency $\omega_{\text{ax}}/(2\pi) = 1.46 \text{ Hz}$ at a temperature between $1.2 \mu\text{K}$ and $2 \mu\text{K}$, which is above $T_c \approx 1 \mu\text{K}$. Once a cloud is excited, it is allowed to rethermalize in the MT during an adjustable hold time τ , after which the confinement is turned off and an absorption image is taken after time-of-flight (TOF). The TOF duration is chosen in such a way that the optical density will not exceed 3.5, resulting in a time-of-flight of 40 ms for the highest number of atoms.

We introduce a measure for the hydrodynamicity in the axial direction $\tilde{\gamma} \equiv \gamma_{\text{col}}/\omega_{\text{ax}}$, where the collision rate $\gamma_{\text{col}} = n_{\text{eff}}\sigma v_{\text{rel}}$ is the average number of collisions. Here, the relative velocity $v_{\text{rel}} = \sqrt{2}\bar{v}_{\text{th}}$, where $\bar{v}_{\text{th}} = \sqrt{8k_{\text{B}}T/m\pi}$ is the thermal velocity at temperature T and m is the mass and $\sigma = 8\pi a^2$ is the isotropic cross section of two bosons with s -wave scattering length a . Furthermore, $n_{\text{eff}} = \int n^2(\mathbf{r}) dV / \int n(\mathbf{r}) dV = n_0/\sqrt{8}$ for an equilibrium distribution in a harmonic potential, where n_0 is the peak density. Written in terms of the number of atoms $N = n_0 (2\pi k_{\text{B}}T / (m\bar{\omega}^2))^{3/2}$ and the geometric mean of the angular trap frequencies $\bar{\omega}^3 \equiv \omega_{\text{rad}}^2 \omega_{\text{ax}}$, this results in $\gamma_{\text{col}} = Nm\sigma\bar{\omega}^3 / (2\pi^2 k_{\text{B}}T) \approx 90 \text{ s}^{-1}$ for the highest number of atoms and corresponds to a hydrodynamicity of $\tilde{\gamma} \lesssim 10$ in the axial direction. Even at the highest hydrodynamicity the lifetime of the cloud, limited by three-body decay, is more than 60 s, which is more than sufficient for the experiments described below. Note that the hydrodynamicity parameter in the radial direction is due to the anisotropic trap potential $\tilde{\gamma}_{\text{rad}} \lesssim 10/65$ and the cloud is in the radially collisionless regime. By reducing the number of atoms the heat flow through the thermal cloud can also be measured in the axially collisionless regime.

The images are analyzed using a least square fit to a 2D Gaussian distribution. In this distribution the radial size as a function of the axial position is modeled by a hyperbolic tangent function which adds a gradient to the width that resembles the asymmetric distribution. The fit to the 2D distribution yields the temperature gradient, axial and radial cloud sizes, and the optical density. In the following we will focus on the temperature gradient, which is a measure of the imbalance of the temperature in the cloud. In this analysis we assume that a local temperature equilibrium is established at all times. Since this is not a valid assumption in the first few tenths of milliseconds after excitation especially for lower collision rates, we cannot accurately describe the data at these times.

Heating the thermal cloud will also cause a quadrupole motion of the atoms, since the cloud is excited non-adiabatically to a higher temperature. Since the resulting compression and decompression is homogeneous over the cloud it does not influence the temperature gradient. The quadrupole mode, induced by perturbing the magnetic confinement, has been studied experimentally by Buggle and coworkers [14] and in chapter Chapter 4 of this thesis. The damping

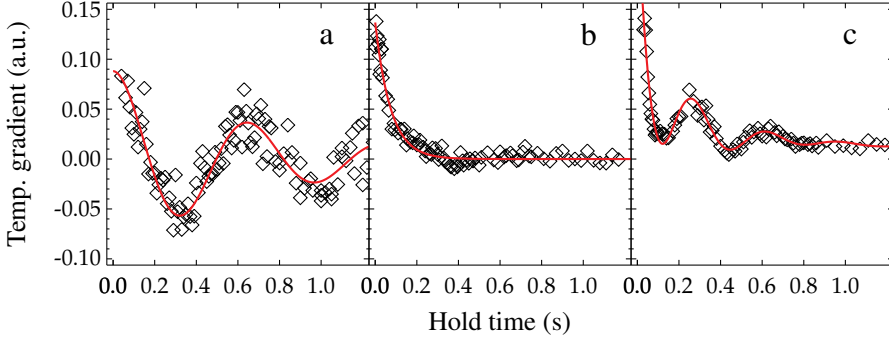


Figure 5.2: The temperature gradient as a function of the hold time τ for three values of the hydrodynamicity parameter $\bar{\gamma}$: $\bar{\gamma} \approx 1$ (Fig. a), $\bar{\gamma} \approx 3$ (Fig. b), $\bar{\gamma} \approx 7.5$ (Fig. c). In Figure a the behavior is collisionless, where the heat propagates through the MT almost undamped. In Fig. b the behavior is neither collisionless nor hydrodynamic and the temperature gradient is nearly critically damped. In Fig. (c) the behavior is hydrodynamic and the damping rate is therefore lower compared to (Fig. b), but a distinctive oscillatory behavior can be identified.

rate and oscillation frequency of this mode are found to be in good agreement with a theoretical model [65]. Since the quadrupole mode damps slower than the thermal dipole mode considered in this chapter, the maximum hold time for most of our measurement series turns out to be insufficient to accurately determine the damping rate of the quadrupole mode. Although our results are less accurate, we have confirmed that the frequency and damping rate of the quadrupole mode are in agreement with the results reported in Refs. [14, 65].

A series of measurements consists of about 100 shots at various hold times τ from which the temperature gradient is determined. The number of atoms and temperature is determined from an average over all shots, which yields the hydrodynamicity $\bar{\gamma}$. We plot the temperature gradient as a function of τ for three values of $\bar{\gamma}$ in Fig. 5.2.

5.3 RESULTS AND DISCUSSION

Figure 5.2a is the result of a measurement at small $\bar{\gamma}$ and shows a slowly damped oscillation, where the temperature gradient after half a trap oscillation has changed sign. The heated atoms are then at the opposite side of the cloud with respect to the excitation side, oscillating a frequency $\omega_d/\omega_{ax} = 1$. We refer to this mode as the thermal dipole mode, which has not been observed previously. The oscillation frequency ω_d and damping rate Γ_d are determined by fitting the data to a damped sinusoid and are shown in Fig. 5.3 as a function of $\bar{\gamma}$. For small

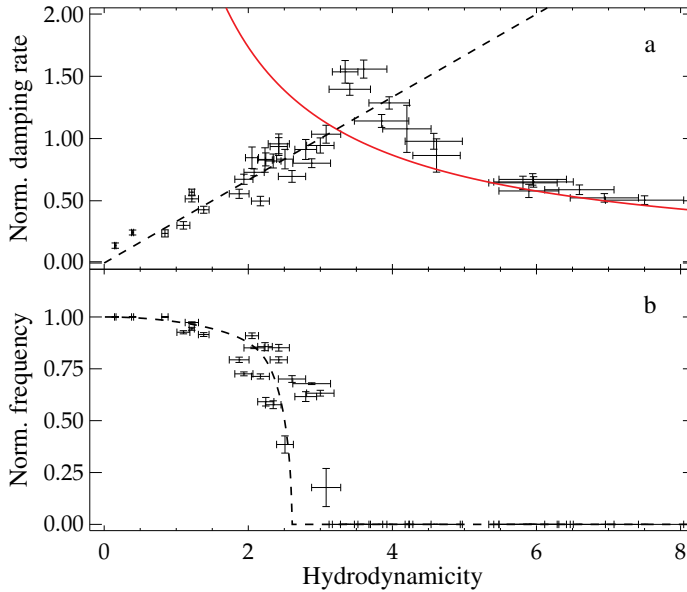


Figure 5.3: The measured normalized damping rate Γ_d/ω_{ax} (Fig. a) and normalized frequency ω_d/ω_{ax} (Fig. b) of the thermal dipole mode as a function of the hydrodynamicity $\tilde{\gamma}$. The solid line in (Fig. a) is a fit of the data points with $\tilde{\gamma} > 5$ to the solution of Eq. (5.1) with $\kappa_0 = 6.4$. The dashed lines are a guide to the eye. The vertical error bars show only statistical errors; the main contribution to the uncertainty in $\tilde{\gamma}$ is the uncertainty in the number of atoms.

collision rates ($\tilde{\gamma} \approx 1$) the damping rate is proportional to the collision rate. As a consequence the frequency of the mode will decrease for increasing $\tilde{\gamma}$ until it reaches zero, when the system is critically damped. In the experiment we observe oscillatory behavior for $\tilde{\gamma} \lesssim 2.5$.

For higher values of $\tilde{\gamma}$ the temperature gradient as a function of τ becomes critically damped, as can be seen in Fig. 5.2b. For even higher values of $\tilde{\gamma}$ the system becomes hydrodynamic and atoms cannot move through the cloud without colliding frequently. The heat transport will become diffusive, which is a slower process than the harmonic oscillation. As a consequence we expect the damping of the temperature gradient to decrease, but remain non-oscillatory. A measurement for high $\tilde{\gamma}$ is shown in Fig. 5.2c. For $\tau < 0.1$ s, a double exponential decay can be seen, where the fast decay due to higher order modes and the slow decay of the lowest thermal dipole mode can be discriminated from each other due to the strong inequality of the damping rates. The reduced chi-squared for all fits are of the order of unity, as can also be seen from Fig. 5.2, since the curves go smoothly through the data points.

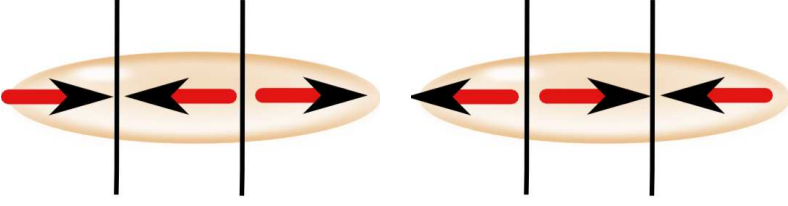


Figure 5.4: Schematic representation of the oscillating, higher order hydrodynamic mode, a standing wave sound mode. The vertical lines indicate the velocity nodes, the arrows indicate the motion of the atoms.

The measurements in the hydrodynamic regime can be analyzed by numerically solving the heat diffusion equation in the axial direction

$$c_p n(z) \frac{\partial}{\partial t} T(z, t) = \frac{\partial}{\partial z} \left[\kappa \frac{\partial}{\partial z} T(z, t) \right]. \quad (5.1)$$

Here the specific heat capacity $c_p = 7/2$, the heat conductivity $\kappa \equiv \kappa_0 \pi v_{\text{th}} \Sigma / (\sqrt{8} \sigma)$ with κ_0 the dimensionless heat conductivity coefficient and $\Sigma = 2\pi k_B T / (m \omega_{\text{rad}}^2)$ is the effective cloud surface. The damping rate of the lowest order solution in this regime is found to be $\Gamma_d = 0.542 \kappa_0 / \bar{\gamma}$. Fitting the measurements for Γ_d with $\bar{\gamma} > 5$ yields $\kappa_0 = 6.4 \pm 0.4$. This value is a factor of five larger than the Chapman-Enskog value $\kappa_0 = 75/64 \approx 1.17$ for a homogeneous hydrodynamic system [82, 83].

The measurements in the hydrodynamic regime also show a damped oscillation of the decay of the temperature gradient for $\tau > 0.1$ s (see Fig. 5.2c). As this oscillation is only seen in the hydrodynamic regime, where the collisionless oscillation is completely damped out, we conclude that it is the result of another hydrodynamic mode, which we identify as a standing wave sound mode. In our experiments this sound mode can only be seen for values of $\bar{\gamma}$ exceeding 5. Using a least-square fit we determine both the oscillation frequency ω_s and damping rate Γ_s of the sound mode for all values of $\bar{\gamma} > 5$ as a function of $\bar{\gamma}$ (see Fig. 5.5). The measured normalized frequency $\omega_s / \omega_{\text{ax}} \approx 2.1$ confirms that the mode differs from a center-of-mass motion ω_{ax} and the quadrupole mode $\omega_q / \omega_{\text{ax}} \approx \sqrt{12/5}$ [65].

This sound mode can be found theoretically by solving the hydrodynamic equations [79] in the limit of no damping and we find $\omega = \sqrt{19/5} \omega_{\text{ax}} \approx 1.95 \omega_{\text{ax}}$. This mode resembles the quadrupole mode, although the standing wave sound mode is even in the axial velocity v_z and has two nodes in the velocity profile instead of one. A schematic representation of this mode is given in Fig. 5.4. As a consequence, this sound mode contributes to the temperature gradient and can

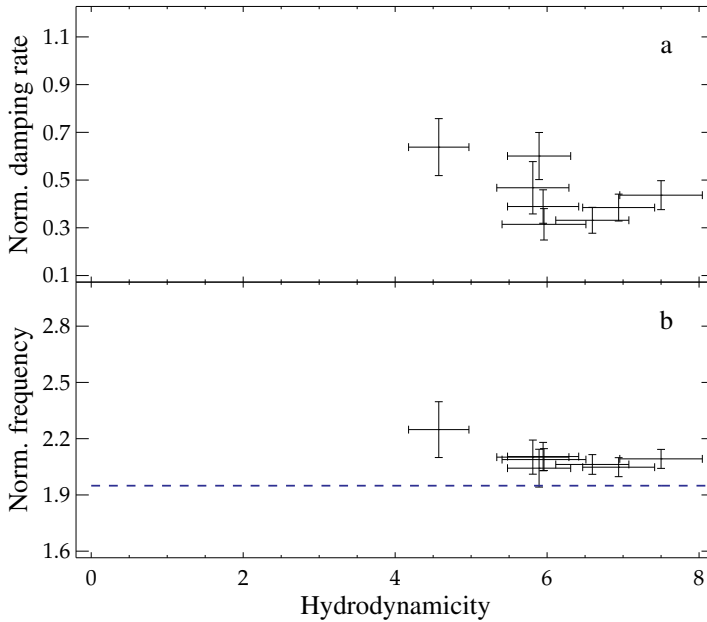


Figure 5.5: The measured normalized damping rate $\Gamma_s/\omega_{\text{ax}}$ (Fig. a) and normalized frequency $\omega_s/\omega_{\text{ax}}$ (Fig. b) of the hydrodynamic sound mode as a function of the hydrodynamicity $\bar{\gamma}$. The dashed line shows the frequency of this mode in the limit of no damping, $\omega = \sqrt{19/5}$.

be observed in Fig. 5.2c. This is the first direct experimental observation of a thermal sound mode in a cold gas.

A rigorous theoretical model to calculate the oscillation frequency and damping rate of the modes for arbitrary hydrodynamicity $\bar{\gamma}$ will be presented in Ref. [84]. The analysis yields $\kappa_0 = 5.98$ in the hydrodynamic-collisionless regime, which confirms the experiment. Furthermore, for a linear confinement as is used for magnetically guided atomic beams the enhancement of the heat flow is even stronger; up to two orders of magnitude. This result implies that the efficiency of evaporatively cooling of a linearly guided atomic beam is strongly diminished due to the large heat flow and questions the feasibility of realizing a continuous atom laser. The increase of κ_0 is found to be caused by two effects. First, the shape of the density of states is altered, which results in a relatively lower collision rate and causes the presence of more atoms with a high transverse energy. The second effect lies in the presence of atoms with a high angular momentum. These atoms are in trajectories spiraling around the core of the cloud. These trajectories are almost collisionless and cause a very strong contribution to the heat flow.

5.4 CONCLUSION

In conclusion, we have successfully excited and measured two previously unobserved modes; a thermal dipole mode and a standing wave sound mode. Observation of the latter demonstrates both the hydrodynamic behavior of the cloud and the presence of sound propagation in a dilute thermal gas. In the hydrodynamic regime we have measured the heat conduction coefficient $\kappa_0 = 6.4 \pm 0.4$, which is five times higher than calculations for the homogeneous case predict. This effect is expected to be even stronger for a linear confined cloud in the axially hydrodynamic-radially collisionless regime. This result implies that the efficiency of evaporative cooling in a continuous atom laser, where the confinement is linear, is strongly reduced by the large heat transfer between the hot and cold parts of the beam.

A THERMAL WAVE IN THE TWO-FLUID REGIME

Abstract

We have studied the propagation of a temperature wave in a BEC at finite temperature. The excitation procedure is similar to the one used above T_c in Chapter 5 for the excitation of a thermal dipole mode. Above T_c we have observed a number of different modes, and below T_c the number of excited modes is even larger, since the condensate introduces a new degree of freedom. Furthermore, some of the modes couple with a strength depending on the temperature. We succeeded in identifying seven distinct modes and present its damping rates and oscillation frequencies in this chapter. In the absence of a theoretical description of most of the excited modes in the two-fluid regime, we cannot quantitatively compare the measured damping rates and frequencies to theory. The data presented here can be used as a testing ground for the development of these theories and can deepen the understating underlying the interactions in the two-fluid regime.

6.1 INTRODUCTION

In this chapter we extend the thermal conductivity measurements described in Chapter 5 to temperatures below T_c . Above T_c we have locally heated the thermal cloud and excited a thermal dipole mode. Furthermore, we have observed a second, oscillating hydrodynamic mode, which we have identified as a standing wave sound mode. Below T_c both a hydrodynamic thermal cloud and a superfluid condensate coexist and we aim at exciting a collective excitation to study the interplay between both components in this two-fluid system. In Chapter 4 the collective excitation studied is a shape oscillation; the quadrupole oscillation. Here, we explore the conditions to excite second sound, a collective excitation for which the density of the condensate and the normal component oscillate out-of-phase. The experimental attempts to excite second sound in gaseous BEC have been very limited. In a pioneering experiment by Jin *et al.* the observation of a strong temperature dependent damping and frequency shift have been attributed to coupling with a second sound mode [59], although the cloud is in the collisionless regime. In an experiment by Stamper-Kurn *et al.* [13] the

hydrodynamic regime is reached and the excitation of an out-of-phase dipole mode of the thermal cloud and the BEC is observed, the analogous of second sound. However, this mode is only excited for a single set of experimental parameters. In the two-fluid regime the modes of the BEC and the thermal cloud are expected to couple and possibly cause strong damping, for instance through thermal conductivity. Strong damping will complicate the observation of propagating sound modes.

Above T_c we observe additional modes upon excitation of the thermal dipole mode; a quadrupole mode and a standing wave sound mode, as well as higher order modes, which have higher damping rates and can thus be distinguished from the lower order modes. Below T_c the number of excited modes is even larger, since the condensate introduces a new degree of freedom. Furthermore, some of the modes couple, and the strength of the coupling depends on the temperature. In this chapter we study the coupling due to the interaction between the thermal cloud and the BEC by analyzing the damping rates and frequencies as a function of the temperature.

6.2 EXPERIMENT

We locally excite the cloud with the same procedure as is used for the excitation of the thermal dipole mode above T_c (see Chapter 5). Briefly, the cloud is locally heated using Bragg scattering with a laser beam, which is aligned perpendicular to the axial axis of the cloud, aimed at the edge of the condensate and retro-reflected. The $(1/e)$ -width of the intensity of this beam is 0.15 mm, about 10 % of the axial condensate radius. The laser beam is detuned 2 nm below the ^{23}Na D_2 transition in order to reduce resonant scattering and prevent superradiant scattering. First order Bragg scattering at an angle π will induce a momentum transfer $p = 2\hbar k$ if the energy deficit for the two photon transition of approximately $h \times 100$ kHz is supplied for by the frequency difference in the beams [81]. Since the laser beam contains both frequencies needed for Bragg scattering, both plus and minus $2\hbar k$ can be transferred. The intensity and pulse duration are decreased compared to the excitation scheme used above T_c to ensure that mainly the condensed atoms are excited. Bragg diffraction is less efficient for atoms in a thermal cloud than it is for atoms in a BEC due to the increased Doppler width of the thermal atoms. The excited atoms will collide frequently, since the collision rate is higher than the radial trap frequency. As a consequence, these atoms redistribute their momentum and energy through collisions resulting in condensed atoms being excited. Furthermore, the local condensate density is decreased, while the local thermal density and temperature are increased until a local equilibrium is established roughly within a radial trap period. A schematic representation of the excitation procedure and an absorption image taken shortly after the excitation are shown in Fig. 6.1. The experiments are conducted on

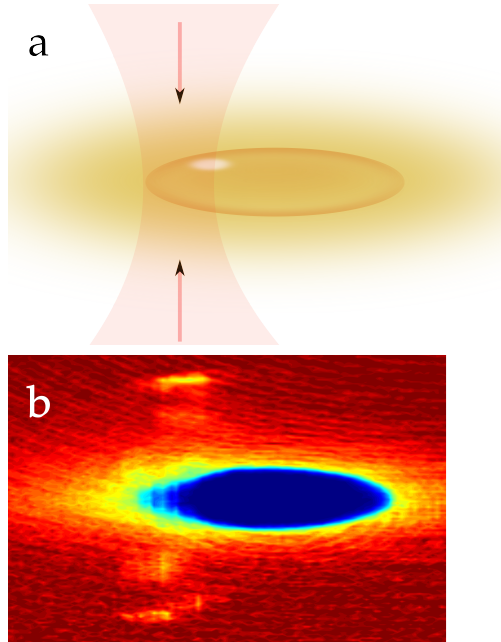


Figure 6.1: Excitation procedure of a thermal wave in a BEC at finite temperature. Figure a shows a schematic representation of the Bragg beam aligned on a BEC and thermal cloud. Figure b shows an absorption image of an excited cloud, directly after the excitation is applied. The cloud has expanded during a time-of-flight for 60 ms and the atoms with $p = \pm 2\hbar k$ are spatially separated. The resulting peaks can be seen both above and below the cloud. These atoms have already collided due to the high collision rate, resulting in the observation of condensed atoms in between the cloud and the peaks.

clouds at various temperatures below $T = T_c$, where the cloud at $T = T_c$ contains roughly $1.3 \cdot 10^9$ atoms. The atoms are confined in a clover leaf type Magnetic Trap (MT) characterized by the radial trap frequencies $\omega_{\text{rad}}/(2\pi) = 95.6$ Hz and axial trap frequency $\omega_{\text{ax}}/(2\pi) = 1.46$ Hz. The final temperature is varied between $T \lesssim T_c$ and $T \approx \mu/k_B$ by tuning the rf-field frequency of the evaporative cooling. In this confinement the BEC contains up to $N_c = 2.5 \cdot 10^8$ atoms. Fig. 6.2 shows the motion of the cloud at various times τ after the excitation of the thermal wave.

Five measurement series, one of the series is shown in Fig. 6.2, are conducted for different temperatures below T_c . Each series, consisting of about 100 shots at various hold times τ , is analyzed by fitting the images. The fit function used is a bimodal distribution, which is the sum of a Maxwell-Bose distribution describing

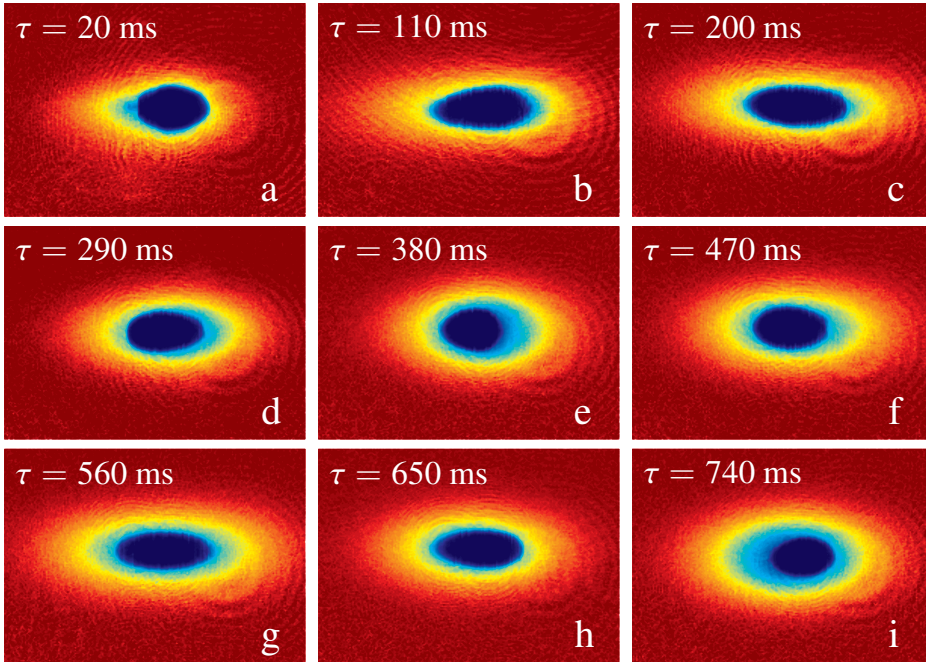


Figure 6.2: Absorption images of a BEC ($\mu = 4 \text{ kHz}$, $T = 0.3 \mu\text{K}$) at various times τ after the cloud is excited. The difference in τ between succeeding figures is $\Delta\tau = 90 \text{ ms}$. In these figures we focus on motion of the temperature wave, causing the condensate density to decrease locally. Figure a at $\tau = 20 \text{ ms}$ shows the decreased condensate fraction at the left side of the BEC, the position of the excitation causing an egg-shaped, asymmetric density profile. In Fig. b to Fig. d the position of the minimum of the condensate fraction propagates to the right side of the BEC, reaching the right side in Fig. e, at $\tau = 380 \text{ ms}$. In Fig. f to Fig. h the temperature wave propagates to the left again, reaching the left side in Fig. i at $\tau = 740 \text{ ms}$. The clouds are imaged after free expansion during time-of-flight for 60 ms .

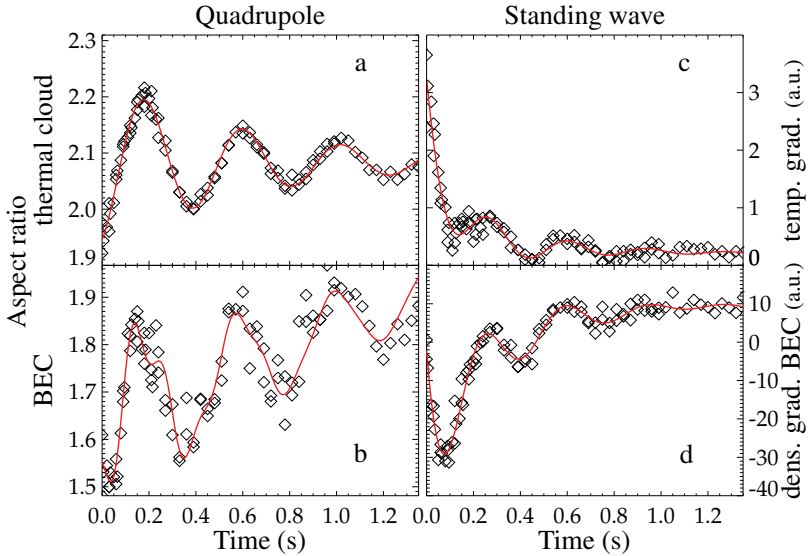


Figure 6.3: The collective behavior of the thermal cloud and BEC as a function of τ for $N_c = 2 \cdot 10^8$ atoms, $N_{ex} = 8 \cdot 10^8$ atoms and $T = 0.8 \mu\text{K}$. Figures a and b show the aspect ratio of the thermal cloud, respectively the BEC, and reflects the quadrupole oscillation. Figure c shows the temperature gradient of the thermal cloud, where the oscillatory behavior is the result of the standing wave sound mode. Figure d shows the density gradient of the BEC in which a similar oscillation as the standing wave sound mode is observed. The solid lines are the result of a fit to the data.

the thermal cloud and a TF distribution describing the BEC. In this distribution the radial size as a function of the axial position of both components is modeled by a hyperbolic tangent function, which adds a gradient to the width that resembles the asymmetric distribution. The fit to the 2D distribution yields ten parameters, which will be used in the subsequent analysis: the axial and radial sizes, the axial position, the optical density and the width gradient of both the thermal cloud and the BEC.

A large number of different modes are excited. In the thermal cloud the modes observed above T_c are found below T_c as well. The quadrupole mode is excited, since the temperature is non-adiabatically increased. We plot the aspect ratio of the thermal cloud as a function of τ for two temperatures in Figs. 6.3a and 6.4a. Locally heating the cloud results in the excitation of the thermal dipole mode and the standing wave sound mode, observed in the measured temperature gradient, which is shown in Figs. 6.3b and 6.4b as a function of τ .

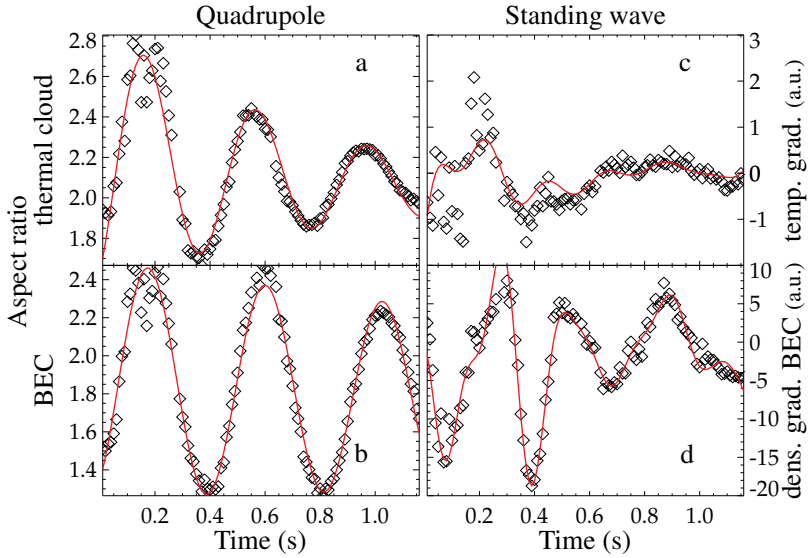


Figure 6.4: The collective behavior of the thermal cloud and BEC as a function of τ for $N_c = 2.5 \cdot 10^8$ atoms, $N_{ex} = 5 \cdot 10^7$ atoms and $T = 0.3 \mu\text{K}$. The description of the figure is given in the caption of Fig. 6.3.

Equivalent modes to the modes excited in the thermal cloud are observed in the BEC as well. The aspect ratio of the BEC is plotted in Figs. 6.3c and 6.4c as a function of τ and shows that a quadrupole oscillation is excited in the BEC as well. Analogous to the temperature gradient in the thermal cloud, which is observed as a width gradient in the density of the thermal cloud, we observe a width gradient in the condensate density. The width gradient in the BEC is associated with a density gradient and it is found to oscillate as a function of τ . The density gradient of the BEC is shown in Figs. 6.3d and 6.4d. Note that the egg-shaped density profiles shown in Fig. 6.2 reflect the observed BEC density gradient described above. This mode is the equivalent of the standing wave sound mode in the thermal cloud.

The excitation of the temperature wave not only causes the local condensate density to decrease, it eventually causes the cloud to equilibrate to the higher temperature. As a result, the condensate fraction will decrease until the new equilibrium is established. We define the condensate fraction by the total absorption of the BEC divided by the total absorption of both components and plot it in Fig. 6.5 as a function of τ . For high temperatures the condensate fraction as a function of τ is found to decrease linearly. However, for lower temperatures an oscillatory decay of the condensate fraction is observed, as can be seen clearly in Fig. 6.6a.

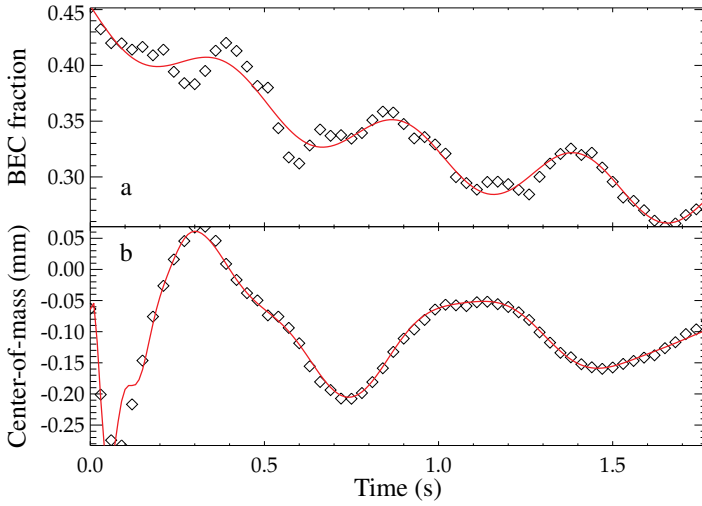


Figure 6.5: The condensate fraction (Fig. a) and out-of-phase dipole oscillation (Fig. b) as a function of τ ; $N_c = 2 \cdot 10^8$ atoms, $N_{ex} = 4 \cdot 10^8$ atoms and $T = 0.5 \mu\text{K}$. The solid lines are the result of a fit to the data.

Finally, the axial position of the center-of-mass of both the BEC and thermal cloud is displaced during the excitation procedure. Since the condensate density is locally reduced a center-of-mass motion is induced. This motion is initially in the opposite direction of that of the BEC, since the thermal density is increased where the cloud is excited. Since the thermal cloud and the BEC start moving in opposite direction we refer to this mode as the out-of-phase dipole mode. The difference between the center-of-mass position in the axial direction of the BEC and the thermal cloud is shown in Figs. 6.5b and 6.6b as a function of τ .

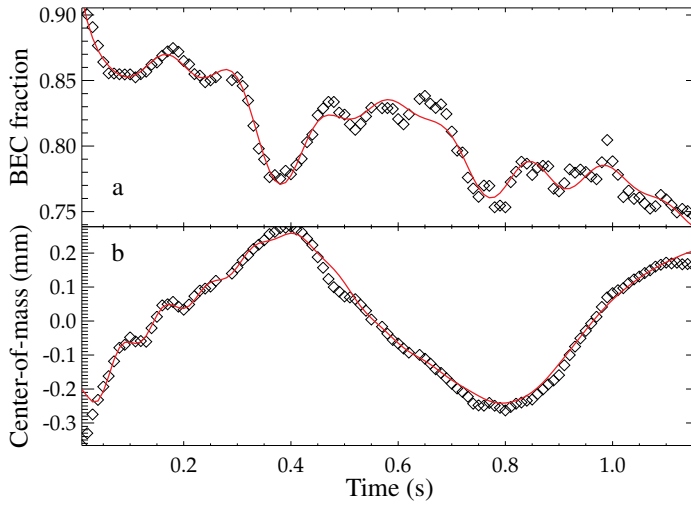


Figure 6.6: The condensate fraction (Fig. a) and out-of-phase dipole oscillation (Fig. b) as a function of τ for identical parameters as in Fig. 6.4. The solid lines are the result of a fit to the data.

6.3 IDENTIFIED MODES

#	MODE	OBSERVED IN	RESULTS
1	Quadrupole mode	Thermal cloud	Fig. 6.7
2	Quadrupole mode	BEC	Fig. 6.7
3	Thermal dipole mode	Thermal cloud	Fig. 6.8
4	Standing wave sound mode	Thermal cloud	Fig. 6.9
5	Standing wave sound mode	BEC	Fig. 6.9
6	Oscillating condensate fraction	Thermal cloud & BEC	Fig. 6.10
7	Out-of-phase dipole mode	Thermal cloud & BEC	Fig. 6.11

Table 6.1: A summary of the seven identified modes. The measured damping rate and frequency of the mode can be found in the stated figure.

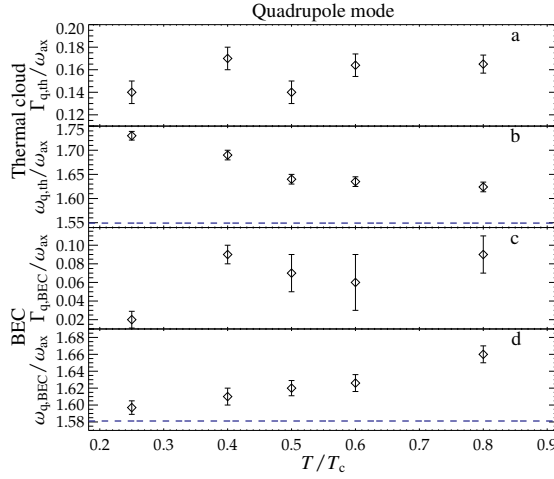


Figure 6.7: The normalized damping rate $\Gamma_{q,ex}/\omega_{ax}$ (Fig. a) ($\Gamma_{q,BEC}/\omega_{ax}$, (Fig. c)) and normalized frequency $\omega_{q,ex}/\omega_{ax}$ (Fig. b) ($\omega_{q,BEC}/\omega_{ax}$ (Fig. d)) of the quadrupole mode of the thermal cloud (the BEC) as a function of the reduced temperature T/T_c . The dashed line in Fig. b indicates the value in the hydrodynamic limit $\Gamma_q/\omega_{ax} = \sqrt{12/5}$ and in Fig. d the $T = 0$ prediction $\Gamma_q/\omega_{ax} = \sqrt{5/2}$.

In the remaining part of this chapter we will discuss the measured damping rates and oscillation frequencies for each of the seven identified modes. A summary of these modes is given in Table 6.1. In the absence of a theoretical description of the observed modes and the effects of the interplay between both components the discussion is restricted to a qualitative interpretation of the measured rates and frequencies.

6.3.1 The quadrupole mode

For all temperatures the oscillation of the thermal quadrupole mode is similar to the data shown in Figs. 6.3a and 6.4a. The data is fitted to a single damped sinusoid, from which the damping rate $\Gamma_{q,ex}$ and oscillation frequency $\omega_{q,ex}$ are determined. The normalized damping rate $\Gamma_{q,ex}/\omega_{ax}$ and normalized oscillation frequency $\omega_{q,ex}/\omega_{ax}$ are shown in Fig. 6.7 as a function of the reduced temperature T/T_c . For high temperatures the oscillation frequency is close to the value found above T_c . We observe that $\omega_{q,ex}$ increases for decreasing temperature. Above T_c , an increase of $\omega_{q,ex}$ due to the crossover toward the collisionless regime is accompanied by an increase in $\Gamma_{q,ex}$. Since $\Gamma_{q,ex}$ remains roughly unchanged, we consider this shift to be caused by the interaction between the thermal and condensed atoms rather than by the crossover toward the collisionless regime. In

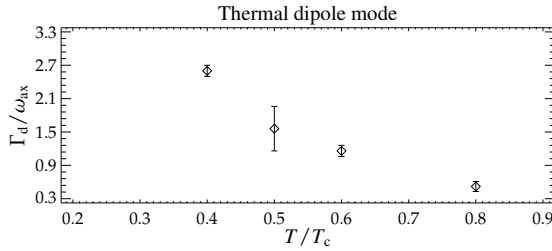


Figure 6.8: The normalized damping rate Γ_d/ω_{ax} of the thermal dipole mode of the thermal cloud as a function of the reduced temperature T/T_c .

the aspect ratio of the BEC a damped oscillation is observed, although for the highest temperatures its offset value increases as well. In the first few hundreds of milliseconds a strongly damped, additional oscillation is observed and its occurrence is found to coincide with a significant temperature gradient in the thermal cloud, discussed in the next section. By analyzing only the data points with $\tau > 200$ ms the combination of a single damped sinusoidal function and a linear slope describes the data sufficiently well at all temperatures and is used to determine the damping rate $\Gamma_{q,BEC}$ and frequency $\omega_{q,BEC}$. The normalized damping rate $\Gamma_{q,BEC}/\omega_{ax}$ and normalized oscillation frequency $\omega_{q,BEC}/\omega_{ax}$ are shown in Fig. 6.7. For low temperatures the frequency is close to the predicted $T = 0$ value $\omega/\omega_{ax} \approx 1.58$. For higher temperatures the oscillation frequency increases, as does the damping rate and we attribute these shifts to interactions between the BEC and the thermal cloud.

6.3.2 Thermal dipole mode and standing wave sound mode

The temperature gradient, which can only be observed in the thermal cloud, is analyzed with the same procedure as is used for the analysis of the thermal dipole mode for temperature above T_c (see Chapter 5). Except for the lowest temperature, a double exponential decay can be seen, where the fast decay due to higher order modes and the slow decay Γ_d of the thermal dipole mode can be discriminated from each other due to the strong inequality of the damping rates. The normalized damping rate Γ_d/ω_{ax} of the thermal dipole mode as a function of the reduced temperature is shown in Fig. 6.8. The damping rate for high temperature is slightly lower than the measured value under the most hydrodynamic conditions above T_c . The damping rate increases strongly for decreasing temperature, until only a damped oscillatory behavior is observed in the temperature gradient (compare Figs. 6.3c and 6.4c).

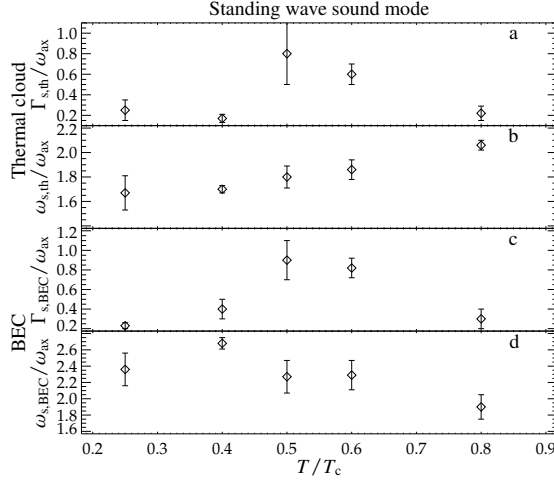


Figure 6.9: The normalized damping rate $\Gamma_{s,ex}/\omega_{ax}$ (Fig. a), the normalized frequency $\omega_{s,ex}/\omega_{ax}$ (Fig. b) and the normalized damping rate $\Gamma_{s,BEC}/\omega_{ax}$ (Fig. c), the normalized frequency $\omega_{s,BEC}/\omega_{ax}$ (Fig. d) of the standing wave sound mode in the thermal cloud and the BEC, respectively as a function of the reduced temperature T/T_c .

For $\tau > 0.1$ s a damped oscillation in the temperature gradient is observed, similar to the measurements above T_c , where this oscillation is identified as a standing wave sound mode. Using a least-square fit we determine both the oscillation frequency ω_s and damping rate Γ_s of the sound mode. The normalized damping rate $\Gamma_{s,ex}/\omega_{ax}$ and normalized frequency $\omega_{s,ex}/\omega_{ax}$ of this mode are shown in Fig. 6.9. The frequency for the highest temperature is similar to the frequency found above T_c . The frequency decreases for decreasing temperature and the frequency eventually becomes smaller than the predicted value in the hydrodynamic limit, $\omega_s/\omega_{ax} = \sqrt{19/5}$.

In the density gradient of the BEC only damped oscillatory behavior is observed, with a frequency similar to the frequency of the standing wave sound mode, although higher order, fast damping modes are observed as well. We fit the density gradient to the combination of two damped sinusoidal functions and find two distinct frequencies and damping rates. Here, we focus on the mode with a frequency similar to the standing wave sound mode and determine its damping rate $\Gamma_{s,BEC}$ and oscillation frequency $\omega_{s,BEC}$ from a least-square fit. In Fig. 6.9 the normalized damping rate $\Gamma_{s,BEC}/\omega_{ax}$ and the normalized frequency $\omega_{s,BEC}/\omega_{ax}$ are shown as a function of the reduced temperature. We find damping rates and frequencies similar to the values of the thermal standing wave sound mode for all temperatures, although $\omega_{s,BEC}/\omega_{ax}$ increases for increasing temperature, where

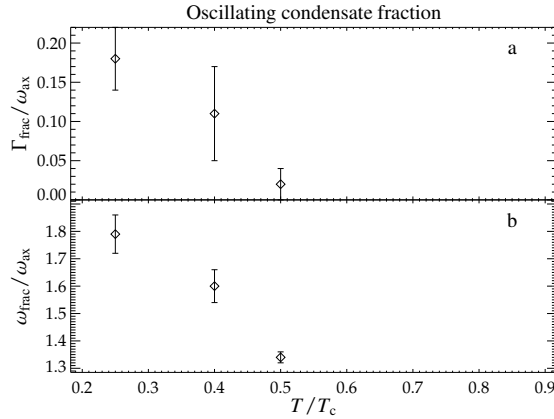


Figure 6.10: The normalized damping rate $\Gamma_{\text{frac}}/\omega_{\text{ax}}$ (Fig. a) and normalized frequency $\omega_{\text{frac}}/\omega_{\text{ax}}$ (Fig. b) of least-damped oscillation of the condensate fraction as a function of the reduced temperature T/T_c .

$\omega_{s,\text{ex}}/\omega_{\text{ax}}$ decreases for increasing temperature. Note that the frequency of the standing wave mode of both the thermal cloud and the BEC are approximately the same around $T/T_c \approx 0.5$ and that the damping rate of both modes strongly increases around this temperature, again indicating the interactions between both components influence the behavior of the modes significantly. Higher order modes observed in the density gradient of the condensate are most prominent at low temperatures (compare Figs. 6.3d and 6.4d) and multiple oscillations are observed. Since these oscillations have almost equal frequencies and damping rates the interpretation of the results at low temperatures is complicated.

6.3.3 Modes involving both components

The excitation procedure adds energy to the cloud. Initially, a local decrease of the condensate fraction is observed. The cloud will eventually equilibrate to the new temperature resulting in a decrease of the global condensate fraction. For high initial temperature the condensate fraction is found to gradually decrease as a function of τ , but for low temperatures the fraction increases again at $\tau \approx 150$ ms. For these temperatures we observe an oscillating decrease of the condensate fraction as can be seen in Fig. 6.10. We describe this oscillation for low temperatures with the combination of three damped sinusoids on a linear decreasing background and find three distinct damping rates and frequencies. At higher temperatures only a single oscillation is observed until the decrease becomes non-oscillatory at the highest temperatures. We focus on the mode

found at the temperature where only one oscillation is observed, and determine its damping rate Γ_{frac} and frequency ω_{frac} from the least-square fit. For lower temperatures, the mode with the smallest damping rate is taken. Fig. 6.10 shows the normalized damping rate $\Gamma_{\text{frac}}/\omega_{\text{ax}}$ and normalized frequency $\omega_{\text{frac}}/\omega_{\text{ax}}$ of the oscillating condensate fraction for the three lowest temperatures, since it is only observed at these temperatures. The oscillation of the condensate fraction is interpreted as the result of a thermal wave, which is strongly damped for high temperatures but its damping rate decreases for lower temperatures, making the observation of the mode possible. Unfortunately, we only observe the propagation of the thermal wave by its effect on the condensate fraction and not directly in the thermal cloud.

The final mode discussed here, the out-of-phase dipole oscillation, shows a slowly damped oscillation for $\tau > 0.5$ s. The damping rate Γ_{oop} and frequency ω_{oop} are determined with a least-square fit to a single damped sinusoid. The normalized damping rate $\Gamma_{\text{oop}}/\omega_{\text{ax}}$ and oscillation frequency $\omega_{\text{oop}}/\omega_{\text{ax}}$ of the out-of-phase dipole oscillation are shown in Fig. 6.11 as a function of the reduced temperature. For low temperatures the frequency of this mode is significantly below ω_{ax} and the motion is almost undamped. For higher temperatures the frequency and damping rate both increase. The damping rate of the out-of-phase dipole motion increases for increasing temperature, showing that interactions between the thermal cloud and BEC cause friction between both components and thereby damp its amplitude. There are only two other observations of the out-of-phase dipole mode reported. In the experiment reported in Ref. [85] the cloud is in the collisionless regime. In Ref. [13] an experiment is described in which the cloud is in the crossover region toward the hydrodynamic regime, and only the result for one experimental setting is reported. Nevertheless, in both studies the out-of-phase dipole oscillation is found to oscillate slower than the trap frequency; $\omega_{\text{oop}} \approx 0.95\omega_{\text{ax}}$. This frequency shift is ascribed to the interaction between the thermal cloud and the BEC. In our experiment we find $\omega_{\text{oop}} \approx 0.85\omega_{\text{ax}}$, indicating the interactions in our experiment are much stronger. The out-of-phase dipole motion is examined in more detail in Chapter 7, where an experiment is described in which mainly this mode is excited.

6.4 CONCLUSION & OUTLOOK

In conclusion, we have successfully excited a temperature wave in a BEC at finite temperature. Above the transition temperature the excitation of a thermal dipole mode already gives rise to a number of different modes. Below T_c , these modes are observed in the thermal cloud as well as in the BEC, doubling the number of excited modes, which makes it even harder to unravel the separate modes. Furthermore, the equivalent modes couple as a function of the temperature and as a consequence complicate the interpretation of the excited modes. Nevertheless,

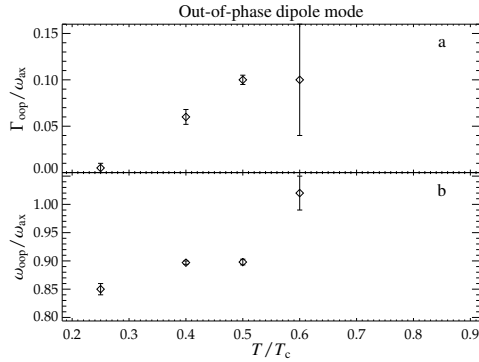


Figure 6.11: The normalized damping rate $\Gamma_{\text{oop}}/\omega_{\text{ax}}$ (Fig. a) and normalized frequency $\omega_{\text{oop}}/\omega_{\text{ax}}$ (Fig. b) of least-damped oscillation of the out-of-phase center of mass oscillation as a function of the reduced temperature T/T_c .

we succeeded in identifying seven distinct modes. We measured the damping rate and frequency of all of these modes as a function of the temperature.

The effects of interaction between the two components is observed in the shifted frequency of the quadrupole oscillations of both components and in the coupling around $T \approx 0.5T_c$ in the standing wave sound modes of both components. Direct observation of the interactions between both components is shown in the oscillating condensate fraction, which indicates the propagation of the excited thermal wave. This mode is only observed for $T \lesssim 0.5T_c$. Furthermore, an out-of-phase dipole oscillation between both components is observed and both the damping and frequency of this mode directly show the effect of mutual interactions.

In the absence of a theoretical description of the two-fluid system we cannot quantitatively compare the measured damping rates and frequencies to theory. The data presented here, showing the interactions between both components in the observed modes, can be used as a testing ground for the development of these theories and can deepen the understating underlying the interactions in the two-fluid regime.

THE SECOND SOUND DIPOLE MODE IN THE TWO-FLUID REGIME

Abstract

We study the second sound dipole mode in a partially Bose-Einstein condensed gas. This mode is excited by spatially separating and releasing the center-of-mass of the Bose-Einstein condensate (BEC) with respect to the thermal cloud, after which the equilibration is observed. The oscillation frequency and the damping rate of this mode is studied for different harmonic confinements and temperatures. The measured damping rates close to the collisionless regime are found to be in good agreement with Landau damping. For increasing hydrodynamicity of the cloud we observe an increase of the damping.

7.1 INTRODUCTION

In 1938 Kapitza, and independently Allen and Misener, discovered that liquid ^4He below the λ -point can flow almost frictionless. Kapitza named this behavior superfluidity [5, 6] and was awarded the Nobel prize for this discovery in 1978. Many of the properties of superfluid helium also appear in the gaseous Bose-Einstein condensates (BECs). In contrast to liquid helium, where the interatomic interaction is too strong to investigate the microscopic properties of superfluidity, the interactions in gaseous BECs are much weaker. The study of superfluid flow in dilute BECs can therefore deepen our understanding of superfluidity.

The observation of vortices in a gaseous BEC [86, 87] and the demonstration of the persistent flow of a BEC in a toroidal trap [88] give a striking demonstration of superfluidity. Evidence of the breakdown of superfluidity in a BEC is obtained in an experiment by the MIT group, in which a blue-detuned laser beam is moved through the BEC at different velocities [89]. Strong heating is observed only above a critical velocity v_c , which is found to be $v_c \simeq 0.25c$, with c the local speed of sound at the peak density of the condensate.

This chapter is based on a paper, which is submitted to Physical Review Letters as *Second sound dipole mode in a partially Bose-Einstein condensed gas*, R. Meppelink, S. B. Koller, J. M. Vogels, H. T. C. Stoof and P. van der Straten.

In this chapter the flow of a BEC through a thermal cloud in a harmonic potential is studied by exciting a dipole oscillation of the BEC, whereas the thermal cloud initially remains stationary. In the hydrodynamic regime this out-of-phase mode of the trapped Bose gas is the analog of the usual second sound mode in bulk superfluid helium [67]. For this second sound dipole mode we study for the first time its frequency and damping rate from the collisionless to the hydrodynamic regime. In contrast to liquid helium, our analysis allows for a direct measurement of the position of the superfluid component (condensed atoms) with respect to the normal fluid (thermal atoms), which allows for an unequivocal determination of the second sound dipole mode. A dipole oscillation of the center-of-mass of the whole system is undamped in a harmonic potential and this in-phase dipole oscillation is often used to measure the trap frequency.

The thermal cloud can also be tuned into the collisionless regime, in which the mean free path of the thermal atoms is larger than the axial size of the cloud. As we will show, the damping of collective excitations in a collisionless partly condensed BEC is primarily caused by Landau damping, i. e. mean-field interactions mediate the transfer of energy from the condensate to the thermal cloud, leading to the damping of collective modes. Landau damping was first discussed by Landau in the context of the damping of plasma oscillation and plays a key role in a broad variety of fields, for instance the damping of phonons in metals, the damping of quarks and gluons in quark-gluon plasmas and the anomalous skin effect in metals.

Previously, some experiments have been performed in which the BEC and the thermal cloud move with respect to each other and either the BEC [13] or the thermal cloud [85] is initially at rest. In the experiment presented in Ref. [85] the thermal cloud is in the collisionless regime. In a pioneering experiment presented in Ref. [13] the thermal cloud is in the crossover region toward the hydrodynamic regime, but only one measurement series is presented. It therefore does not provide a study of the dependence of the superfluid flow on for instance the temperature or the collision rate. In contrast, the number of theoretical studies of this subject greatly outnumbers the available experimental work [67, 71, 78, 90].

7.2 EXPERIMENT

The experimental setup, as described in detail in Chapter 2, is capable of creating Bose-Einstein condensates containing up to $3 \cdot 10^8$ sodium atoms, limited by three-body decay. In this setup we have reached the axially hydrodynamic regime in the thermal cloud above the transition temperature T_c . The axially hydrodynamic regime is reached by evaporatively cooling atoms in an axially strongly decompressed trap with an aspect ratio of up to 1 : 65 [36]. The radial trap frequency is given by $\omega_{\text{rad}}/(2\pi) = 95.56$ Hz. Here, we cool atoms to temperatures below T_c for three different values of the axial confinement.

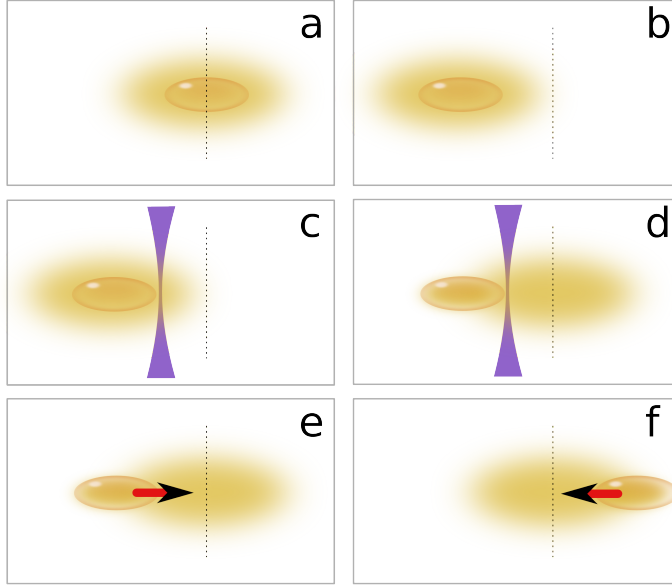


Figure 7.1: Schematic representation of the excitation procedure of the second sound dipole oscillation. See text for more details.

We introduce a measure for the hydrodynamicity of the thermal cloud in the axial direction $\tilde{\gamma} \equiv \gamma_{22}/\omega_{\text{ax}}$, where the collision rate $\gamma_{22} = \gamma_{\text{col}} = n_{\text{eff}} \sigma v_{\text{rel}}$ is the average number of collisions in the thermal cloud (see Chapter 5). Here, v_{rel} is the relative velocity, $\sigma = 8\pi a^2$ is the isotropic cross section of two bosons with s -wave scattering length a and $n_{\text{eff}} = \int d\mathbf{r} n_{\text{ex}}^2(\mathbf{r}) / \int d\mathbf{r} n_{\text{ex}}(\mathbf{r})$ is the effective density of the trapped thermal atoms with density n_{ex} . For our parameters, $\gamma_{22} \simeq 90 \text{ s}^{-1}$ for the highest number of atoms and weakest axial confinement, which corresponds to a hydrodynamicity of $\tilde{\gamma} \lesssim 10$. Note that the thermal cloud becomes less hydrodynamic for stronger axial confinement due to two effects: the increased three-body losses and the radial expansion. We have observed the crossover from the collisionless regime to the hydrodynamic regime by studying the quadrupole mode and heat conduction in a thermal cloud above T_c (see Chapters 4 and 5, respectively). Furthermore, in the study of the collective modes of clouds above and below T_c , presented in Chapter 4, we have experimentally substantiated the claim made in Ref. [71] that the thermal cloud is deeper in the hydrodynamic regime when a BEC forms due to collisions with condensed atoms. As a result the thermal cloud is even more hydrodynamic below T_c than it is above the transition temperature.

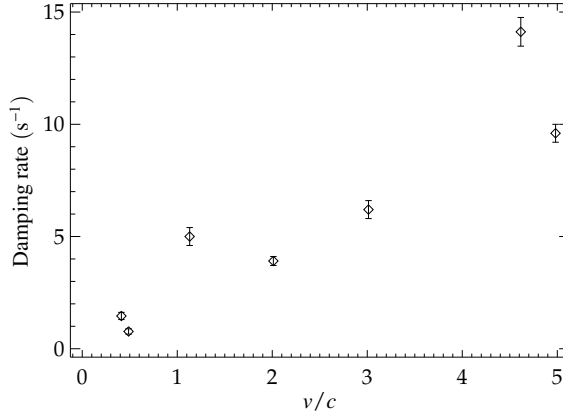


Figure 7.2: The damping rate of the out-of-phase oscillation as a function of the initial velocity v/c , where c is the central speed of sound determined using the measured BEC density. The uncertainty in the measured damping rate and in c is larger for high v due to the depletion of the condensate. The axial trap frequency is $\omega_{ax}/(2\pi) = 1.56$ Hz for all measurements.

The procedure used for the excitation of a second sound dipole mode, schematically shown in Fig. 7.1, is conducted as follows: initially, the center of the magnetic trap (MT) at $z = z_0$ (Fig. 7.1a) is displaced adiabatically in the axial direction over slightly more than the length of the BEC (Fig. 7.1b). Next, a focused blue-detuned laser beam is aligned perpendicular to the axial axis of the system at position z_d with $z_0 < z_d < z_1$, where it does not overlap with the BEC (Fig. 7.1c). This beam is detuned 25 nm below the ^{23}Na D_2 -transition and its intensity is gradually ramped up to roughly 10^4 mW/cm² in 100 ms. This corresponds to a maximum potential of roughly $V_{\text{dip}} \simeq 1.1 \times \mu$, where μ is the chemical potential of the initial cloud. The intensity is continuously measured using a photo diode in order to stabilize the intensity using a feed-back circuit controlling the efficiency of an acousto-optical modulator (AOM), which deflects the light used for the dipole beam. Next, the center of the trap is displaced adiabatically back to its original position $z = z_0$ (Fig. 7.1d). Since $\mu < V_{\text{dip}} < k_B T$, with k_B the Boltzmann constant and T the temperature, only the thermal cloud can pass the dipole potential and returns to $z = z_0$, while the condensate remains at $z = z_1$. Finally, the dipole beam is turned off and the BEC will undergo a dipole oscillation, while the thermal cloud is initially at rest (Figs. 7.1e and 7.1f). The distance $\Delta z = z_d - z_0$ determines the maximum velocity $v = \omega_{ax} \Delta z$ of the center-of-mass of the condensate. The final position of the center of the MT is used to tune Δz and thus v .

We have excited the cloud for various v in order to observe, if there is a threshold velocity v_c above which the out-of-phase oscillation is strongly damped. The damping rate for different values of v is shown in Fig. 7.2. For $v > c$ we observe an increase of the damping rate of the out-of-phase oscillation for increasing v . The strong damping in this regime is accompanied by a large reduction of the condensate fraction, which eventually leads to the complete depletion of the BEC. For smaller v (but still above v_c) we observe two distinct damping rates as long as the relative velocity is sufficiently reduced below v_c before the condensate is fully depleted: first we observe a high damping rate, but as soon as the relative velocity is below v_c a much lower damping rate is observed. For excitations with $v \lesssim v_c$ we observe a low damping rate, independent of v within the experimental accuracy. The threshold value depends on our trap geometry and is determined at $v_c/c \approx 0.59 \pm 0.05$ for the weakest axial confinement. For the strongest confinement used we find $v_c/c \approx 0.8 \pm 0.1$. The observation of a threshold velocity indicates the onset of a strong damping mechanism, which we consider as the breakdown of superfluidity. The experiments described in the remainder of this chapter are conducted in the regime of low damping ($v < v_c$).

A measurement series contains roughly 100 shots at various hold time τ after the dipole beam is suddenly turned off. At the end of the hold time an absorption image is taken after the cloud is allowed to expand during a 85 ms time-of-flight (TOF). During a measurement series the situation before the dipole beam is turned off is monitored a few times to check for the absence of condensed atoms in the center of the trap. The thermal cloud is easily distinguished from the BEC in the absorption images due to the distinct density profiles. The final images are fitted to a bimodal distribution. This distribution is the sum of a Maxwell-Bose distribution modeling the thermal cloud and a Thomas-Fermi (TF) distribution modeling the BEC. The fit yields ten parameters; the axial and radial positions, the axial and radial sizes and the optical densities of both components. The axial position of both components is used to observe the dipole oscillations, the total absorption is used to determine the column density of both components, and the radial size of the thermal cloud is used to determine the temperature of the system. Furthermore, the aspect ratio of the condensate is used to detect the quadrupole oscillation induced by the excitation procedure, which turns out to be small. This mode does not couple to the dipole mode and is therefore not of interest to us here.

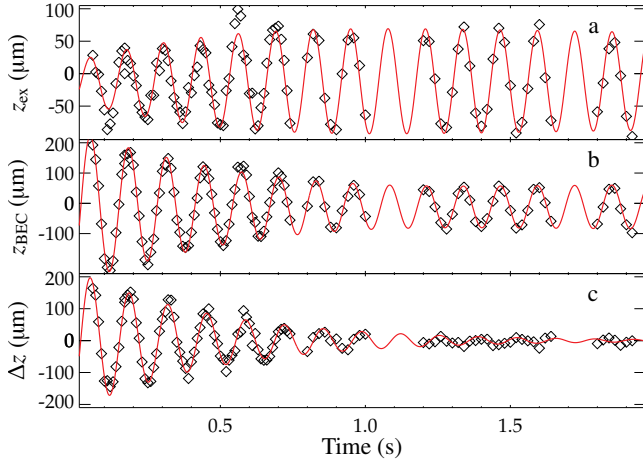


Figure 7.3: The in-phase and out-of-phase dipole oscillation of a system characterized by $T = 0.39 \mu\text{K}$ and $\mu/h = 2.6 \text{ kHz}$ for $\omega_{\text{ax}}/(2\pi) = 7.78 \text{ Hz}$. In Figs. a and b the axial position z_{ex} of the thermal cloud and z_{BEC} of the BEC is plotted as a function of the hold time τ . In Fig. c the motion of the out-of-phase dipole oscillation is isolated by plotting $\Delta z = z_{\text{BEC}} - z_{\text{ex}}$ as a function of τ . The solid lines are the result of a fit to Eq. (7.1).

7.3 RESULTS & DISCUSSION

A series is measured for three different values of the axial confinement and for two different temperatures. To compare the results under these different conditions, the temperature is adjusted in such a way that for a given temperature the initial chemical potential is roughly the same in all confinements. Note that due to the large three-body losses for strong confinement, the number of atoms is smaller in that case and thus the thermal cloud becomes less hydrodynamic. The distance $z_{\text{d}} - z_0$ is adjusted for each confinement to ensure $v < v_{\text{c}}$. The axial position of the thermal cloud z_{ex} and the BEC z_{BEC} are plotted as a function of τ in Figs. 7.3 and 7.4 for different values of the axial confinement. Furthermore, the difference $\Delta z = z_{\text{BEC}} - z_{\text{ex}}$ is plotted to isolate the out-of-phase dipole oscillation from the in-phase oscillation. The thermal cloud, initially at rest, starts to oscillate when the BEC moves through it and eventually both the BEC and the thermal cloud oscillate simultaneously and in-phase, as can be seen in Figs. 7.3 and 7.4. We refer to this final motion as the in-phase dipole oscillation. We have checked that the thermal cloud remains at rest as long as the dipole beam is present.

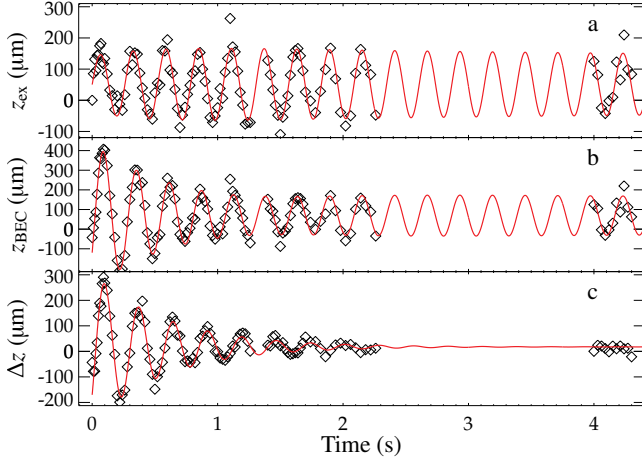


Figure 7.4: The in-phase and out-of-phase dipole oscillation of a cloud, characterized by $T = 0.46 \mu\text{K}$ and $\mu/h = 3.0 \text{ kHz}$, for $\omega_{\text{ax}}/(2\pi) = 3.91 \text{ Hz}$. For the description refer to the caption of Fig. 7.3.

The positions z_{ex} and z_{BEC} are simultaneously fitted to a combination of two exponentially damped sinusoidal functions, where the function describing the in-phase (out-of-phase) oscillation is denoted by $Z_{\text{ip}}(t)$ ($Z_{\text{oop}}(t)$) resulting in

$$\begin{aligned} z_{\text{ex}}(t) &= Z_{\text{ip}}(t) - \mathcal{F} Z_{\text{oop}}(t), \\ z_{\text{BEC}}(t) &= Z_{\text{ip}}(t) + (1 - \mathcal{F})Z_{\text{oop}}(t). \end{aligned} \quad (7.1)$$

Here \mathcal{F} is the condensate fraction. The fit of the data to Eq. (7.1) yields the damping rate Γ_{ip} (Γ_{oop}) and the frequency ω_{ip} (ω_{oop}) of the in-phase (out-of-phase) dipole oscillation. The damping rate of the in-phase dipole oscillation does not deviate from zero within the experimental uncertainty, as is expected for a harmonic trap. The axial trap frequency determined from the in-phase oscillation frequency gives the same result as the trap frequency determination from a mutual center-of-mass oscillation ($\omega_{\text{ip}} = \omega_{\text{ax}}$). The quantities Γ_{oop} and ω_{oop} are plotted as a function of the trap frequency and the temperature in Figs. 7.5 and 7.6, respectively. Furthermore, the results are tabulated in Table 7.1.

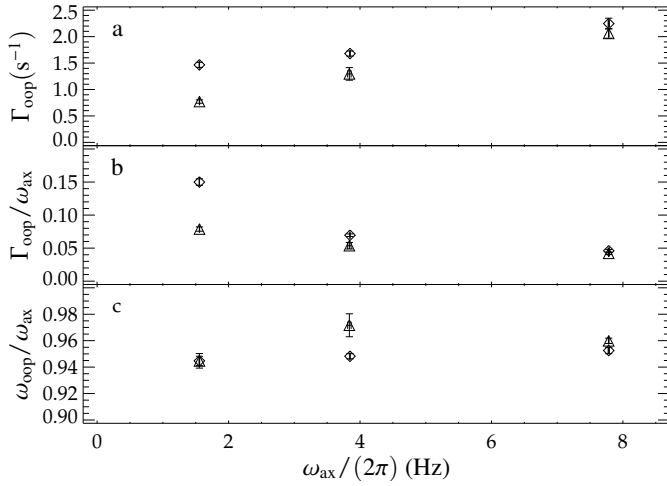


Figure 7.5: The damping rate Γ_{ooop} (Fig. a), the normalized damping rate $\Gamma_{\text{ooop}}/\omega_{\text{ax}}$ (Fig. b), and the normalized oscillation frequency $\omega_{\text{ooop}}/\omega_{\text{ax}}$ (Fig. c) as a function of the axial trap frequency $\omega_{\text{ax}}/(2\pi)$. The diamonds (triangles) indicates the high (low) temperature condition.

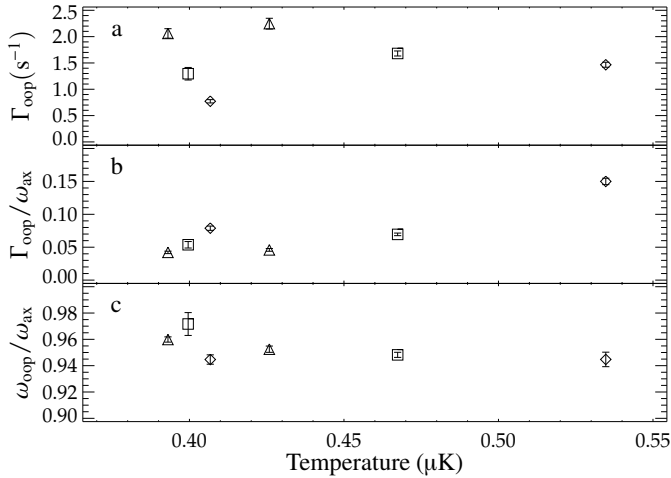


Figure 7.6: The damping rate Γ_{ooop} (Fig. a), the normalized damping rate $\Gamma_{\text{ooop}}/\omega_{\text{ax}}$ (Fig. b), and the normalized oscillation frequency $\omega_{\text{ooop}}/\omega_{\text{ax}}$ (Fig. c) as a function of the temperature T , determined from the radial expansion of the thermal cloud. The diamonds, squares, and triangles correspond to measurements in the axial confinement given by 1.56 Hz, 3.85 Hz and 7.78 Hz, respectively.

#	$\frac{\mu}{h}$ (kHz)	T (μ K)	N_c (10^6)	N_{ex} (10^6)	$\frac{\omega_{\text{ax}}}{2\pi}$ (Hz)	$\tilde{\gamma}$	$\frac{\omega_{\text{oop}}}{2\pi}$ (Hz)	Γ_{oop} (s^{-1})	$\Gamma_{\text{oop}}/\Gamma_L$
1	2.8	0.53	80	450	1.56	8.5	1.47 (1)	1.47 (5)	1.72
2	3.1	0.41	100	200	1.56	4.9	1.47 (1)	0.77 (3)	1.18
3	2.7	0.39	15	80	7.78	2.1	7.47 (2)	2.06 (9)	1.15
4	2.8	0.43	20	120	7.78	2.8	7.41 (2)	2.25 (10)	1.15
5	2.7	0.4	30	70	3.84	1.8	3.73 (3)	1.30 (12)	1.10
6	3.1	0.46	30	250	3.85	5.5	3.65 (1)	1.68 (5)	1.29
7	5.2	0.3	145	180	3.89	6.0	3.86 (1)	1.22 (6)	1.46
8	3.9	0.3	180	100	1.58	3.3	1.58 (1)	0.51 (4)	1.2

Table 7.1: Results of the out-of-phase dipole oscillation measurements. The oscillation frequency ω_{oop} and damping rate Γ_{oop} of the out-of-phase dipole mode are given, as well as the corresponding chemical potential μ , temperature T , number of condensed atoms N_c , and number of thermal atoms N_{ex} . The hydrodynamicity for mutual collisions in the thermal cloud $\tilde{\gamma}$ and the Landau damping rate Γ_L (see Eq. (7.3)) is given as well. The radial trap frequencies are $\omega_{\text{rad}}/(2\pi) = 95.56$ Hz for all experiments. The first six series are shown in Figs. 7.5 and 7.6.

In Fig. 7.5a one can see that Γ_{oop} decreases for decreasing axial trap frequency. However, $\Gamma_{\text{oop}}/\omega_{\text{ax}}$ increases for decreasing axial trap frequency as one can see in Fig. 7.5b. This indicates that an extra damping mechanism, which does not depend on the trap frequency, plays a significant role as well, especially for the highest T (see Fig. 7.6) and thus the most hydrodynamic clouds.

The normalized second sound oscillation frequency $\omega_{\text{oop}}/\omega_{\text{ax}}$ is shown in Fig. 7.5c. For all conditions $\omega_{\text{oop}} < \omega_{\text{ax}}$, where under the most hydrodynamic conditions $\omega_{\text{oop}} \approx 0.94\omega_{\text{ax}}$. Furthermore, the largest deviations of $\omega_{\text{oop}}/\omega_{\text{ax}}$ from 1 coincides with the largest Γ_{oop} and is found for the most hydrodynamic clouds. The shift of ω_{oop} with respect to ω_{ax} , up to 6% in our experiment, is larger than the shift of 4.5% observed in Ref. [13] and similar to the 6% shift reported in Ref. [85], although the reduced temperature T/T_c is lower in our experiments.

The mean-field potential of the thermal cloud causes the effective axial trapping potential to be slightly smaller. This effect reduces the effective trap frequency with roughly 2% for the highest thermal density in these experiments and cannot account for the shifts of up to 6%. As a consequence, the measured frequency shift and damping rate of the out-of-phase dipole mode both reflect that collisional effects play a role. Since ω_{oop} and ω_{ax} are determined simultaneously and with a high accuracy the frequency shift gives an accurate measure for these effects.

The measured damping rates are compared in Fig. 7.7 to Landau damping. Landau damping in a homogeneous, weakly interacting Bose gas has been described in the collisionless limit by several authors [91, 92]. Landau damping increases with temperature, because of the larger number of particle-hole pairs available at thermal equilibrium [76]. The damping rate for a homogeneous gas is given by [76]

$$\Gamma_{\text{Lh}} = \frac{3\pi k_{\text{B}} T a \omega}{8 \hbar c}, \quad (7.2)$$

where the speed of sound is given by $c = \sqrt{\mu/m}$, with m the atomic mass. Furthermore, ω is the frequency of the excitation. Note that in our experiment Γ_{Lh} is roughly independent of the speed of sound, since μ and therefore the central density is roughly constant in the different axial confinements.

In our case, due to the confinement both the BEC and the thermal cloud have an inhomogeneous density distribution. Landau damping in such a system is determined by the condensate boundary region, and the result for the damping rate is different from that in a spatially homogeneous gas [93–95]. Using the result from Ref. [95], we find for the Landau damping rate for an inhomogeneous cloud

$$\Gamma_{\text{L}} = \frac{12c m}{\pi^{3/2} k_{\text{B}} \sqrt{m \hbar \omega} \log [2c^2 m / (\hbar \omega)]} \Gamma_{\text{Lh}}. \quad (7.3)$$

Fig. 7.7 shows that we have measured the damping rate of the second sound dipole mode in a range from close to the collisionless regime up to the hydro-

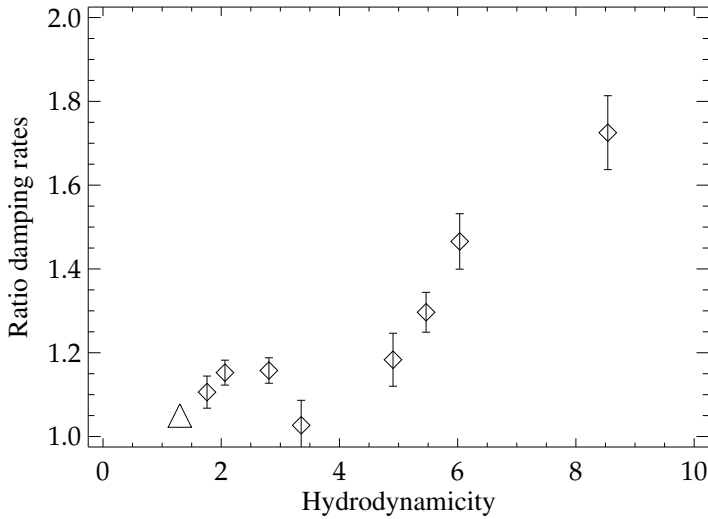


Figure 7.7: The ratio of the measured damping rate and Landau damping $\Gamma_{\text{ooP}}/\Gamma_L$ as a function of the hydrodynamicity parameter $\tilde{\gamma}$. The data point represented by the triangle is the result of a measurement taken from Ref. [13]. The main contribution to the uncertainties is the estimated error in the measured chemical potential.

dynamic regime with a hydrodynamicity close to 10. Close to the collisionless regime we find the measured damping rates show good agreement to Landau damping if we take the inhomogeneous density into account. The ratio $\Gamma_{\text{ooP}}/\Gamma_L$ increases strongly as a function of the hydrodynamicity $\tilde{\gamma}$ and this may serve as a stringent test for theoretical models, which attempt to describe the damping of hydrodynamic excitations in the Landau two-fluid (normal and superfluid) model. It shows that collisional processes, which have not been incorporated in the descriptions of Landau damping discussed above, play an important role in damping the second sound dipole mode.

7.4 CONCLUSION

In conclusion, we successfully excited an out-of-phase dipole mode in a trapped Bose-Einstein condensed gas at finite temperature. In the hydrodynamic regime this out-of-phase mode of the trapped Bose gas is the analog of the usual second sound mode in bulk superfluid helium. We have shown that interactions between a moving BEC and a static thermal cloud cause the thermal cloud to move as well, eventually damping the out-of-phase oscillation. The in-phase oscillation

remains undamped. The damping rate and the oscillation frequency of the second sound dipole mode is measured as a function of the axial confinement and the temperature with a high accuracy. We find that Landau damping, when the inhomogeneous density of the cloud is taken into account, shows good agreement to the measured damping rates close to the collisionless regime. In the hydrodynamic regime the measured damping rates are larger than the rates based on Landau damping. The observed shift the frequency, as large as 6 % of the oscillation with respect to the trap frequency cannot be accounted for by the mean-field potential of the thermal cloud for the most hydrodynamic thermal clouds.

We hope that the measurements presented here encourages calculations based on models that take collisional damping into account and can provide a fruitful testing ground for such models.

SOUND PROPAGATION IN THE TWO-FLUID REGIME

Abstract

We study the propagation of a density wave in a magnetically trapped Bose-Einstein condensate at finite temperature. The thermal cloud is in the hydrodynamic regime and the system is therefore described by the two-fluid model. A phase contrast imaging technique is used to image the cloud of atoms and allows us to observe small density excitations. The propagation of the density wave in the condensate is used to determine the speed of sound as a function of the temperature. We find the speed of sound to be in good agreement with calculations based on the Landau two-fluid model.

8.1 INTRODUCTION

Long wavelength excitations of a Bose-Einstein condensate (BEC) with repulsive interactions exhibit a phononlike, linear dispersion, causing these excitations to move at a finite speed c , the speed of sound. Excitations with a wavelength comparable to the size of the cloud result in collective shape oscillations of the system and these excitations are studied in Chapter 4. The dispersion relation is linear up to wave vectors of the order of the inverse of the healing length. Perturbations with a wavelength much shorter than the axial size of the cloud and larger than the healing length therefore give rise to the excitation of a hydrodynamic mode propagating at the speed of sound.

In the case of liquid helium sound excitations have been extensively studied below the λ -point, where a superfluid and a normal fluid coexist. In this regime two sound modes can be distinguished: the first mode, first sound, consists of an in-phase oscillation of the superfluid and normal fluid component, while the second mode, second sound, consists of an out-of-phase oscillation of the superfluid and normal fluid component. The occurrence of two distinct modes is caused by the presence of both a superfluid density and normal fluid density, which are coupled. One of the drawbacks of liquid helium is that the interactions

This chapter is based on a paper, which is accepted for publication in Physical Review A as *Sound propagation in a Bose-Einstein condensate at finite temperatures*, R. Meppelink, S. B. Koller and P. van der Straten

are so strong that a clear distinction between the two components is difficult which complicates the interpretation of the phenomena.

In the dilute gaseous BEC studied here a two-fluid system exists below T_c , analogous to the case of liquid helium. In our setup the thermal cloud is in the hydrodynamic regime, where collisions between atoms are rapid enough to establish a state of dynamic local equilibrium in the thermal cloud. In contrast to Bose-condensed liquid helium, the superfluid in the gaseous BEC corresponds directly to the Bose-Einstein condensed atoms and the normal component directly to the thermal, non-condensed atoms, since the interactions are much weaker.

First and second sound in a Bose gas exhibit different features than those in a Bose liquid [96]. In liquid helium, the coupling between the density and temperature is weak, since $C_p \simeq C_v$, with $C_{p,v}$ the specific heat at constant pressure and constant volume, respectively. As a result, in liquid helium first sound is mainly a density wave, while second sound is an almost pure temperature wave. In contrast, in a Bose gas the density and temperature fluctuations are strongly coupled, since $C_p/C_v \neq 1$. The first sound mode in a Bose gas is largely an oscillation of the density of the thermal cloud (the normal fluid) and second sound is largely an oscillation of the density of the condensate (the superfluid) [97]. In superfluid helium, only the first sound mode can be excited by a density perturbation. In contrast, second sound has a significant weight in the density response function in superfluid Bose gases at finite temperatures and can be excited by a local perturbation of the density.

Since we can directly image BECs and make a clear distinction between both components, it allows for a direct comparison with theoretical descriptions of the two-fluid system modeling the interactions between both components. Thus the research using weakly interacting Bose gases promises results that will go beyond the results obtained using liquid helium.

In a pioneering paper by Lee and Yang the speed of first and second sound is derived for a dilute Bose gas, although there is no coupling between both sound modes [98]. This interaction is taken into account in the two-fluid model developed by Landau for liquid helium [99] and in a hydrodynamic model developed by Zaremba, Griffin, and Nikuni for trapped Bose gases [67]. In these papers it is shown that the hydrodynamic second sound mode at finite temperature extrapolates to the $T = 0$ Bogoliubov phonon mode.

The propagation of sound in a harmonically trapped, almost pure BEC in the collisionless regime has been observed experimentally in a pioneering experiment by the MIT group [44, 100] and studied theoretically by various authors [78, 98, 99, 101–103]. After the first experiment, sound propagation has been observed for a BEC in an optical lattice, the excitation spectrum of a BEC has been measured and the excitation of shock waves is observed [104–106].

The work presented here describes the experimental observation of a propagating sound wave in an elongated BEC at finite temperature and extends the study

by the MIT group in two ways. First, in the work presented here the propagation of a sound wave is observed at finite temperature. The thermal cloud is in the hydrodynamic regime above T_c and the cloud is therefore a two-fluid system below T_c : a superfluid BEC coexists with a normal fluid of thermal atoms. If the thermal cloud is already close to the hydrodynamic regime above T_c , it will be deeply in the hydrodynamic regime when the BEC forms, since the collision rate γ is dominated by the collisions between the condensed and the thermal atoms determined by the rate γ_{12} [71]. In the two-fluid system interactions between the superfluid and the normal component are expected to play an important role. Second, the high signal-to-noise ratio of our imaging technique allows us to make smaller excitations than is used in the MIT experiments, thereby limiting nonlinear effects. The large atom number BECs in combination with the weak axial confinement results in typical axial BEC lengths of more than 2 mm. This allows for the determination of the speed of sound with a high accuracy, since the propagation distance can be large before the sound wave reaches the edge of the BEC.

8.2 SOUND PROPAGATION IN A DILUTE BOSE-EINSTEIN CONDENSED GAS

Since second sound at finite temperature extrapolates to the $T = 0$ Bogoliubov phonon mode, we start this discussion in the $T = 0$ limit. The speed of second sound in the absence of a thermal cloud can be derived using the Gross-Pitaevskii equation (GPE). Reformulated as a pair of hydrodynamic equations, neglecting the quantum pressure and after linearization, the GPE can be written in the simplified, hydrodynamic form [103]

$$\frac{\partial^2 \delta n}{\partial t^2} = \nabla \left(c^2(\mathbf{r}) \nabla \delta n \right), \quad (8.1)$$

where the departure of the density from its equilibrium density n_{eq} is given by $\delta n(\mathbf{r}, t) = n(\mathbf{r}, t) - n_{\text{eq}}(\mathbf{r})$ and the local speed of sound $c(\mathbf{r})$ is defined by

$$mc^2(\mathbf{r}) = \mu - V_{\text{ext}}(\mathbf{r}), \quad (8.2)$$

where μ is the chemical potential, V_{ext} is the external confinement and m is the mass. In a uniform Bose gas, $V_{\text{ext}} = 0$, the speed of second sound is given by $c = \sqrt{\mu/m} = \sqrt{U_0 n_c/m}$, with n_c the condensate density and U_0 the interaction parameter. This result was first derived by Lee and Yang [98] based on theory developed by Bogoliubov [107] and is therefore often referred to as the Bogoliubov speed of sound, which we will refer to as c_B in this chapter. c_B only depends on temperature through the BEC density and is independent of the thermal density.

The experiments are conducted in an elongated 3D trap where the external confinement in the radial (subscript rad) and axial (subscript ax) direction is given by

$$V_{\text{ext}}(x, y, z) = \frac{1}{2}m \left(\omega_{\text{rad}}^2 x^2 + \omega_{\text{rad}}^2 y^2 + \omega_{\text{ax}}^2 z^2 \right), \quad (8.3)$$

with $\omega_{\text{rad}} \gg \omega_{\text{ax}}$, and the density depends on the position. Although the confinement is highly anisotropic, the BEC is not fully in the 1D regime, since $\mu \gg \hbar\omega_{\text{rad}}$. For the radial average density we use the Thomas-Fermi (TF) value $\bar{n}(z) = n(0, 0, z)/2$, where $n(0, 0, z)$ is the central axial density. The local Bogoliubov speed of sound is given in terms of the radial average density by

$$c_{\text{B}}(z) = \sqrt{\frac{U_0 \bar{n}(z)}{m}} = \sqrt{\frac{U_0 n(0, 0, z)}{2m}}, \quad (8.4)$$

a result confirmed using different methods [100–103]. In our experiment the axial confinement is weak and the density varies slowly along the axial direction.

To our knowledge two theoretical descriptions are available in which the effect of the interaction between the normal and the superfluid component on the speed of sound is taken into account. Zaremba, Griffin, and Nikuni have derived the two-fluid hydrodynamic equations for weakly interacting Bose gases [67] and use them to discuss first and second sound for a uniform Bose gas [108]. We refer to this description as the ZGN model. In the same paper, they derive the Landau two-fluid equations for a dilute gas in a complete local equilibrium and use these equations to calculate the first and second sound velocities. We refer to this description as the Landau model. In Ref. [78] it is shown the ZGN model is valid in the limit in which collisions between the condensed and the thermal atoms are ignored on the timescale of the collective excitation $\gamma_{\mu}/\omega \rightarrow 0$. The Landau model developed for dense fluids such as superfluid helium is valid for dilute Bose gases in the opposite limit of complete local equilibrium $\gamma_{\mu}/\omega \rightarrow \infty$ [78]. Here, γ_{μ} is the relaxation rate for chemical potential differences between the condensate and the thermal cloud as given in Ref. [78] and ω is the excitation frequency.

We introduce a measure for the hydrodynamicity of the thermal cloud in the axial direction $\bar{\gamma} \equiv \gamma_{22}/\omega_{\text{ax}}$, where the collision rate $\gamma_{22} = \gamma_{\text{col}} = n_{\text{eff}}\sigma v_{\text{rel}}$ is the average number of collisions in the thermal cloud. Here, the relative velocity $v_{\text{rel}} = \sqrt{2\bar{v}_{\text{ex}}}$, where $\bar{v}_{\text{ex}} = \sqrt{8k_{\text{B}}T/m\pi}$ is the thermal velocity at temperature T and m is the mass and $\sigma = 8\pi a^2$ is the isotropic cross section of two bosons with s -wave scattering length a . Furthermore, $n_{\text{eff}} = \int n_{\text{ex}}^2(\mathbf{r}) dV / \int n(\mathbf{r}) dV = n0_{\text{ex}}/\sqrt{8}$ for an equilibrium distribution in a harmonic potential, where $n0_{\text{ex}}$ is the peak density. Written in terms of the number of thermal atoms $N_{\text{ex}} = n0_{\text{ex}}(2\pi k_{\text{B}}T/(m\bar{\omega}^2))^{3/2}$ and the geometric mean of the angular trap frequencies $\bar{\omega}^3 \equiv \omega_{\text{rad}}^2 \omega_{\text{ax}}$, this results in $\gamma_{22} = N_{\text{ex}}m\sigma\bar{\omega}^3/(2\pi^2 k_{\text{B}}T) \approx 90 \text{ s}^{-1}$ for the highest

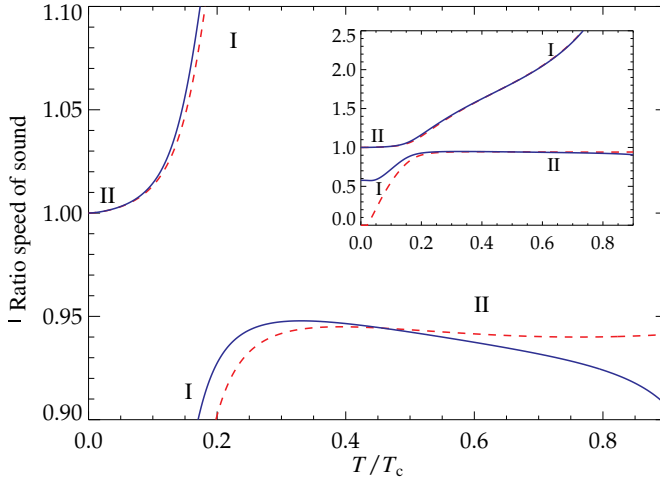


Figure 8.1: The speed of first (I) and second (II) sound calculated in the Landau model (solid lines) and the ZGN model (dashed lines), normalized to c_B (Eq. (8.4)) as a function of the reduced temperature T/T_c . The inset shows the same temperature range on a larger vertical scale. The densities and temperature used for the calculations for $0.2 < T/T_c < 0.9$ correspond to the interpolated experimental values. For $T/T_c < 0.2$ n_c is kept constant, and n_{ex} is extrapolated to $n_{\text{ex}} = 0$ for $T = 0$.

number of atoms and corresponds to a hydrodynamicity of $\bar{\gamma} \lesssim 10$ in the axial direction. We have observed the crossover from the collisionless regime to the hydrodynamic regime by studying a thermal dipole mode above T_c (see Chapter 5). Furthermore, it is noted in Ref. [71] that the thermal cloud is deeper in the hydrodynamic regime when a BEC forms due to collisions with condensed atoms. As a result, the thermal cloud is even more hydrodynamic below T_c than it is above the transition temperature.

Both models are used to calculate the speed of first and second sound as solutions of an equation of the form $u^4 - Au^2 + B = 0$, where A and B are coefficients which are given for both models in Ref. [78]. These coefficients depend on the condensate density n_c , the thermal density n_{ex} and the temperature T . In Ref. [78] the differences between both models for constant density $n = n_c + n_{\text{ex}}$ are found to be very small in the case of a weakly interacting Bose gas. As a result, the transfer of atoms required to equilibrate the condensed and thermal atoms is found to play a minor role in the determination of the speed of first and second sound [108].

The speed of first and second sound for both models is shown in Fig. 8.1, where close to T_c the first (second) sound mode mainly corresponds to the density wave

in the thermal (condensed) fraction. The figure shows the coupling between both sound modes cause the speed of second sound to be smaller than the Bogoliubov speed of sound. Around $T = 0.15T_c$ this coupling results in an avoided crossing. Note that the position of the avoided crossing in Fig. 8.1 is outside the region of validity of the model, which is valid for $k_B T \gg \mu$ [78].

8.3 EXPERIMENT

The experimental setup used to create large number BECs is described in Chapter 2. In short, ^{23}Na atoms are cooled and trapped in a dark-spot MOT and transferred to a magnetic trap (MT) after being spin-polarized [34]. Forced evaporative cooling on these atoms yields roughly $1 \cdot 10^9$ thermal atoms around $T = T_c$. In order to prevent three-body losses which limit the density as well as to increase the collision rate with respect to the axial trap frequency, we work with axially decompressed traps [36]. The resulting elongated, cigar-shaped clouds used for the experiments described here have an aspect ratio $\omega_{\text{rad}}/\omega_{\text{ax}} \approx 65$.

The experiments are conducted on clouds at various temperatures below T_c . The number of condensed atoms, slightly depending on the temperature, is roughly $N_c = 1.7 \cdot 10^8$ and the BEC density is about $2.5 \cdot 10^{20} \text{ m}^{-3}$. At the lowest temperatures, the BEC has a radial TF radius of μ roughly $22 \mu\text{m}$ and an axial TF radius of 1.4 mm .

The clouds are imaged using phase contrast imaging, the details of which are described in Chapter 3. Briefly, the atoms are imaged *in situ* and in contrast to other implementations of the phase contrast imaging technique [43], our implementation does not aim at nondestructive imaging, but uses the periodicity of the intensity of the phase contrast imaging technique as a function of the accumulated phase of a probe beam that propagates through a cloud of atoms. Therefore, the intensity signal for large enough accumulated phase show rings in the intensity profile. The number of rings is a sensitive measure for the atomic density and allows us to determine the BEC density, the thermal density and the temperature within a few percent. The lens setup used results in a diffraction limited resolution of roughly $4 \mu\text{m}$.

For the experiments we evaporatively cool the atoms in the presence of a blue-detuned focused laser beam aimed at the center of the trap, which acts as a repulsive optical dipole trap. The beam is focused using a cylindrical lens yielding a sheet of light with a $(1/e)$ -width of the intensity of $127 \pm 20 \mu\text{m}$. The non-focused direction has a $(1/e)$ -width of roughly 5 mm . The light of the dipole beam is detuned 20 nm below the ^{23}Na D_2 transition and the power adjusted in such a way that the repulsive potential has a height of $(0.24 \pm 0.04) \mu$, where μ is the chemical potential. Due to the large detuning heating caused by light scattering is negligible. The laser power of the dipole beam is continuously measured and used in an electronic feedback circuit controlling the efficiency of

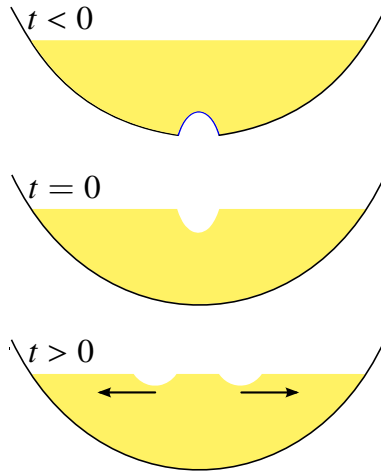


Figure 8.2: Schematic representation of the excitation of a sound wave, where the trapping potential, height and width of the perturbation are roughly on scale. At $t < 0$ a BEC is formed in the presence of a blue-detuned repulsive dipole beam which adjusts the trapping potential. At $t = 0$ the dipole beam is suddenly turned off and the inflicted density perturbation causes two density dips to move outward for $t > 0$, propagating at the speed of sound.

the acousto-optical modulator (AOM) that deflects laser light into an optical fiber whose output is used for the dipole beam. Using this procedure the stabilized intensity has a RMS fluctuation of 0.1%. Typically, the power is adjusted on the order of milliseconds and the power is therefore not stabilized instantaneously, mainly due to heating of the optical fibers. However, the height of the potential is not critical during the first stages of the evaporation (tens of seconds), where the thermal energy $k_B T$ is large compared to the dipole potential, ensuring the stability of the height of the potential long before the BEC is formed. An alternative way of exciting a sound wave is by turning on the repulsive potential after the BEC is formed. Since this procedure is immediately sensitive to the height of the potential this alternative results in less reproducible excitations than the procedure used in our experiments. Turning the dipole beam suddenly off ($(1/e)$ -time ~ 250 ns) causes a local dip of the BEC density. This perturbation splits up in two waves propagating symmetrically outward, both with half the amplitude of the initial perturbation. A schematic representation of the excitation procedure is shown in Fig. 8.2.

Clouds are imaged at about ten different times after the dipole beam is switched off, where for each shot a new cloud is prepared, since the imaging scheme used is destructive. The initial conditions of the newly prepared clouds show only

a small variation, since the density in the final stage of the evaporative cooling process is limited by three-body losses. The density as a function of the axial position is determined by making 1D fits of the radial profile for all axial positions. The fit function used is a bimodal distribution which is the sum of a Maxwell-Bose distribution describing the thermal cloud and a TF distribution describing the BEC. Each propagation time for a series is mostly measured twice. The total accumulated phase as well as the radial width of the BEC can be used as a measure for the local density, although the width is expected to yield inferior results due to lensing effects and the limited resolution in the radial direction.

8.4 RESULTS & DISCUSSION

The resulting axial density profiles of the condensate, shown in Fig. 8.3 for various propagation times, clearly shows the outward traveling density dips. In the density profiles of the thermal cloud these dips are absent, and no propagation is observed. The propagation of sound in the thermal cloud is discussed at the end of this section and for now we consider only the density perturbation of the condensed fraction of the cloud.

In the density profiles shown in Fig. 8.3 one can see that the shape of the perturbation, which is initially approximately Gaussian, deforms during the propagation. The deformation is caused by the dependence of the speed of sound on the density and its effect will be estimated using Eq. (8.4). The estimated change of the sound velocity corresponding to a change in density Δn is approximated by $\Delta c = (c/2)\Delta n/n$. The dependence of the sound velocity on the density causes the center of the dip to move slower than the edges. Furthermore, this effects results in the trailing edge to 'overtake' the center, while the leading edge outruns the center part. The resulting high density gradient leads to the formation of shock waves when the density gradient is of the order of $1/\zeta$, where ζ is the healing length [106]. Formation of shock waves complicates the propagation due to strong nonlinear behavior. The typical time for the formation of shock waves is estimated by considering the difference in traveled distance Δz of the tailing edge (density n) with respect to the center (density $n - \Delta n$) after τ propagation time, yielding $\Delta z \approx -(c\tau/2)\Delta n/n$ [102]. The edge will reach the center when $\Delta z \sim \sigma$, where σ is the width of the perturbation, resulting in $\tau \gtrsim \sigma n/(\Delta n c)$ which is the time for shock waves to form. For our typical parameters this yields $\tau \gtrsim 200$ ms. In the experiments propagation times are less than 110 ms.

8.4.1 Computer simulations

For times less than τ we already see that the propagating wave deforms. We have made a simulation of the Gross-Pitaevskii (GPE) equation which describes the BEC at $T = 0$ to analyze the effect the deformation has on the propagation of the

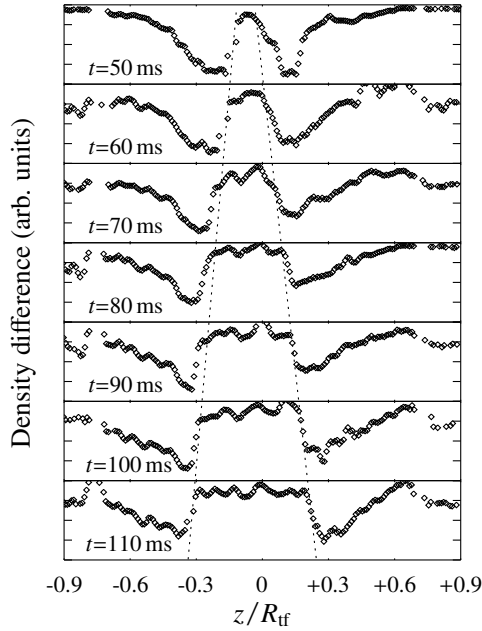


Figure 8.3: Density profiles showing the peak density of the BEC as a function of the axial position for seven different propagation times. The unperturbed density profile is subtracted from perturbed ones to increase the visibility of the density dips. The dotted line is a guide to the eye following the trailing edge of the dip. The horizontal scale is given in terms of the axial TF radius $R_{\text{tf}} \simeq 1.4$ mm.

condensate density wave. The GPE is numerically solved using the time-splitting spectral method described in Ref. [73]. Since the experiments are done on very elongated, cigar-shaped BECs and all effects are found in the axial directions, the calculation time can be reduced by solving an effective 1D equation in the limit of strong coupling [74]. Many experiments on both the statics and dynamics of BECs have shown that experiments can be modeled accurately by numerically solving the GPE, for example in experiments on interferometry [75] and superfluidity [76]. Note that we assume that the temperature dependence on the deformation of the condensate density wave can be neglected.

The simulated density profiles are shown in Fig. 8.4, where the perturbation is excited by growing the BEC in the presence of an additional Gaussian shaped potential. At $t = 0$ this extra potential is suddenly switched off, but the harmonic confinement remains. Two situations are shown; a small initial perturbation and a perturbation corresponding to the situation in the experiments. The simulations show the deformation of the initial shape of the perturbation and the steepening

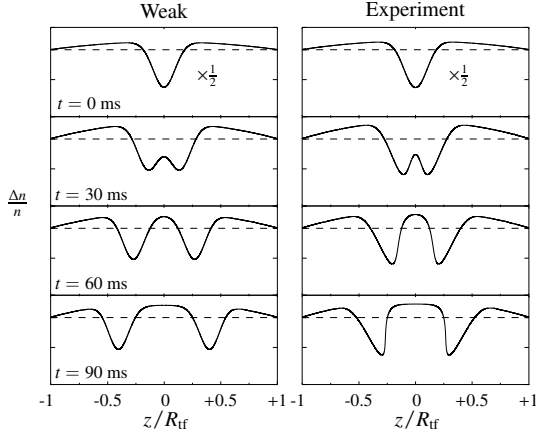


Figure 8.4: Simulation of the normalized density profiles $\Delta n/n$ along the axial axis in terms of the axial TF radius R_{tf} for different times t after the sound wave is excited. The left column corresponds to a weak perturbation $\Delta n/n = 10^{-4}$, the right column corresponds to the perturbation applied in the experiment, $\Delta n/n = 0.25$ and therefore both columns are on a different vertical scale. Note that the $t = 0$ figures (top row) have a vertical scale twice as large as the other figures in the same column. The dashed lines in the figures indicate $\Delta n/n = 0$.

of the trailing edge of the condensate density wave under the experimental conditions. After about 200 ms the simulations indeed show the formation of shock waves.

We have run simulations for larger perturbations $\Delta n/n \approx 0.5$ and find shock waves to form within a few tens of milliseconds. Comparing these results to the sound propagation experiments by the MIT group [44, 100], where applied perturbations are reported as large as $\Delta n/n = 1$, suggests shock waves have formed in their experiments shortly after the sound wave is excited. The MIT group has measured the condensate density wave to propagate at c_B , even though strong nonlinear effects are expected to influence the propagation, as already remarked by Kavoulakis *et al.* [102].

In our experiment sound waves are excited in elongated cigar-shaped BECs allowing us to make a perturbation much longer than the radial size to ensure the excitation of a one-dimensional motion, while it remains small compared to the axial size. In the experiment reported by the MIT group the size of the excitation is of the order of the radial size of the BEC.

The simulations for small density perturbations ($\Delta n/n = 10^{-4}$) confirm the minimum of the density dip moves with c_B as given by Eq. (8.4) and shows the validity of the simulation. For the perturbation used in the experiment the simulations show the minimum of the dip propagates about 8% slower than

the speed of sound, in agreement with the estimate $\Delta c = -(c/2)\Delta n/n$. This is disadvantageous for the determination of the speed of sound from the measured density profiles, since the position of the minimum of the dip is the easiest parameter to derive. In order to derive the appropriate speed of sound from the density profiles, not only the position of minimum is determined, but also the amount of deformation is taken into account by determining the asymmetry of the propagating wave.

The simulations suggest the density at the $(1/e)$ -height of the dips is a good approximation of the unperturbed density (see Fig. 8.4). We therefore use the deformation at $(1/e)$ -height in addition to the position of the center of the perturbation in these simulations as the measure of the distance the perturbation has traveled. The speed of sound is now found to remain constant within 2% for a broad range of perturbation amplitudes (10^{-5} –0.3), only to show larger deviations when shock waves are formed. For typical propagation time used in the experiment, the simulations show the decrease of the propagation speed due to the axial density dependence remains below 2% as well.

8.4.2 Experiment

Returning to the results of the experiment, the measured density profiles are fitted to an asymmetric function, yielding both the deformation and position of the propagating density wave. Taking the same combined measure for the traveled distance as used in the simulations, the propagation distance varies linear with the propagation time, the slope of which is used to determine the speed of sound.

This procedure is repeated for different temperatures, which are created by adjusting the final rf-field frequency. Each series, consisting of about ten shots, is used to determine the propagation speed for that temperature. Rf-induced evaporative cooling does not allow to cool to temperatures below $k_B T \approx \mu$, since around this temperature both thermal atoms and condensed atoms are removed from the trap by the rf-field, setting a lower limit to the temperature reached in the experiment. The highest temperature used in the measurements corresponds to $T/T_c = 0.72 \pm 0.04$. For higher temperatures the axial length of the BEC becomes more than 15% shorter than the typical BEC length. By choosing this upper limit for the temperature prevents the need to account for the axial density dependence.

An unperturbed cloud in each series is used to derive the temperature, thermal density and BEC density for that series. In these measurements the chemical potential based on the axial size of the BEC and the total accumulated phase agree within 5%. The measured speeds are normalized to c_B based on the measured BEC density. The resulting normalized speed of sound as a function of reduced temperature and thermal density is shown in Fig. 8.5a. From these measurements

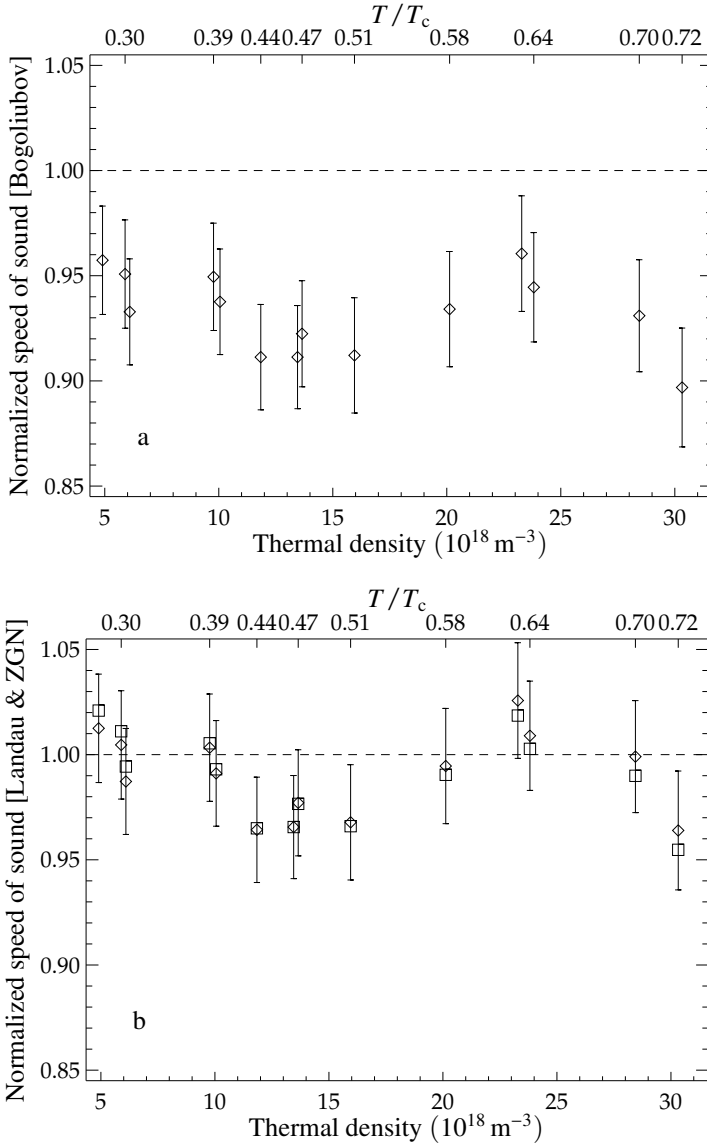


Figure 8.5: The normalized speed of sound as a function of the thermal density. The upper axis gives the reduced temperature T/T_c for the corresponding data point. Figure a shows the speed of sound normalized to c_B (Eq. (8.4)) based on the measured BEC density. Figure b shows the same measurements normalized to the speed of sound based on the Landau model (diamonds) and ZGN model (squares) based on the measured BEC and thermal densities. The main contribution to the error bars is the uncertainty in the measured densities.

we conclude that, even though the thermal density is varied over more than an order of magnitude, the effect of the thermal cloud appears to be constant within the accuracy of the measurement. Furthermore, the measured speeds are found to be approximately 7% lower than c_B given by Eq. (8.4). Note that since the condensate density is limited by three-body losses, the variation of n_c as a function of the temperature is modest.

In Fig. 8.5b the measured speeds are normalized using the speed of second sound calculated using the Landau and ZGN model. We find the measured propagation speed to be in excellent agreement with the speed of second sound given by both the Landau and ZGN model within the accuracy of the measurements. This result shows we have measured the effect of the thermal cloud on the propagation of a sound wave in the BEC. However, the dependence of the speed of second sound on the temperature is modest in the experimentally accessible temperature range. Furthermore, since the difference between the Landau and the ZGN model is smaller than the experimental uncertainty we cannot distinguish between both models in the current experiment.

We have not been able to observe a sound wave in the thermal cloud (first sound) in this experiment. For the higher temperatures this can be explained by the moderate perturbation depth compared to the thermal energy. At the lowest temperatures, still above $k_B T = \mu$, the thermal density is small and the thermal cloud spatially barely extends further than the BEC, causing the signal-to-noise to be insufficient to see small density perturbations in the thermal cloud in this regime. Above T_c we are able to observe a density perturbation when the excitation is of the order $k_B T$, but the excited wave damps too fast to be able to observe its propagation.

8.5 CONCLUSION

In conclusion, we have excited a hydrodynamic mode in a BEC: a propagating sound wave. We measure its propagation speed, which is used to determine the speed of sound in the BEC as a function of the temperature. The combination of the phase contrast imaging technique and elongated large atom number BECs allows us to make a moderate density excitation in the BEC and observe the propagation of a sound wave. Numerical simulations are conducted to model the nonlinear propagation. We find the speed of sound to be in good agreement with both the Landau model and ZGN model in which the coupling between the first and second sound modes is incorporated and thus we have observed the effect of the thermal cloud on the speed of sound in the BEC. However, the effect does not vary within the accuracy of the measurements with the temperature for our experimental conditions. The Bogoliubov speed of sound, in which this coupling between the two sound modes is absent, deviates significantly from the measured speeds reported in this chapter.

OBSERVATION OF SHOCK WAVES IN A LARGE BEC

Abstract

We observe the formation of shock waves in a Bose-Einstein condensate containing a large number of sodium atoms. The shock wave is initiated with a repulsive, blue-detuned light barrier, intersecting the BEC, after which two shock fronts appear. We observe breaking of these waves when the size of these waves approaches the healing length of the condensate. At this time, the wave front splits into two parts and clear fringes appear. The experiment is modeled using an effective 1D Gross-Pitaevskii-like equation and gives excellent quantitative agreement with the experiment, even though matter waves with wavelengths two orders of magnitude smaller than the healing length are present. In these experiments, no significant heating or particle loss is observed.

9.1 INTRODUCTION

The realization of Bose-Einstein condensates (BECs) in dilute atomic gases [1] provides the opportunity for the study of nonlinear matter wave dynamics. Many experiments on both the statics and dynamics of BECs have shown that experiments can often be modeled accurately by solving the mean-field Gross-Pitaevskii equation (GPE) [76].

For example it has successfully been used to model experiments on interferometry [75, 76], soliton formation [109, 110], four wave mixing [111], atom laser outcoupling [112–114], sound propagation, and superfluidity [76] to name a few. However, the Gross-Pitaevskii equation is not an exact description of a Bose-Einstein condensate, but instead it is expected to be a good approximation for condensates that contain a relatively large number of particles and are not undergoing violent dynamics [54, 115]. Thus it is of interest to experimentally probe the limits of validity of the GPE in describing the dynamics of Bose-Einstein condensates.

This chapter is based on a paper, which is accepted for publication in Physical Review A as *Observation of shock waves in a large Bose-Einstein condensate*, R. Meppelink, S. B. Koller, J. M. Vogels and P. van der Straten, E. D. van Ooijen, N. R. Heckenberg, H. Rubinsztein-Dunlop, S. A. Haine and M. J. Davis. The experiments are conducted in our group, the modeling is conducted by the group of M. J. Davis.

The well-known ‘Bosenova’ experiment of Donley *et al.* [116] is one situation where the validity of the GPE might be questioned, combining a small number of atoms with violent dynamics. The experiment began with a near ideal ^{85}Rb condensate of a few thousand atoms in its ground state before the atomic scattering length is manipulated using a Feshbach resonance to being attractive. The BEC is observed to collapse, emitting high energy jets and bursts of atoms. A number of computational studies have shown good qualitative agreement with the experimental observations [117–119]. However, careful quantitative studies have indicated that at the most basic level there is quantitative disagreement with the experimental data. Savage *et al.* showed that the experimentally measured collapse time is typically 25% shorter than predicted by simulations of the GPE [120]. Going beyond mean-field theory and including the first order quantum corrections to the dynamics is shown to make little difference to the numerical results [120, 121]. A second group of experiments by the same group found evidence for the formation of repulsive bright solitary waves in the condensate collapse [122]. However, modeling this experiment with the GPE is unable to reproduce this experimental finding [123].

Another example where the GPE has successfully modeled results of violent experiments is in the formation of quasi-1D bright solitons as reported in Refs [124, 125]. Both of these experiments involve a sudden change to an attractive scattering length. It has been shown [110] that the GPE can be used to successfully model these experiments. However, in this case, the three-body losses, which is not included in the GPE derivation, plays a nontrivial role in the dynamics, and the GPE must be modified by the addition of phenomenological damping terms in order to agree with these experiments.

Another situation exhibiting violent dynamics in the solution of the GPE without dissipation is in the generation of shock waves. Damski [126] has calculated the 1D GPE dynamics following the introduction and sudden removal of an attractive dimple potential in the center of a harmonically trapped elongated BEC. The localized density bulge splits into two pulses, which propagate toward the ends of the condensate. Due to the density dependent speed of sound in the system, the center of the pulse catches up to the front, creating a shock, and at this point the calculations develop a strong fringe pattern with a spacing of the order of the healing length corresponding to classical wave breaking. However, Damski speculated that in a physical system the Gross-Pitaevskii equation would become invalid at this point and this would not be observed in an experiment.

Recently, a number of experiments have been performed that have observed phenomena related to wave breaking in a Bose-Einstein condensate. The first experiments are conducted by Dutton *et al.* [127]. They used the slow light mechanism to create a defect in the condensate which is much narrower than the healing length. This defect created dark solitons which shed high frequencies

traveling at different velocities. The wave front of the propagating solitons eventually became curled and decayed into vortex pairs.

Simula *et al.* [128] blasted a hole in a rapidly rotating oblate BEC using a repulsive dipole potential and found qualitative agreement between their experimental observations and numerical calculations of the GPE. This was followed by Hofer *et al.* who performed similar experiments on a stationary and slowly rotating oblate BEC, and made the connection to dispersive shock waves in the GPE [129]. They found that this wave breaking phenomenon can be described by the Gross-Pitaevskii equation [130]. However, to obtain quantitative agreement between the simulations and the experimental observations they found that they had to use the laser width as a fitting parameter. In one situation agreement is obtained with a value 1.5 times larger than in the experiment, but in another it is required to be half as large, suggesting that this is not a systematic error but something more fundamental.

The purpose of this chapter is to generate shock waves in a large number, elongated BEC and to perform a quantitative comparison with simulations of an effective 1D GPE as a test of its validity in extreme conditions. We observe no indication of heating or particle loss, and conclude that even at these relatively high energy scales the GPE is valid for the time of the experiment. Soon after the experimental data for this work was taken, related work was reported by Chang *et al.* [106]. They also found good agreement with the GPE. However, these experiments are conducted at significantly lower energy scales, where agreement with the GPE is expected, and hence they did not perform a detailed investigation of the fringe spacing and possibility of heating.

9.2 EXPERIMENT

In our experiment we begin with an almost pure sodium BEC containing up to $100 \cdot 10^6$ atoms in the $|F_g, m_F\rangle = |1, -1\rangle$ hyperfine state. The atoms are magnetically confined in a clover leaf trap with harmonic trapping frequencies of 95.6 Hz in the radial direction and 3.91 Hz in the longitudinal direction. For the condensate, this corresponds to a chemical potential of 214 nK and Thomas-Fermi widths of $20 \mu\text{m}$ and $506 \mu\text{m}$ in the radial and axial directions, respectively. To create the initial disturbance we turn on a repulsive, blue-detuned laser beam focused in the middle of the BEC, intersecting the cloud in the longitudinal direction. This procedure is similar to the excitation scheme used to excite the sound waves described in Chapter 8, although the dipole potential used in these experiments is of the order of the chemical potential and thus much larger. The focus of the dipole beam has a waist of $90 \pm 11 \mu\text{m}$ ($1/e^2$) and a wavelength λ_L , tunable from 567 to 584 nm, where the power can be switched within $10 \mu\text{s}$. At $t = 0$ the blue-detuned laser is turned on suddenly with the magnetic trap still on and after variable times the cloud is imaged in the trap. Note that the waist of

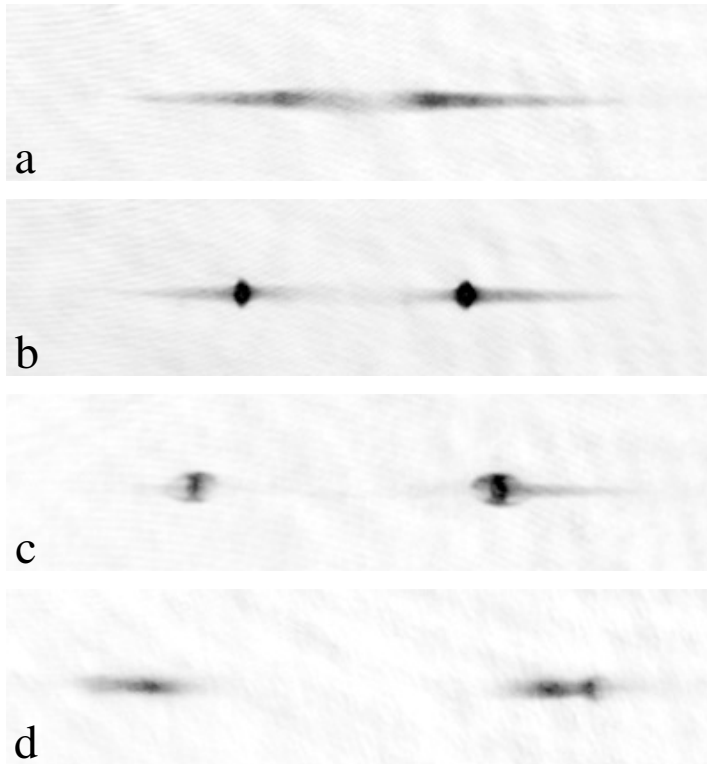


Figure 9.1: Phase contrast images of the BEC in the trap for (a-d) $t = 2, 5, 8$ and 15 ms after turning on the blue-detuned laser beam. The image size is $1200 \mu\text{m} \times 300 \mu\text{m}$.

the laser focus is much smaller than the axial width of the condensate and much larger than the radial widths, suggesting that most of the dynamics will occur along the axial direction.

9.2.1 Case 1

For the first set of experiments we make use of *in situ* phase contrast imaging (see Chapter 3). The detuning of the imaging laser is chosen such that a 2π phase shift is accumulated for the largest atom cloud density. The resolution is $3 \mu\text{m} \times 3 \mu\text{m}$ and the images are recorded with a CCD camera (Apogee AP1E). Figure 9.1 shows the in-trap CCD images for a BEC with $50 \cdot 10^6$ atoms, corresponding to a chemical potential $\mu = 162 \text{ nK}$, imaged after $t = 2, 6, 8$ and 15 ms, respectively. The power for the repulsive laser beam used is 78 mW with a wavelength of 579 nm , resulting in a repulsive barrier of $12.6 \mu\text{K}$. For all experiments the

scattering of photons from the laser can be neglected due to the large detuning used. The first image shows the splitting of the cloud induced by the switch on of the repulsive barrier. The density profile of the BEC results in a gradient in the speed of sound of the condensate v_c as $v_c \sim \sqrt{n}$. As a consequence, as the wave fronts induced by the lasers travel from the center toward the edge of the condensate with the back of the pulse catches up to the front, resulting in steepening of the wave (self-steepening). This is clearly observed in the second image. The last two images show that the wave breaks into two parts after the maximum density gradient has been reached.

9.2.2 Case 2

As the size of the fringes in the data set above is much smaller than the resolution of the imaging system, the experiment is repeated and imaged using absorption imaging after a 70 ms time-of-flight expansion to enlarge the detailed features of the condensate. This free expansion time is chosen in such a way that the full CCD array is used to obtain the maximum resolution. Figure 9.2 shows the images for a smaller condensate of $18 \cdot 10^6$ atoms for an evolution time in the trap of 0, 1, 2, 6, 13 and 25 ms, respectively. In this situation we use a repulsive laser beam with a power of 21 mW and a wavelength of 569 nm, corresponding to a repulsive potential barrier with a height of $0.43 \mu\text{K}$.

The images in Fig. 9.2 indicated that it takes longer for the build-up of the wave front for a smaller BEC and a weaker repulsive barrier. It can be seen that the shock front splits into two parts, where pronounced fringe patterns appear. Fourier analysis on the last image yields a fringe size of $6 \pm 1 \mu\text{m}$. Integration over the entire pixel array shows a 2.7% fluctuation in the number of atoms over an evolution time of 30 ms, suggesting that losses due to any potential heating are negligible. Figures e and f show that there is a slight curvature of the wave fronts, suggesting that the outer edge of the wave front has traveled faster than the center. We are currently uncertain of the cause of this.

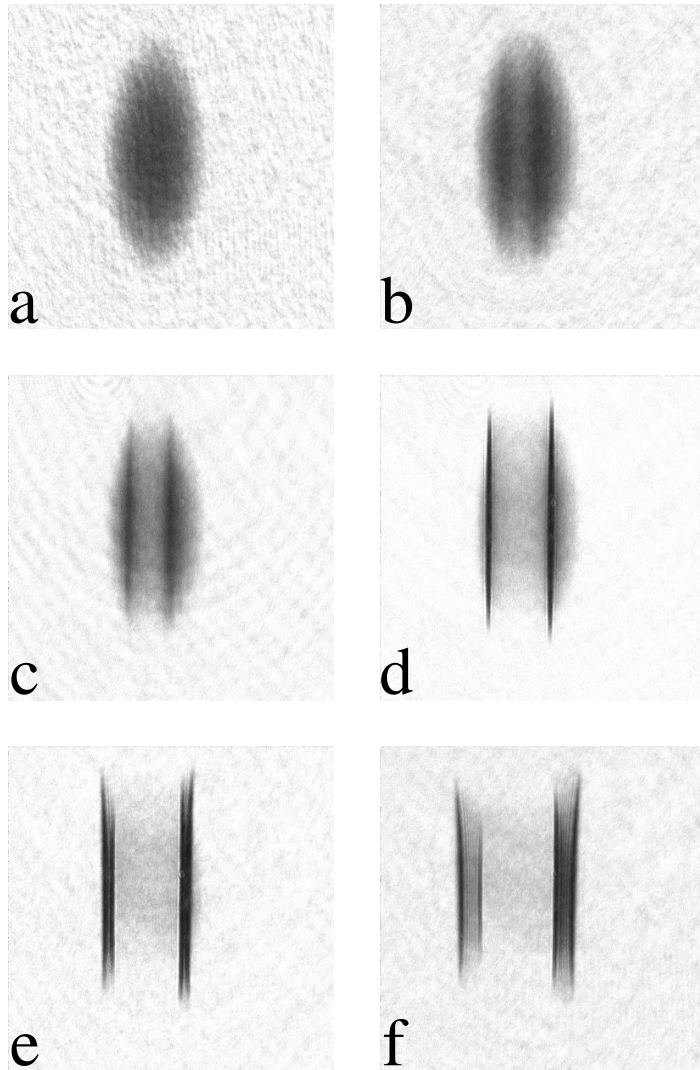


Figure 9.2: Absorption images of an 70 ms expanded BEC for (a-f) $t = 0, 1, 2, 6, 13$ and 25 ms after turning on the repulsive barrier. The size of the images is $2304 \mu\text{m} \times 1536 \mu\text{m}$.

9.3 NUMERICAL SIMULATIONS

We now turn to the numerical modeling of these experiments. Ideally we would do so with a fully three-dimensional simulation of the Gross-Pitaevskii equation. However, even making use of the cylindrical symmetry we find that the simulation parameters for such a large BEC are too demanding for numerical simulation with the computational resources we have available. To proceed we have made use of the fact that the system has cylindrical symmetry and a high aspect ratio, and reduced the problem to simulating the one-dimensional non-polynomial Gross-Pitaevskii equation (NPGPE) as derived by Salasnich *et al.* [74]. This assumes a variational Gaussian profile for the wave function in the radial direction whose width, $\sigma(z)$, is dependent on the local one dimensional density. This is to allow for the ‘bulging’ in the radial direction due to the mean field interaction to be included. The result is a 1D Gross-Pitaevskii equation where the nonlinear interaction term is a function of the local density. In the case of a harmonic trapping potential in the radial direction with trapping frequency ω_{rad} , the effective 1D equation of motion is

$$i\hbar \frac{d}{dt} \psi(z) = \left(\frac{-\hbar^2}{2m} \frac{\partial^2}{\partial z^2} + V(z) + \frac{U_{3D}}{2\pi\sigma^2} |\psi(z)|^2 + \left(\frac{\hbar^2}{2m} \sigma^{-2} + \frac{m\omega_{\text{rad}}^2}{2} \sigma^2 \right) \right) \psi(z), \quad (9.1)$$

with

$$\sigma^2(z) = \frac{\hbar}{m\omega_{\text{rad}}} \sqrt{1 + 2a|\psi(z)|^2}. \quad (9.2)$$

$V(z)$ represents the external potential along the z direction, $U_{3D} = 4\pi\hbar^2 a/m$ is the 3D atom-atom interaction strength, and a is the s -wave scattering length. We solve this equation numerically with no free parameters.

9.3.1 Case 1

We used Eq. (9.1) and Eq. (9.2) to simulate the experimental conditions used in Case 1. We used an initial condition of $50 \cdot 10^6$ atoms in the ground state of a harmonic trap of trapping frequencies $\omega_{\text{ax}}/(2\pi) = 3.9$ Hz and $\omega_{\text{rad}}/(2\pi) = 95.6$ Hz. The ground state is found by imaginary time propagation. A repulsive potential due to the laser beam is then switched on. The laser power is 49 mW, and detuned by 23 nm from resonance. We assumed that the beam profile is Gaussian with a width of 90 μm . This corresponds to a repulsive potential height of 0.87 μK .

Figure 9.3 shows a comparison of theoretical calculations with experimental data for these parameters. The left column (a-d) shows the density profile of

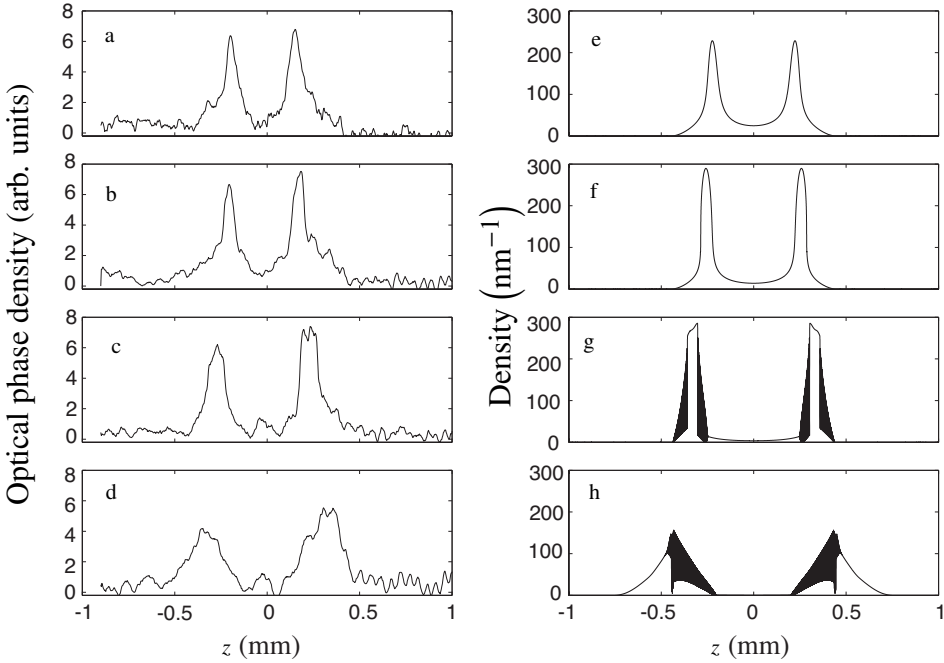


Figure 9.3: Comparison of theoretical calculations with the experimental data of Case 1. The left column (Figs. a–d) shows the density profile of the condensate, integrated along the radial direction, and the right column (Figs. e–h) shows the theoretical calculations. The images are for Figs. a and e: 11 ms, Figs. b and f: 14 ms, Figs. c and g: 21 ms, Figs. d and h: 32 ms after the repulsive potential is switched on. The laser power is 49 mW, which corresponds to a repulsive potential height of $0.87 \mu\text{K}$

the condensate, integrated along the radial direction, and the right column (e–h) shows the theoretical calculations. The images are for Figs. 9.3a and 9.3e 11 ms, Figs. 9.3b and 9.3f 14 ms, Figs. 9.3c and 9.3g 21 ms, Figs. 9.3d and 9.3h 32 ms after the repulsive potential is switched on.

The experimental images show that we get two pulses propagating outwards. The leading edges of these pulses gets steeper due to the density-dependent speed of sound [126]. The theoretical plots show agreement with the experimental data in terms of the position of the pulses and the steepening of the density. However, they show extra detail which the experimental image is insufficient to resolve. As the pulses steepen the relative density gradient become comparable to the healing length, and a shock wave forms. This causes an abrupt change in the

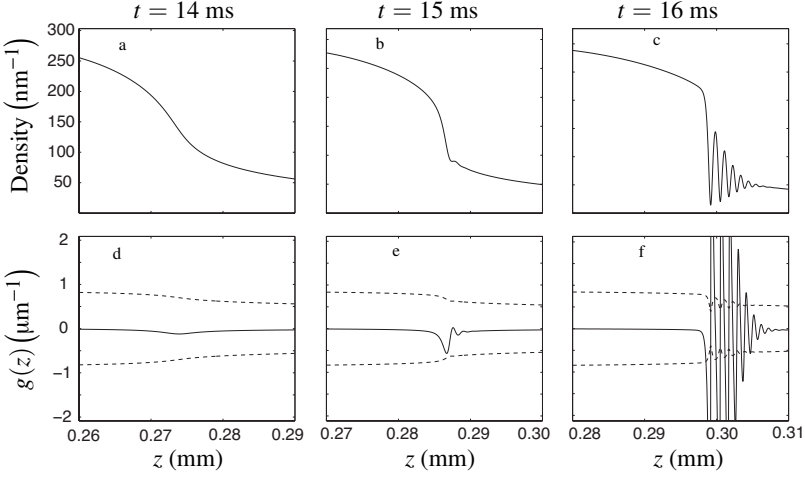


Figure 9.4: Top row: Close up of the density profile of the leading edge of the pulse for Fig. a: $t = 14$ ms, Fig. b: $t = 15$ ms, and Fig. c: $t = 16$ ms, for the same parameters as Fig. 9.3. Bottom row: The relative density gradient, $g(z)$ (solid line) and the inverse of the healing length $\pm k_{wb}(z)$ (dashed line) for the cases in Fig. a, Fig. b, and Fig. c respectively. In Fig. d, $|g(z)| \ll k_{wb}(z)$, so the pulse propagates smoothly. In Fig. e, $g(z)$ becomes comparable to $k_{wb}(z)$, and a shock front begins to form. In Fig. f, $|g(z)| \gg k_{wb}$, and high frequency oscillations are visible in the density profile.

density profile of the smooth pulse, resulting in rapid density oscillations behind and in front of the pulse. Figure (9.4) compares the relative density gradient

$$g(z) \equiv \frac{dn(z)}{n(z)dz}, \quad (9.3)$$

to the inverse of the healing length

$$k_{wb}(z) \equiv \frac{1}{\xi} = \frac{\sqrt{2mn(z)g(z)}}{\hbar}, \quad (9.4)$$

where $g(z) = U_{3D}/(2\pi\sigma^2(z))$ is the effective 1D interaction strength. In Figs. 9.4a and 9.4d, $|g(z)| \ll k_{wb}(z)$, and the density profile of the pulse remains smooth. In Figs. 9.4b and 9.4e, $|g(z)|$ becomes comparable to $k_{wb}(z)$, and a shock front begins to form. In Figs. 9.4c and 9.4f, $|g(z)| \gg k_{wb}$, and high frequency oscillations are visible in the density profile.

We found similar agreement between theoretical results and experimental data for repulsive barrier heights of $0.39 \mu\text{K}$ and $3.27 \mu\text{K}$ (corresponding to data presented in Fig. 9.1), which we have not presented here.

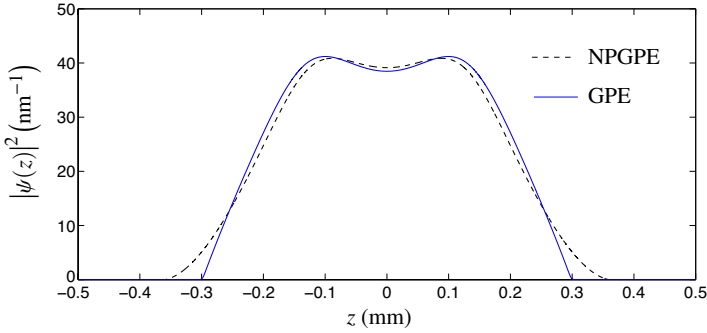


Figure 9.5: Comparison of the density profiles resulting from GPE (blue solid line) and NPGPE (dashed black line) simulations. The condensate is left to evolve in trap for 3 ms with a $0.88 \mu\text{K}$ repulsive barrier.

9.3.2 Case 2

In the second set of data we made use of time-of-flight imaging and are able to observe features that are not resolvable in trap. To make a comparison with this experimental data, we have modeled the expansion of the condensate in the radial direction during time of flight combined with continuing the 1D simulation of the dynamics of the wave function in the axial direction. We are unable to use the NPGPE in this case, as it is unable to model the expansion in the radial direction. Instead, we obtained a 1D set of equations by assuming a transverse radial width of the condensate, independent of z , which allows us to scale our nonlinearity to one dimension using $U_{1D} = U_{3D}/(\pi R^2)$. We chose this width parameter R by comparing the evolution while still in the trap to the evolution of the NPGPE with no free parameters, and chose the transverse width parameter which gives the best agreement to the results. Figure (9.5) shows the comparison between the solution to the GPE and the NPGPE after 3 ms of evolution, during the trapped phase of the evolution. For the GPE simulation, we set $R = 12 \mu\text{m}$, which yields the best agreement with the NPGPE.

During the expansion phase, we assumed that the transverse width expanded according to the analytic result derived by Castin and Dum [131] for the self-similar expansion of a Thomas-Fermi condensate. According to this result, the transverse width evolves according to $R(t) = R(0)\sqrt{1 + (\omega_{\text{rad}}t)^2}$. As we have neglected to include three dimensional effects in our simulation, we do not expect perfect agreement with the experimental data.

Figure 9.6 shows a density slice from the experimental data from Fig. 9.2 (integrated in the y direction for 100 pixels) compared to theoretical simulations. There is excellent agreement between these results. In both cases, high contrast

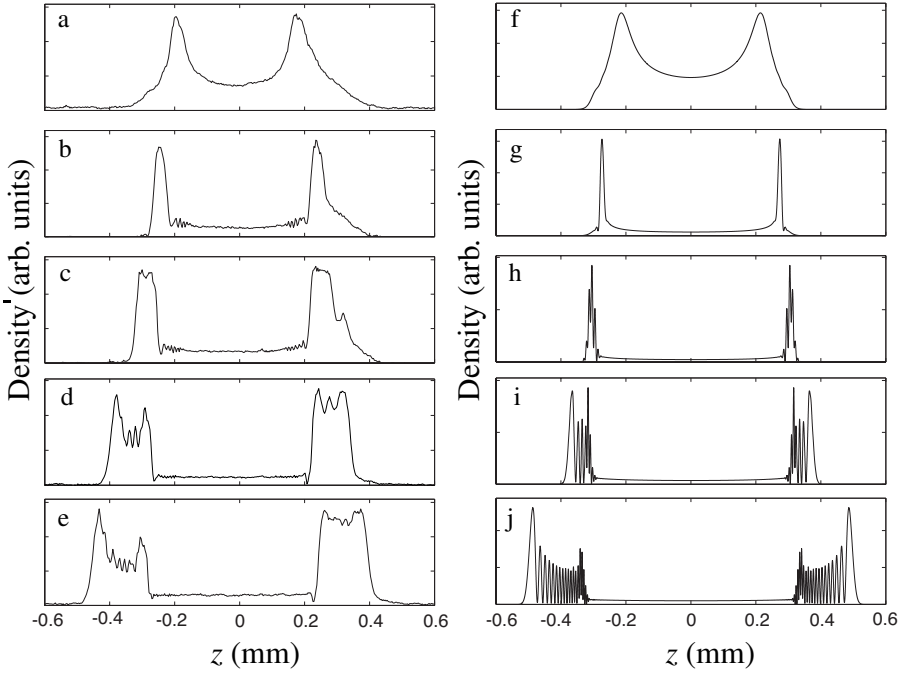


Figure 9.6: Density slice (left column), and theoretical 1D GPE simulation (right column) of the density profile of the condensate after expansion for 69 ms after evolving in the trap for various times. The condensate is held in the trap with the optical dipole on potential for Figs. a and f: 0.5 ms, Figs. b and g: 1.1 ms, Figs. c and h: 1.5 ms, Figs. d and i: 2.0 ms, Figs. e and j: 3.0 ms. Parameters: $N = 1.8 \cdot 10^7$ atoms, waist = 90 μm , $P = 21$ mW, detuning = 10 nm, corresponding to a barrier height of 0.88 μK .

fringes are observed when the back edge of the pulse catches up with the front edge. We find that the wave breaking occurs after a much shorter time compared to the case I, because the expansion in the radial direction leads to a rapid increase in the healing length.

There is considerable agreement between our simulation with no free parameters, and the experimental data, indicating that it is valid to simulate such a violent system with the GPE. The main cause of discrepancy between the experimental images and the theoretical calculations is most likely the uncertainty in the size of the waist of the blue-detuned beam ($90 \pm 11 \mu\text{m}$). By adjusting the value of the waist slightly in the calculations, we found better agreement with the experimental images, with the positions and widths of the wave packets giving best agreement for a waist of 92 μm . There is also a slight discrepancy

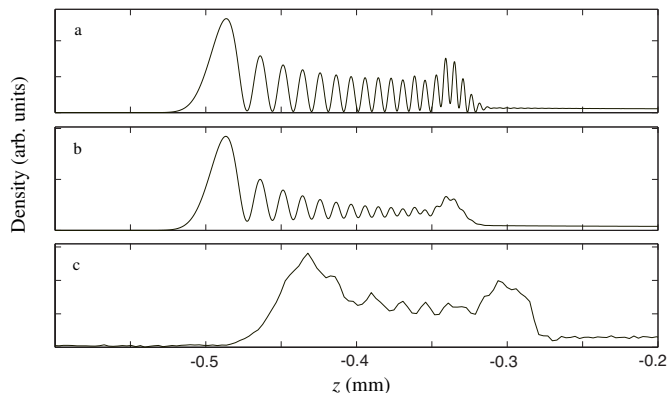


Figure 9.7: Close up view of the density slice for the same conditions as Figs. 9.6e and 9.6j. Figure a shows the raw simulation data, Fig. b shows the same data convolved with a $3\ \mu\text{m}$ Gaussian to emulate the finite pixel size of the camera, and Fig. c shows the experimental data. The discrepancy in the positions of the experimental and theoretical density distributions is most likely due to the uncertainty in the waist of the blue-detuned beam.

in the spatial frequency of the interference fringes for the experimental images and the simulation, the cause of which is unknown. It is difficult to accurately determine the spatial frequency in the experimental images, due to the $3\ \mu\text{m}$ pixel size causing spatial aliasing. The drop in observed fringe contrast in the experimental images is partly due to this spatial aliasing effect, but most likely is the result of a slight misalignment of the imaging axis with respect to the axis of the fringes in the 3D experiment. The asymmetry is due to a slight misalignment of the dipole barrier with the center of the trap. Figure (9.7) shows a comparison between the experimental data, and the results from the simulation convolved with a Gaussian of width $3\ \mu\text{m}$, to emulate the effect of the $3\ \mu\text{m}$ resolution. The fringe contrast is reduced as a result of the convolution, especially toward the back end of the pulse where the fringe separation is smaller. However, this effect is not enough to describe the lack of fringe contrast in the experimental images at the front of the pulse. One might suspect that the reduced fringe visibility is due to heating of the condensate atoms. However, no thermal fraction is observed. This is validated by repeating the experiment for different expansion times.

Inspection of Fig. 9.2 shows that the wave front of the leading edge of the pulse is slightly curved. As this curvature will also be present in the direction of imaging, this will also contribute to the loss of fringe visibility. Given these discrepancies, it is clear that the solutions of the GPE correctly capture the physical processes determining the evolution of the system.

9.4 CONCLUSION

We have generated shock waves in a large number elongated Bose-Einstein condensate by suddenly splitting it with a blue-detuned optical dipole potential. We observe no significant particle loss or heating over these time scales, and find excellent agreement with the predictions of our simulations of the 1D non-polynomial Gross-Pitaevskii equation. We used a method to describe the expansion of the elongated condensate while simulating the continuing dynamics in the long direction, and again find excellent agreement with simulations. Our study provides further evidence that the Gross-Pitaevskii equation can be an excellent approximation to the dynamics of condensates even in situations exhibiting violent dynamics and low dissipation.

BIBLIOGRAPHY

The references include a Digital Object Identifier (DOI) where available. The DOI provides a simple way to refer to a digital document. Simply add the DOI to the URL <http://dx.doi.org/>.

- [1] M. H. Anderson, J. R. Ensher, M. R. Matthews, C. E. Wieman, and E. A. Cornell. *Observation of Bose-Einstein condensation in a dilute atomic vapor*. *Science*, **269**: 198–201, 1995. DOI: [10.1126/science.269.5221.198](https://doi.org/10.1126/science.269.5221.198). URL: <http://www.sciencemag.org/cgi/content/abstract/269/5221/198>. (Cited on pages [1](#), [57](#), and [123](#).)
- [2] K. B. Davis, M. O. Mewes, M. R. Andrews, N. J. van Druten, D. S. Durfee, D. M. Kurn, and W. Ketterle. *Bose-Einstein condensation in a gas of sodium atoms*. *Phys. Rev. Lett.*, **75**: 3969–3973, 1995. DOI: [10.1103/PhysRevLett.75.3969](https://doi.org/10.1103/PhysRevLett.75.3969). (Cited on pages [1](#) and [57](#).)
- [3] E. L. Raab, M. Prentiss, A. Cable, S. Chu, and D. E. Pritchard. *Trapping of neutral sodium atoms with radiation pressure*. *Phys. Rev. Lett.*, **59**: 2631–2634, 1987. DOI: [10.1103/PhysRevLett.59.2631](https://doi.org/10.1103/PhysRevLett.59.2631). (Cited on page [1](#).)
- [4] W. H. Keesom. *The states of aggregation of condensed helium*. *Nature*, **122**: 847–849, 1926. (Cited on page [1](#).)
- [5] P. L. Kapitza. *Viscosity of liquid helium below the λ -point*. *Nature*, **141**: 74, 1938. DOI: [10.1038/141075a0](https://doi.org/10.1038/141075a0). (Cited on pages [1](#) and [97](#).)
- [6] J. F. Allen and A. D. Misener. *Flow of liquid helium II*. *Nature*, **141**: 75–75, 1938. DOI: [10.1038/141075a0](https://doi.org/10.1038/141075a0). (Cited on pages [1](#) and [97](#).)
- [7] J. F. Allen and H. Jones. *New phenomena connected with heat flow in helium II*. *Nature*, **141**: 243–244, 1938. (Cited on page [2](#).)
- [8] T. R. Sosnick, W. M. Snow, and P. E. Sokol. *Deep-inelastic neutron scattering from liquid ^4He* . *Phys. Rev. B*, **41**: 11185–11202, 1990. DOI: [10.1103/PhysRevB.41.11185](https://doi.org/10.1103/PhysRevB.41.11185). (Cited on page [2](#).)
- [9] H. R. Glyde, R. T. Azuah, and W. G. Stirling. *Condensate, momentum distribution, and final-state effects in liquid ^4He* . *Phys. Rev. B*, **62**: 14337–14349, 2000. DOI: [10.1103/PhysRevB.62.14337](https://doi.org/10.1103/PhysRevB.62.14337). (Cited on page [2](#).)
- [10] D. S. Jin, J. R. Ensher, M. R. Matthews, C. E. Wieman, and E. A. Cornell. *Collective excitations of a Bose-Einstein condensate in a dilute gas*. *Phys. Rev.*

- Lett., **77**: 420–423, 1996. DOI: [10.1103/PhysRevLett.77.420](https://doi.org/10.1103/PhysRevLett.77.420). (Cited on pages 2 and 57.)
- [11] M.-O. Mewes, M. R. Andrews, N. J. van Druten, D. M. Kurn, D. S. Durfee, C. G. Townsend, and W. Ketterle. *Collective excitations of a Bose-Einstein condensate in a magnetic trap*. Phys. Rev. Lett., **77**: 988–991, 1996. DOI: [10.1103/PhysRevLett.77.988](https://doi.org/10.1103/PhysRevLett.77.988). (Cited on pages 2 and 57.)
- [12] M. R. Andrews, C. G. Townsend, H.-J. Miesner, D. S. Durfee, D. M. Kurn, and W. Ketterle. *Observation of interference between two Bose condensates*. Science, **275**: 637–641, 1997. DOI: [10.1126/science.275.5300.637](https://doi.org/10.1126/science.275.5300.637). URL: <http://www.sciencemag.org/cgi/content/abstract/275/5300/637>. (Cited on page 2.)
- [13] D. M. Stamper-Kurn, H.-J. Miesner, S. Inouye, M. R. Andrews, and W. Ketterle. *Collisionless and hydrodynamic excitations of a Bose-Einstein condensate*. Phys. Rev. Lett., **81**: 500–503, 1998. DOI: [10.1103/PhysRevLett.81.500](https://doi.org/10.1103/PhysRevLett.81.500). (Cited on pages 2, 5, 58, 73, 83, 95, 98, 106, and 107.)
- [14] Ch. Buggle, P. Pedri, W. von Klitzing, and J. T. M. Walraven. *Shape oscillations in nondegenerate Bose gases: Transition from the collisionless to the hydrodynamic regime*. Phys. Rev. A, **72**: 043610, 2005. DOI: [10.1103/PhysRevA.72.043610](https://doi.org/10.1103/PhysRevA.72.043610). (Cited on pages 2, 5, 58, 61, 63, 76, and 77.)
- [15] D. Das and V. Natarajan. *High-precision measurement of hyperfine structure in the D lines of alkali atoms*. Journal of Physics B: Atomic, Molecular and Optical Physics, **41**: 035001 (12pp), 2008. URL: <http://stacks.iop.org/0953-4075/41/035001>. (Cited on page 7.)
- [16] D. Das, K. Pandey, A. Wasan, and V. Natarajan. *Resolving closely spaced hyperfine levels in the $3P_{3/2}$ state of ^{23}Na* . Journal of Physics B: Atomic, Molecular and Optical Physics, **39**: 3111–3119, 2006. URL: <http://stacks.iop.org/0953-4075/39/3111>. (Cited on page 7.)
- [17] A. Beckmann, K. D. Böklen, and D. Elke. *Precision measurements of the nuclear magnetic dipole moments of ^6Li , ^7Li , ^{23}Na , ^{39}K and ^{41}K* . Zeitschrift für Physik, **270**: 173–186, 1974. DOI: [10.1007/BF01680407](https://doi.org/10.1007/BF01680407). URL: <http://www.springerlink.com/content/q458666655561108>. (Cited on page 7.)
- [18] P. Juncar, J. Pinard, J. Hamon, and A. Chartier. *Absolute determination of the wavelengths of the sodium D_1 and D_2 lines by using a CW tunable dye laser stabilized on iodine*. Metrologia, **17**: 77–79, 1981. URL: <http://stacks.iop.org/0026-1394/17/77>. (Cited on pages 7 and 8.)

- [19] U. Volz, M. Majerus, H. Liebel, A. Schmitt, and H. Schmoranzer. *Precision lifetime measurements on NaI $3p^2P_{1/2}$ and $3p^2P_{3/2}$ by beam-gas-laser spectroscopy*. Phys. Rev. Lett., **76**: 2862–2865, 1996. DOI: [10.1103/PhysRevLett.76.2862](https://doi.org/10.1103/PhysRevLett.76.2862). (Cited on page 8.)
- [20] M. P. Bradley, J. V. Porto, S. Rainville, J. K. Thompson, and D. E. Pritchard. *Penning trap measurements of the masses of ^{133}Cs , $^{85,87}\text{Rb}$, and ^{23}Na with uncertainties ≤ 0.2 ppb*. Phys. Rev. Lett., **83**: 4510–4513, 1999. DOI: [10.1103/PhysRevLett.83.4510](https://doi.org/10.1103/PhysRevLett.83.4510). (Cited on page 8.)
- [21] C. Samuelis, E. Tiesinga, T. Laue, M. Elbs, H. Knöckel, and E. Tiemann. *Cold atomic collisions studied by molecular spectroscopy*. Phys. Rev. A, **63**: 012710, 2000. DOI: [10.1103/PhysRevA.63.012710](https://doi.org/10.1103/PhysRevA.63.012710). (Cited on page 8.)
- [22] D. A. Steck. *Sodium D line data*, 2009. URL: <http://steck.us/alkalidata/>. (Cited on page 8.)
- [23] W. Demtröder. *Laser Spectroscopy*. Springer, 1995. (Cited on page 11.)
- [24] G. C. Bjorklund. *Frequency-modulation spectroscopy: a new method for measuring weak absorptions and dispersions*. Opt. Lett., **5**: 15, 1980. URL: <http://ol.osa.org/abstract.cfm?URI=ol-5-1-15>. (Cited on page 11.)
- [25] E. D. van Ooijen, G. Katgert, and P. van der Straten. *Laser frequency stabilization using Doppler-free bichromatic spectroscopy*. Applied Physics B: Lasers and Optics, **79**: 57–59, 2004. DOI: DOI - [10.1007/s00340-004-1522-6](https://doi.org/10.1007/s00340-004-1522-6). URL: <http://www.springerlink.com/content/qth4xr5l6d3vk4v>. (Cited on page 14.)
- [26] C. A. Stan. *Experiments with Interacting Bose and Fermi Gases*. PhD thesis, Massachusetts Institute of Technology, 2005. (Cited on page 14.)
- [27] W. D. Phillips and H. Metcalf. *Laser deceleration of an atomic beam*. Phys. Rev. Lett., **48**: 596–599, 1982. DOI: [10.1103/PhysRevLett.48.596](https://doi.org/10.1103/PhysRevLett.48.596). (Cited on page 15.)
- [28] P. A. Molenaar. *Photoassociative reactions of laser-cooled sodium*. PhD thesis, Universiteit Utrecht, 1996. (Cited on page 15.)
- [29] E. D. van Ooijen. *Realization and Illumination of Bose-condensed Sodium Atoms*. PhD thesis, Universiteit Utrecht, 2005. (Cited on pages 15 and 20.)
- [30] K. M. R. van der Stam. *Superradiant scattering of laser light from a Bose-Einstein condensate*. PhD thesis, Universiteit Utrecht, 2006. (Cited on pages 15, 17, and 20.)
- [31] R. A. Rozendaal. *Counting Bose-condensed sodium atoms using phase-contrast imaging*. Master’s thesis, Universiteit Utrecht, 2007. (Cited on page 16.)

- [32] W. Ketterle, K. B. Davis, M. A. Joffe, A. Martin, and D. E. Pritchard. *High densities of cold atoms in a dark spontaneous-force optical trap*. Phys. Rev. Lett., **70**: 2253–2256, 1993. DOI: [10.1103/PhysRevLett.70.2253](https://doi.org/10.1103/PhysRevLett.70.2253). (Cited on page 18.)
- [33] R. van Rooij. *Heat conduction in an ultra-cold quantum gas*. Master’s thesis, Universiteit Utrecht, 2007. (Cited on page 18.)
- [34] K. M. R. van der Stam, A. Kuijk, R. Meppelink, J. M. Vogels, and P. van der Straten. *Spin-polarizing cold sodium atoms in a strong magnetic field*. Phys. Rev. A, **73**: 063412, 2006. DOI: [10.1103/PhysRevA.73.063412](https://doi.org/10.1103/PhysRevA.73.063412). (Cited on pages 19 and 114.)
- [35] D. van Oosten. *Quantum gases in optical lattices: the atomic Mott insulator*. PhD thesis, Universiteit Utrecht, 2004. (Cited on page 20.)
- [36] K. M. R. van der Stam, R. Meppelink, J. M. Vogels, and P. van der Straten. *Reaching the hydrodynamic regime in a Bose-Einstein condensate by suppression of avalanches*. Phys. Rev. A, **75**: 031602, 2007. DOI: [10.1103/PhysRevA.75.031602](https://doi.org/10.1103/PhysRevA.75.031602). (Cited on pages 21, 61, 74, 98, and 114.)
- [37] M. Hugbart, J. A. Retter, A. F. Varón, P. Bouyer, A. Aspect, and M. J. Davis. *Population and phase coherence during the growth of an elongated Bose-Einstein condensate*. Phys. Rev. A, **75**: 011602, 2007. DOI: [10.1103/PhysRevA.75.011602](https://doi.org/10.1103/PhysRevA.75.011602). (Cited on page 23.)
- [38] H. Kreutzmann, A. Sanpera, L. Santos, M. Lewenstein, D. Hellweg, L. Cacciapuoti, M. Kottke, T. Schulte, K. Sengstock, J. J. Arlt, and W. Ertmer. *Characterization and control of phase fluctuations in elongated Bose-Einstein condensates*. Applied Physics B: Lasers and Optics, **76**: 165–172, 2003. DOI: [10.1007/s00340-002-1074-6](https://doi.org/10.1007/s00340-002-1074-6). (Cited on page 23.)
- [39] W. Ketterle, D. S. Durfee, and D. M. Stamper-Kurn. *Making, probing and understanding Bose-Einstein condensates*. In *Proceedings of the International School of Physics “E. Fermi”*, volume 140. IOSPress, 1999. URL: <http://www.citebase.org/abstract?id=oai:arXiv.org:cond-mat/9904034>. (Cited on pages 31, 40, 47, 65, 67, and 69.)
- [40] G. Reinaudi, T. Lahaye, Z. Wang, and D. Guéry-Odelin. *Strong saturation absorption imaging of dense clouds of ultracold atoms*. Opt. Lett., **32**: 3143–3145, 2007. URL: <http://ol.osa.org/abstract.cfm?URI=ol-32-21-3143>. (Cited on pages 32 and 49.)
- [41] M. T. DePue, S. L. Winoto, D. J. Han, and D. S. Weiss. *Transient compression of a MOT and high intensity fluorescent imaging of optically thick clouds of atoms*. Optics Communications, **180**: 73–79,

2000. ISSN 0030-4018. DOI: [10.1016/S0030-4018\(00\)00701-X](https://doi.org/10.1016/S0030-4018(00)00701-X). URL: <http://www.sciencedirect.com/science/article/B6TVF-40F1PMW-C/2/caf335aa644b13a893500d7bd55214e0>. (Cited on page 32.)
- [42] C. C. Bradley, C. A. Sackett, and R. G. Hulet. *Bose-Einstein condensation of lithium: Observation of limited condensate number*. Phys. Rev. Lett., **78**: 985–989, 1997. DOI: [10.1103/PhysRevLett.78.985](https://doi.org/10.1103/PhysRevLett.78.985). (Cited on page 32.)
- [43] M. R. Andrews, M.-O. Mewes, N. J. van Druten, D. S. Durfee, D. M. Kurn, and W. Ketterle. *Direct, nondestructive observation of a Bose condensate*. Science, **273**: 84–87, 1996. DOI: [10.1126/science.273.5271.84](https://doi.org/10.1126/science.273.5271.84). URL: <http://www.sciencemag.org/cgi/content/abstract/273/5271/84>. (Cited on pages 32, 34, and 114.)
- [44] M. R. Andrews, D. M. Kurn, H.-J. Miesner, D. S. Durfee, C. G. Townsend, S. Inouye, and W. Ketterle. *Propagation of sound in a Bose-Einstein condensate*. Phys. Rev. Lett., **79**: 553–556, 1997. DOI: [10.1103/PhysRevLett.79.553](https://doi.org/10.1103/PhysRevLett.79.553). (Cited on pages 32, 34, 110, and 118.)
- [45] L. D. Turner, K. F. E. M. Domen, and R. E. Scholten. *Diffraction-contrast imaging of cold atoms*. Phys. Rev. A, **72**: 031403, 2005. DOI: [10.1103/PhysRevA.72.031403](https://doi.org/10.1103/PhysRevA.72.031403). (Cited on page 32.)
- [46] S. Kadlecik, J. Sebby, R. Newell, and T. G. Walker. *Nondestructive spatial heterodyne imaging of cold atoms*. Opt. Lett., **26**: 137–139, 2001. URL: <http://ol.osa.org/abstract.cfm?URI=ol-26-3-137>. (Cited on pages 32 and 34.)
- [47] F. Zernike. *Phase-contrast, a new method for microscopic observation of transparent objects*. Physica, **9**: 686–698, 1942. (Cited on page 33.)
- [48] L. D. Turner, K. P. Weber, D. Paganin, and R. E. Scholten. *Off-resonant defocus-contrast imaging of cold atoms*. Opt. Lett., **29**: 232–234, 2004. URL: <http://ol.osa.org/abstract.cfm?URI=ol-29-3-232>. (Cited on page 34.)
- [49] G. Nienhuis, P. van der Straten, and S.-Q. Shang. *Operator description of laser cooling below the Doppler limit*. Phys. Rev. A, **44**: 462–474, 1991. DOI: [10.1103/PhysRevA.44.462](https://doi.org/10.1103/PhysRevA.44.462). (Cited on page 35.)
- [50] J. J. Sakurai. *Modern Quantum Mechanics*. Addison-Wesley Publishing Company, 1995. (Cited on page 35.)
- [51] J. D. Jackson. *Classical Electrodynamics*. John Wiley & Sons, Inc., third edition edition, 1999. (Cited on page 37.)
- [52] O. Morice, Y. Castin, and J. Dalibard. *Refractive index of a dilute Bose gas*. Phys. Rev. A, **51**: 3896–3901, 1995. DOI: [10.1103/PhysRevA.51.3896](https://doi.org/10.1103/PhysRevA.51.3896). (Cited on page 37.)

- [53] We acknowledge Chris Rétif and AMOLF for the manufacturing of the phase spot., 2007. (Cited on page 39.)
- [54] C. J. Pethick and H. Smith. *Bose-Einstein condensation in dilute gases*. Cambridge University Press, 2002. (Cited on pages 41, 42, 53, 58, 59, and 123.)
- [55] M. Naraschewski and D. M. Stamper-Kurn. *Analytical description of a trapped semi-ideal Bose gas at finite temperature*. *Phys. Rev. A*, **58**: 2423–2426, 1998. DOI: [10.1103/PhysRevA.58.2423](https://doi.org/10.1103/PhysRevA.58.2423). (Cited on page 42.)
- [56] F. Gerbier, J. H. Thywissen, S. Richard, M. Hugbart, P. Bouyer, and A. Aspect. *Experimental study of the thermodynamics of an interacting trapped Bose-Einstein condensed gas*. *Phys. Rev. A*, **70**: 013607, 2004. DOI: [10.1103/PhysRevA.70.013607](https://doi.org/10.1103/PhysRevA.70.013607). (Cited on pages 45 and 50.)
- [57] S. Giorgini, L. P. Pitaevskii, and S. Stringari. *Scaling and thermodynamics of a trapped Bose-condensed gas*. *Phys. Rev. Lett.*, **78**: 3987–3990, 1997. DOI: [10.1103/PhysRevLett.78.3987](https://doi.org/10.1103/PhysRevLett.78.3987). (Cited on page 50.)
- [58] B. D. Busch, C. Liu, Z. Dutton, C. H. Behroozi, and L. Vestergaard Hau. *Observation of interaction dynamics in finite-temperature Bose condensed atom clouds*. *Europhysics Letters*, **51**: 485–491, 2000. DOI: [10.1209/epl/i2000-00363-0](https://doi.org/10.1209/epl/i2000-00363-0). (Cited on page 50.)
- [59] D. S. Jin, M. R. Matthews, J. R. Ensher, C. E. Wieman, and E. A. Cornell. *Temperature-dependent damping and frequency shifts in collective excitations of a dilute Bose-Einstein condensate*. *Phys. Rev. Lett.*, **78**: 764–767, 1997. DOI: [10.1103/PhysRevLett.78.764](https://doi.org/10.1103/PhysRevLett.78.764). (Cited on pages 57, 73, and 83.)
- [60] M. Edwards, P. A. Ruprecht, K. Burnett, R. J. Dodd, and C. W. Clark. *Collective excitations of atomic Bose-Einstein condensates*. *Phys. Rev. Lett.*, **77**: 1671–1674, 1996. DOI: [10.1103/PhysRevLett.77.1671](https://doi.org/10.1103/PhysRevLett.77.1671). (Cited on page 57.)
- [61] S. Stringari. *Collective excitations of a trapped Bose-condensed gas*. *Phys. Rev. Lett.*, **77**: 2360–2363, 1996. DOI: [10.1103/PhysRevLett.77.2360](https://doi.org/10.1103/PhysRevLett.77.2360). (Cited on pages 57, 58, and 60.)
- [62] A. Griffin, W.-C. Wu, and S. Stringari. *Hydrodynamic modes in a trapped Bose gas above the Bose-Einstein transition*. *Phys. Rev. Lett.*, **78**: 1838–1841, 1997. DOI: [10.1103/PhysRevLett.78.1838](https://doi.org/10.1103/PhysRevLett.78.1838). (Cited on pages 57, 58, and 60.)
- [63] G. M. Kavoulakis, C. J. Pethick, and H. Smith. *Damping of hydrodynamic modes in a trapped Bose gas above the Bose-Einstein transition temperature*. *Phys. Rev. A*, **57**: 2938–2941, 1998. DOI: [10.1103/PhysRevA.57.2938](https://doi.org/10.1103/PhysRevA.57.2938). (Cited on page 57.)

- [64] M. Leduc, J. Leonard, F. Pereira dos Santos, E. Jahier, S. Schwartz, and C. Cohen-Tannoudji. *Hydrodynamic modes in a trapped gas of metastable helium above the Bose-Einstein transition*. Acta Physica Polonica B, **33**: 2213, 2002. (Cited on pages 58 and 67.)
- [65] D. Guéry-Odelin, F. Zambelli, J. Dalibard, and S. Stringari. *Collective oscillations of a classical gas confined in harmonic traps*. Phys. Rev. A, **60**: 4851–4856, 1999. DOI: [10.1103/PhysRevA.60.4851](https://doi.org/10.1103/PhysRevA.60.4851). (Cited on pages 58, 61, 63, 64, 77, and 79.)
- [66] N. P. Proukakis and B. Jackson. *Finite-temperature models of Bose-Einstein condensation*. Journal of Physics B: Atomic, Molecular and Optical Physics, **41**: 203002 (66pp), 2008. URL: <http://stacks.iop.org/0953-4075/41/203002>. (Cited on page 58.)
- [67] E. Zaremba, A. Griffin, and T. Nikuni. *Two-fluid hydrodynamics for a trapped weakly interacting Bose gas*. Phys. Rev. A, **57**: 4695–4698, 1998. DOI: [10.1103/PhysRevA.57.4695](https://doi.org/10.1103/PhysRevA.57.4695). (Cited on pages 58, 98, 110, and 112.)
- [68] J. C. K. Yongli Ma, S. T. Chui. *Collective excitations of a trapped Bose-Einstein condensate at finite large atom numbers*. Journal of Low Temperature Physics, **129**: 79–92, 2002. DOI: [10.1023/A:1020001519190](https://doi.org/10.1023/A:1020001519190). (Cited on page 58.)
- [69] L. Pitaevskii and S. Stringari. *Elementary excitations in trapped Bose-Einstein condensed gases beyond the mean-field approximation*. Phys. Rev. Lett., **81**: 4541–4544, 1998. DOI: [10.1103/PhysRevLett.81.4541](https://doi.org/10.1103/PhysRevLett.81.4541). (Cited on pages 62 and 70.)
- [70] T. Nikuni and A. Griffin. *Frequency and damping of hydrodynamic modes in a trapped Bose-condensed gas*. Phys. Rev. A, **69**: 023604, 2004. DOI: [10.1103/PhysRevA.69.023604](https://doi.org/10.1103/PhysRevA.69.023604). (Cited on pages 63 and 67.)
- [71] T. Nikuni and A. Griffin. *Temperature-dependent relaxation times in a trapped Bose-condensed gas*. Phys. Rev. A, **65**: 011601, 2001. DOI: [10.1103/PhysRevA.65.011601](https://doi.org/10.1103/PhysRevA.65.011601). (Cited on pages 64, 66, 98, 99, 111, and 113.)
- [72] R. A. Duine and H. T. C. Stoof. *Stochastic dynamics of a trapped Bose-Einstein condensate*. Phys. Rev. A, **65**: 013603, 2001. DOI: [10.1103/PhysRevA.65.013603](https://doi.org/10.1103/PhysRevA.65.013603). (Cited on page 67.)
- [73] W. Bao, D. Jaksch, and P. A. Markowich. *Numerical solution of the Gross-Pitaevskii equation for Bose-Einstein condensation*. Journal of Computational Physics, **187**: 318–342, 2003. ISSN 0021-9991. DOI: [DOI: 10.1016/S0021-9991\(03\)00102-5](https://doi.org/10.1016/S0021-9991(03)00102-5). URL: <http://www.sciencedirect.com/science/article/B6WHY-487122Y-4/2/ece39a061526c2d1488dc61c20d919a1>. (Cited on pages 69 and 117.)

- [74] L. Salasnich, A. Parola, and L. Reatto. *Effective wave equations for the dynamics of cigar-shaped and disk-shaped Bose condensates*. Phys. Rev. A, **65**: 043614, 2002. DOI: [10.1103/PhysRevA.65.043614](https://doi.org/10.1103/PhysRevA.65.043614). (Cited on pages 70, 117, and 129.)
- [75] D. Ananikian and T. Bergeman. *Gross-Pitaevskii equation for Bose particles in a double-well potential: Two-mode models and beyond*. Phys. Rev. A, **73**: 013604, 2006. DOI: [10.1103/PhysRevA.73.013604](https://doi.org/10.1103/PhysRevA.73.013604). (Cited on pages 70, 117, and 123.)
- [76] F. Dalfovo, S. Giorgini, L. P. Pitaevskii, and S. Stringari. *Theory of Bose-Einstein condensation in trapped gases*. Rev. Mod. Phys., **71**: 463–512, 1999. DOI: [10.1103/RevModPhys.71.463](https://doi.org/10.1103/RevModPhys.71.463). (Cited on pages 70, 106, 117, and 123.)
- [77] P. Engels, C. Atherton, and M. A. Hofer. *Observation of Faraday waves in a Bose-Einstein condensate*. Phys. Rev. Lett., **98**: 095301, 2007. DOI: [10.1103/PhysRevLett.98.095301](https://doi.org/10.1103/PhysRevLett.98.095301). (Cited on page 70.)
- [78] E. Zaremba, T. Nikuni, and A. Griffin. *Dynamics of trapped Bose gases at finite temperatures*. Journal of Low Temperature Physics, **116**: 277–345, 1999. DOI: [10.1023/A:1021846002995](https://doi.org/10.1023/A:1021846002995). (Cited on pages 73, 74, 98, 110, 112, 113, and 114.)
- [79] T. Nikuni and A. Griffin. *Hydrodynamic damping in trapped Bose gases*. Journal of Low Temperature Physics, **111**: 793–814, 1998. DOI: [10.1023/A:1022221123509](https://doi.org/10.1023/A:1022221123509). (Cited on pages 74 and 79.)
- [80] T. Lahaye, J. M. Vogels, K. J. Günter, Z. Wang, J. Dalibard, and D. Guéry-Odelin. *Realization of a magnetically guided atomic beam in the collisional regime*. Phys. Rev. Lett., **93**: 093003, 2004. DOI: [10.1103/PhysRevLett.93.093003](https://doi.org/10.1103/PhysRevLett.93.093003). (Cited on page 74.)
- [81] M. Kozuma, L. Deng, E. W. Hagley, J. Wen, R. Lutwak, K. Helmerson, S. L. Rolston, and W. D. Phillips. *Coherent splitting of Bose-Einstein condensed atoms with optically induced Bragg diffraction*. Phys. Rev. Lett., **82**: 871–875, 1999. DOI: [10.1103/PhysRevLett.82.871](https://doi.org/10.1103/PhysRevLett.82.871). (Cited on pages 75 and 84.)
- [82] S. Chapman. *On the law of distribution of molecular velocities, and on the theory of viscosity and thermal conduction, in a non-uniform simple monatomic gas*. Royal Society of London Philosophical Transactions Series A, **216**: 279–348, 1916. (Cited on page 79.)
- [83] D. Enskog. *Kinetische Theorie der Vorgänge in mässig verdünnten Gasen, Dynamical Theory of Gases*. PhD thesis, Uppsala, 1917. (Cited on page 79.)
- [84] J. M. Vogels, W. C. Germs, and P. van der Straten. To be published. (Cited on page 80.)

- [85] F. Ferlaino, P. Maddaloni, S. Burger, F. S. Cataliotti, C. Fort, M. Modugno, and M. Inguscio. *Dynamics of a Bose-Einstein condensate at finite temperature in an atom-optical coherence filter*. Phys. Rev. A, **66**: 011604, 2002. DOI: [10.1103/PhysRevA.66.011604](https://doi.org/10.1103/PhysRevA.66.011604). (Cited on pages 95, 98, and 106.)
- [86] K. W. Madison, F. Chevy, W. Wohlleben, and J. Dalibard. *Vortex formation in a stirred Bose-Einstein condensate*. Phys. Rev. Lett., **84**: 806–809, 2000. DOI: [10.1103/PhysRevLett.84.806](https://doi.org/10.1103/PhysRevLett.84.806). (Cited on page 97.)
- [87] M. R. Matthews, B. P. Anderson, P. C. Haljan, D. S. Hall, C. E. Wieman, and E. A. Cornell. *Vortices in a Bose-Einstein condensate*. Phys. Rev. Lett., **83**: 2498–2501, 1999. DOI: [10.1103/PhysRevLett.83.2498](https://doi.org/10.1103/PhysRevLett.83.2498). (Cited on page 97.)
- [88] C. Ryu, M. F. Andersen, P. Cladé, V. Natarajan, K. Helmerson, and W. D. Phillips. *Observation of persistent flow of a Bose-Einstein condensate in a toroidal trap*. Phys. Rev. Lett., **99**: 260401, 2007. DOI: [10.1103/PhysRevLett.99.260401](https://doi.org/10.1103/PhysRevLett.99.260401). (Cited on page 97.)
- [89] C. Raman, M. Köhl, R. Onofrio, D. S. Durfee, C. E. Kuklewicz, Z. Hadzibabic, and W. Ketterle. *Evidence for a critical velocity in a Bose-Einstein condensed gas*. Phys. Rev. Lett., **83**: 2502–2505, 1999. DOI: [10.1103/PhysRevLett.83.2502](https://doi.org/10.1103/PhysRevLett.83.2502). (Cited on page 97.)
- [90] E. Taylor and A. Griffin. *Two-fluid hydrodynamic modes in a trapped superfluid gas*. Phys. Rev. A, **72**: 053630, 2005. DOI: [10.1103/PhysRevA.72.053630](https://doi.org/10.1103/PhysRevA.72.053630). (Cited on page 98.)
- [91] P. C. Hohenberg and P. C. Martin. *Microscopic theory of superfluid helium*. Annals of Physics, **34**: 291–359, 1965. ISSN 0003-4916. DOI: [DOI: 10.1016/0003-4916\(65\)90280-0](https://doi.org/10.1016/0003-4916(65)90280-0). URL: <http://www.sciencedirect.com/science/article/B6WB1-4DF4VRF-P/2/c3122ccaa4c6d2f4bfcf3c047f467dff>. (Cited on page 106.)
- [92] P. Szépfalusy and I. Kondor. *On the dynamics of continuous phase transitions*. Annals of Physics, **82**: 1–53, 1974. ISSN 0003-4916. DOI: [DOI: 10.1016/0003-4916\(74\)90330-3](https://doi.org/10.1016/0003-4916(74)90330-3). URL: <http://www.sciencedirect.com/science/article/B6WB1-4DDR8Y8-269/2/6de6ebf4a34fad35098bf4667ae96ff>. (Cited on page 106.)
- [93] W. Vincent Liu. *Theoretical study of the damping of collective excitations in a Bose-Einstein condensate*. Phys. Rev. Lett., **79**: 4056–4059, 1997. DOI: [10.1103/PhysRevLett.79.4056](https://doi.org/10.1103/PhysRevLett.79.4056). (Cited on page 106.)
- [94] L. P. Pitaevskii and S. Stringari. *Landau damping in dilute Bose gases*. Physics Letters A, **235**: 398–402, 1997. ISSN 0375-9601. DOI: [DOI: 10.1016/S0375-9601\(97\)00666-X](https://doi.org/10.1016/S0375-9601(97)00666-X). URL:

<http://www.sciencedirect.com/science/article/B6TVM-3SPV3CF-49/2/07bf8f32e1a706ed0e2be144bf2b8230>. (Cited on page 106.)

- [95] P. O. Fedichev, G. V. Shlyapnikov, and J. T. M. Walraven. *Damping of low-energy excitations of a trapped Bose-Einstein condensate at finite temperatures*. Phys. Rev. Lett., **80**: 2269–2272, 1998. DOI: [10.1103/PhysRevLett.80.2269](https://doi.org/10.1103/PhysRevLett.80.2269). (Cited on page 106.)
- [96] A. Griffin. *Condensate oscillations, kinetic equations and two-fluid hydrodynamics in a Bose gas*. In *Proceedings of the 13th Physics Summer School: Bose-Einstein Condensation*, pages 65–116. World scientific, 2000. (Cited on page 110.)
- [97] T. Nikuni and A. Griffin. *Hydrodynamic modes and pulse propagation in a cylindrical Bose gas above the Bose-Einstein transition*. Phys. Rev. A, **58**: 4044–4050, 1998. DOI: [10.1103/PhysRevA.58.4044](https://doi.org/10.1103/PhysRevA.58.4044). (Cited on page 110.)
- [98] T. D. Lee and C. N. Yang. *Low-temperature behavior of a dilute Bose system of hard spheres. II. nonequilibrium properties*. Phys. Rev., **113**: 1406–1413, 1959. DOI: [10.1103/PhysRev.113.1406](https://doi.org/10.1103/PhysRev.113.1406). (Cited on pages 110 and 111.)
- [99] L. D. Landau. *The theory of superfluidity of helium II*. Journal of Physics, **V**: 71–90, 1941. (Cited on page 110.)
- [100] M. R. Andrews, D. M. Stamper-Kurn, H.-J. Miesner, D. S. Durfee, C. G. Townsend, S. Inouye, and W. Ketterle. *Erratum: Propagation of sound in a Bose-Einstein condensate [phys. rev. lett. 79, 553 (1997)]*. Phys. Rev. Lett., **80**: 2967, 1998. DOI: [10.1103/PhysRevLett.80.2967](https://doi.org/10.1103/PhysRevLett.80.2967). (Cited on pages 110, 112, and 118.)
- [101] E. Zaremba. *Sound propagation in a cylindrical Bose-condensed gas*. Phys. Rev. A, **57**: 518–521, 1998. DOI: [10.1103/PhysRevA.57.518](https://doi.org/10.1103/PhysRevA.57.518). (Cited on pages 110 and 112.)
- [102] G. M. Kavoulakis and C. J. Pethick. *Quasi-one-dimensional character of sound propagation in elongated Bose-Einstein condensed clouds*. Phys. Rev. A, **58**: 1563–1566, 1998. DOI: [10.1103/PhysRevA.58.1563](https://doi.org/10.1103/PhysRevA.58.1563). (Cited on pages 110, 112, 116, and 118.)
- [103] S. Stringari. *Dynamics of Bose-Einstein condensed gases in highly deformed traps*. Phys. Rev. A, **58**: 2385–2388, 1998. DOI: [10.1103/PhysRevA.58.2385](https://doi.org/10.1103/PhysRevA.58.2385). (Cited on pages 110, 111, and 112.)
- [104] C. Menotti, M. Krämer, A. Smerzi, L. Pitaevskii, and S. Stringari. *Propagation of sound in a Bose-Einstein condensate in an optical lattice*. Phys. Rev. A, **70**: 023609, 2004. DOI: [10.1103/PhysRevA.70.023609](https://doi.org/10.1103/PhysRevA.70.023609). (Cited on page 110.)

- [105] J. Steinhauer, R. Ozeri, N. Katz, and N. Davidson. *Excitation spectrum of a Bose-Einstein condensate*. Phys. Rev. Lett., **88**: 120407, 2002. DOI: [10.1103/PhysRevLett.88.120407](https://doi.org/10.1103/PhysRevLett.88.120407). (Cited on page 110.)
- [106] J. J. Chang, P. Engels, and M. A. Hofer. *Formation of dispersive shock waves by merging and splitting Bose-Einstein condensates*. Phys. Rev. Lett., **101**: 170404, 2008. DOI: [10.1103/PhysRevLett.101.170404](https://doi.org/10.1103/PhysRevLett.101.170404). (Cited on pages 110, 116, and 125.)
- [107] N. N. Bogoliubov. *On the theory of superfluidity*. J. Phys. USSR, **11**: 23–32, 1947. (Cited on page 111.)
- [108] A. Griffin and E. Zaremba. *First and second sound in a uniform Bose gas*. Phys. Rev. A, **56**: 4839–4844, 1997. DOI: [10.1103/PhysRevA.56.4839](https://doi.org/10.1103/PhysRevA.56.4839). (Cited on pages 112 and 113.)
- [109] S. Burger, K. Bongs, S. Dettmer, W. Ertmer, K. Sengstock, A. Sanpera, G. V. Shlyapnikov, and M. Lewenstein. *Dark solitons in Bose-Einstein condensates*. Phys. Rev. Lett., **83**: 5198–5201, 1999. DOI: [10.1103/PhysRevLett.83.5198](https://doi.org/10.1103/PhysRevLett.83.5198). (Cited on page 123.)
- [110] V. Y. F. Leung, A. G. Truscott, and K. G. H. Baldwin. *Nonlinear atom optics with bright matter-wave soliton trains*. Phys. Rev. A, **66**: 061602, 2002. DOI: [10.1103/PhysRevA.66.061602](https://doi.org/10.1103/PhysRevA.66.061602). (Cited on pages 123 and 124.)
- [111] M. Trippenbach, Y. B. Band, and P. S. Julienne. *Theory of four-wave mixing of matter waves from a Bose-Einstein condensate*. Phys. Rev. A, **62**: 023608, 2000. DOI: [10.1103/PhysRevA.62.023608](https://doi.org/10.1103/PhysRevA.62.023608). (Cited on page 123.)
- [112] N. P. Robins, C. M. Savage, J. J. Hope, J. E. Lye, C. S. Fletcher, S. A. Haine, and J. D. Close. *Fluctuations and flux: The limits of multistate atom lasers*. Phys. Rev. A, **69**: 051602, 2004. DOI: [10.1103/PhysRevA.69.051602](https://doi.org/10.1103/PhysRevA.69.051602). (Cited on page 123.)
- [113] N. P. Robins, A. K. Morrison, J. J. Hope, and J. D. Close. *Limits to the flux of a continuous atom laser*. Phys. Rev. A, **72**: 031606, 2005. DOI: [10.1103/PhysRevA.72.031606](https://doi.org/10.1103/PhysRevA.72.031606). (Cited on page 123.)
- [114] M. Köhl, T. Busch, K. Mølmer, T. W. Hänsch, and T. Esslinger. *Observing the profile of an atom laser beam*. Phys. Rev. A, **72**: 063618, 2005. DOI: [10.1103/PhysRevA.72.063618](https://doi.org/10.1103/PhysRevA.72.063618). (Cited on page 123.)
- [115] A. A. Norrie, R. J. Ballagh, and C. W. Gardiner. *Quantum turbulence and correlations in Bose-Einstein condensate collisions*. Phys. Rev. A, **73**: 043617, 2006. DOI: [10.1103/PhysRevA.73.043617](https://doi.org/10.1103/PhysRevA.73.043617). (Cited on page 123.)

- [116] E. A. Donley, N. R. Claussen, S. L. Cornish, J. L. Roberts, E. A. Cornell, and C. E. Wieman. *Dynamics of collapsing and exploding Bose-Einstein condensates*. *Nature*, **412**: 295–299, 2001. (Cited on page 124.)
- [117] H. Saito and M. Ueda. *Mean-field analysis of collapsing and exploding Bose-Einstein condensates*. *Phys. Rev. A*, **65**: 033624, 2002. DOI: [10.1103/PhysRevA.65.033624](https://doi.org/10.1103/PhysRevA.65.033624). (Cited on page 124.)
- [118] S. K. Adhikari. *Dynamics of collapsing and exploding Bose-Einstein condensate*. *Physics Letters A*, **296**: 145–150, 2002. ISSN 0375-9601. DOI: [DOI: 10.1016/S0375-9601\(02\)00246-3](https://doi.org/10.1016/S0375-9601(02)00246-3). URL: <http://www.sciencedirect.com/science/article/B6TVM-45GKN94-8/2/918222847574d9fdd661d39b6c250223>. (Cited on page 124.)
- [119] L. Santos and G. V. Shlyapnikov. *Collapse dynamics of trapped Bose-Einstein condensates*. *Phys. Rev. A*, **66**: 011602, 2002. DOI: [10.1103/PhysRevA.66.011602](https://doi.org/10.1103/PhysRevA.66.011602). (Cited on page 124.)
- [120] S. Wüster, J. J. Hope, and C. M. Savage. *Collapsing Bose-Einstein condensates beyond the Gross-Pitaevskii approximation*. *Phys. Rev. A*, **71**: 033604, 2005. DOI: [10.1103/PhysRevA.71.033604](https://doi.org/10.1103/PhysRevA.71.033604). (Cited on page 124.)
- [121] S. Wüster, B. J. Dąbrowska-Wüster, A. S. Bradley, M. J. Davis, P. Blair Blakie, J. J. Hope, and C. M. Savage. *Quantum depletion of collapsing Bose-Einstein condensates*. *Phys. Rev. A*, **75**: 043611, 2007. DOI: [10.1103/PhysRevA.75.043611](https://doi.org/10.1103/PhysRevA.75.043611). (Cited on page 124.)
- [122] S. L. Cornish, S. T. Thompson, and C. E. Wieman. *Formation of bright matter-wave solitons during the collapse of attractive Bose-Einstein condensates*. *Phys. Rev. Lett.*, **96**: 170401, 2006. DOI: [10.1103/PhysRevLett.96.170401](https://doi.org/10.1103/PhysRevLett.96.170401). (Cited on page 124.)
- [123] B. J. Dąbrowska-Wüster, S. Wüster, and M. J. Davis. *Dynamical formation and interaction of bright solitary waves and solitons in the collapse of Bose-Einstein condensates with attractive interactions*. arXiv:0812.0493v1, 2008. (Cited on page 124.)
- [124] K. E. Strecker, G. B. Partridge, A. G. Truscott, and R. G. Hulet. *Formation and propagation of matter-wave soliton trains*. *Nature*, **417**: 150–153, 2002. DOI: [10.1038/nature747](https://doi.org/10.1038/nature747). URL: <http://dx.doi.org/10.1038/nature747>. (Cited on page 124.)
- [125] L. Khaykovich, F. Schreck, G. Ferrari, T. Bourdel, J. Cubizolles, L. D. Carr, Y. Castin, and C. Salomon. *Formation of a matter-wave bright soliton*. *Science*, **296**: 1290–1293, 2002. DOI: [10.1126/science.1071021](https://doi.org/10.1126/science.1071021). URL: <http://www.sciencemag.org/cgi/content/abstract/296/5571/1290>. (Cited on page 124.)

- [126] B. Damski. *Formation of shock waves in a Bose-Einstein condensate*. Phys. Rev. A, **69**: 043610, 2004. DOI: [10.1103/PhysRevA.69.043610](https://doi.org/10.1103/PhysRevA.69.043610). (Cited on pages [124](#) and [130](#).)
- [127] Z. Dutton, M. Budde, C. Slowe, and L. V. Hau. *Observation of quantum shock waves created with ultra-compressed slow light pulses in a Bose-Einstein condensate*. Science, **293**: 663–668, 2001. DOI: [10.1126/science.1062527](https://doi.org/10.1126/science.1062527). URL: <http://www.sciencemag.org/cgi/content/abstract/293/5530/663>. (Cited on page [124](#).)
- [128] T. P. Simula, P. Engels, I. Coddington, V. Schweikhard, E. A. Cornell, and R. J. Ballagh. *Observations on sound propagation in rapidly rotating Bose-Einstein condensates*. Phys. Rev. Lett., **94**: 080404, 2005. DOI: [10.1103/PhysRevLett.94.080404](https://doi.org/10.1103/PhysRevLett.94.080404). (Cited on page [125](#).)
- [129] M. A. Hoefer, M. J. Ablowitz, I. Coddington, E. A. Cornell, P. Engels, and V. Schweikhard. *Dispersive and classical shock waves in Bose-Einstein condensates and gas dynamics*. Phys. Rev. A, **74**: 023623, 2006. DOI: [10.1103/PhysRevA.74.023623](https://doi.org/10.1103/PhysRevA.74.023623). (Cited on page [125](#).)
- [130] M. A. Hoefer, M. J. Ablowitz, and P. Engels. *Piston dispersive shock wave problem*. Phys. Rev. Lett., **100**: 084504, 2008. DOI: [10.1103/PhysRevLett.100.084504](https://doi.org/10.1103/PhysRevLett.100.084504). (Cited on page [125](#).)
- [131] Y. Castin and R. Dum. *Bose-Einstein condensates in time dependent traps*. Phys. Rev. Lett., **77**: 5315–5319, 1996. DOI: [10.1103/PhysRevLett.77.5315](https://doi.org/10.1103/PhysRevLett.77.5315). (Cited on page [132](#).)

LIST OF PUBLICATIONS

This thesis is based on the following articles

- R. Meppelink, R. A. Rozendaal, S. B. Koller, and P. van der Straten, *Phase contrast imaging of Bose-Einstein condensed clouds*. Phys. Rev. A, (submitted, 2009). (Chapter 3)
- R. Meppelink, R. van Rooij, J. M. Vogels, and P. van der Straten, *Enhanced heat flow in the hydrodynamic-collisionless regime*. Phys. Rev. Lett. **103**: 095301, 2009. (Chapter 5)
- R. Meppelink, S. B. Koller, J. M. Vogels, H. T. C. Stoof, and P. van der Straten, *Second sound dipole mode in a partially Bose-Einstein condensed gas*. Phys. Rev. Lett., (submitted, 2009). (Chapter 7)
- R. Meppelink, S. B. Koller, and P. van der Straten, *Sound propagation in a Bose-Einstein condensate at finite temperatures*. Phys. Rev. A, (accepted, 2009). (Chapter 8)
- R. Meppelink, S. B. Koller, J. M. Vogels and P. van der Straten, E. D. van Ooijen, N. R. Heckenberg, H. Rubinsztein-Dunlop, S. A. Haine and M. J. Davis, *Observation of shock waves in a large Bose-Einstein condensate*. Phys. Rev. A, (accepted, 2009). (Chapter 9)

Other articles to which the author has contributed

- K. M. R. van der Stam, A. Kuijk, R. Meppelink, J. M. Vogels, and P. van der Straten. *Spin-polarizing cold sodium atoms in a strong magnetic field*. Phys. Rev. A, **73**: 063412, 2006.
- K. M. R. van der Stam, E. D. van Ooijen, R. Meppelink, J. M. Vogels, and P. van der Straten. *Large atom number Bose-Einstein condensate of sodium*. Review of Scientific Instruments, **78**: 013102, 2007.
- K. M. R. van der Stam, R. Meppelink, J. M. Vogels, and P. van der Straten. *Reaching the hydrodynamic regime in a Bose-Einstein condensate by suppression of avalanches*. Phys. Rev. A, **75**: 031602, 2007.

LIST OF CONFERENCE CONTRIBUTIONS

List of oral presentations

- R. Meppelink, S. B. Koller, R. van Rooij, J. M. Vogels and P. van der Straten, *Heat conduction in an ultra-cold quantum gas*. 31st Meeting of the section atomic molecular and optical physics (AMO), Lunteren, April 4, 2007.
- R. Meppelink, S. B. Koller, J. M. Vogels and P. van der Straten, *Excitations of Bose-Einstein condensates in anisotropic thermal clouds*. Physics@FOM, Veldhoven, January 22, 2008.
- R. Meppelink, S. B. Koller, J. M. Vogels and P. van der Straten, *Hydrodynamic excitations in a Bose-Einstein condensate*. 32nd Meeting of the section atomic molecular and optical physics (AMO), Lunteren, October 28, 2008.

List of poster presentations

- R. Meppelink, K. M. R. van der Stam, J. M. Vogels and P. van der Straten, *Large sodium Bose-Einstein condensates*. Achievements and perspectives of cold molecules, EU training school and workshop, Les Houches (France), February 27 to March 3, 2006.
- R. Meppelink, K. M. R. van der Stam, S. B. Koller, R. van Rooij, R. Rozendaal, J. M. Vogels and P. van der Straten, *Reaching the hydrodynamic regime in a Bose-Einstein condensate by suppression of avalanches*. FOM-meeting Physics@Veldhoven 2007, Veldhoven, January 23, 2007.
- R. Meppelink, S. B. Koller, J. M. Vogels and P. van der Straten, *Hydrodynamic excitations in a Bose-Einstein condensate*. XXI international conference on atomic physics (ICAP 2008), Storrs (USA), July 31, 2008.
- R. Meppelink, S. B. Koller, J. M. Vogels and P. van der Straten, *Hydrodynamic excitations in a Bose-Einstein condensate*. Physics@FOM, Veldhoven, January 20, 2009.

SAMENVATTING IN HET NEDERLANDS

LAGE TEMPERATUREN

De moleculen in de lucht tussen de lezer en deze pagina bewegen met ongeveer 300 meter per seconde, drie keer sneller dan een raceauto. De temperatuur van de lucht hangt af van de snelheid van de moleculen. Hoe langzamer ze bewegen des te lager is de temperatuur. Langzamer dan stilstaan kan echter niet en dat betekent dat er een ondergrens aan de temperatuur is. De temperatuur waarbij de moleculen stilstaan is $-273,15^{\circ}\text{C}$. Deze temperatuur wordt het absolute nulpunt genoemd. In de wetenschap wordt gebruik gemaakt van een absolute temperatuurschaal, uitgedrukt in Kelvin (K), waarbij 0 K gelijk is aan $-273,15^{\circ}\text{C}$. Op deze absolute temperatuurschaal smelt ijs bij 273,15 K.

LASERKOELEN

Met behulp van lasers kunnen atomen worden afgeremd. In dit onderzoek werken wij met natriumatomen. De laserkoeltechniek werkt als volgt: een atoom in een laserbundel kan fotonen ("lichtdeeltjes") absorberen, waarbij het foton het atoom "een duwtje" geeft. Door een laserbundel tegen de bewegingsrichting van het atoom in te sturen kan het worden afgeremd. Het atoom wordt dus gekoeld. Het atoom zendt het geabsorbeerde foton vervolgens in een willekeurige richting uit en het atoom is weer beschikbaar om een nieuw foton te absorberen. Ondanks het zeer kleine duwtje van het foton is een atoom met deze techniek nagenoeg tot stilstand te brengen, doordat het atoom door heel veel fotonen geraakt kan worden. Een beeldende analogie is het afremmen van een vrachtwagen met behulp van een tennisballen-kanon. Als je genoeg tennisballen op de vrachtwagen afschiet zal die uiteindelijk tot stilstand komen. Een laser wordt dus gebruikt als een soort 'fotonen-kanon' voor de atomen.

Met behulp van magneetvelden kunnen de sterk vertraagde atomen vervolgens gevangen worden in een zogenoemde magneto-optische val. Uiteindelijk bewegen de gevangen atomen met enkele centimeters per seconde, ruwweg de snelheid van een mug.

BOSE-EINSTEIN CONDENSATIE

In 1925 kwam Wolfgang Pauli met een theorie die zegt dat twee elektronen niet tegelijkertijd dezelfde kwantumtoestand kunnen bezetten. De verklaring daarvoor

blijkt verband te houden met de ontdekking dat de elektronen als het ware om hun as draaien: ze hebben een 'spin'. De allerkleinste deeltjes waar materie uit is opgebouwd blijken te verdelen te zijn in twee groepen: deeltjes waarvan de spin *half-tallig* is (bijvoorbeeld $1/2$ of $3/2$) en deeltjes waarvan de spin heel-tallig (bijvoorbeeld 0 of 1) is. Deeltjes met *half-tallige* spin, *fermionen* genoemd, kunnen niet gelijktijdig in dezelfde kwantumtoestand zijn. De elektronen die Pauli bestudeerde zijn dus *fermionen*. Deeltjes met *heel-tallige* spin, *bosonen* genoemd, kunnen – in tegenstelling tot fermionen – wel dezelfde kwantummechanische toestand bezetten.

In datzelfde jaar voorspelde Albert Einstein, geïnspireerd door ideeën van Satyendra Nath Bose, de statistische eigenschappen van *bosonen*. Daaruit blijkt dat er bij voldoende lage temperatuur iets heel bijzonders gebeurt: zodra een *boson* in de kwantummechanische grondtoestand terecht komt zal een aanzienlijk deel van de overige *bosonen* daar ook terecht komen. Wanneer dat gebeurt spreekt men van een *Bose-Einstein condensaat* of afgekort een *BEC*. Aangezien sommige atomen – afhankelijk van hun interne opbouw – *bosonen* zijn, kan er Bose-Einstein condensatie optreden in een atoomwolk.

De lezer zou zich ondertussen kunnen afvragen wat het verband is tussen Bose-Einstein condensatie en laserkoelen. Om een Bose-Einstein condensaat te laten ontstaan zijn erg lage temperaturen nodig. Dat komt door het kwantummechanische karakter van atomen. Bij lage temperaturen is het niet correct het atoom te zien als een deeltje, maar moet het gezien worden als een golf. Bij voldoende lage temperatuur wordt de golflengte van het atoom groter dan de afstand tussen de atomen. De golven overlappen en hun afzonderlijke golven worden één enkele golf die voor alle atomen hetzelfde is: er ontstaat een Bose-Einstein condensaat. Een van de meest bijzondere eigenschappen van een Bose-Einstein condensaat is dat alle atomen "met elkaar in de pas lopen". Ze oscilleren samen, als één geheel. Dit wordt ook wel *coherent gedrag* genoemd.

De atomen die gevangen zijn in de magneto-optische val blijken nog lang niet koud genoeg te zijn om Bose-Einstein condensatie op te laten treden. Dat heeft onder meer te maken met het duwtje dat de fotonen de atomen blijven geven, waardoor de atomen nooit helemaal stilgezet kunnen worden. Om nog lagere temperaturen te behalen moet een techniek gebruikt worden die werkt zonder laserlicht. De atomen worden overgeladen naar een volledig magnetische val. Vervolgens vindt er koeling plaats door de atomen met de hoogste snelheden uit deze val te laten ontsnappen. De resterende atomen hebben gemiddeld een lagere snelheid en dus een lagere temperatuur. Indien de atomen onderling voldoende vaak botsen leidt dat zo nu en dan tot atomen die bijna stilstaan, waarbij de energie is overgedragen op andere atomen. De atomen met de hoogste snelheden kunnen vervolgens uit de val ontsnappen. Deze procedure herhaalt zich vele malen en is equivalent aan het afkoelen van een kop koffie. Dit proces is dusdanig efficiënt dat de temperatuur verlaagd kan worden tot $1\ \mu\text{K}$ (een miljoenste graad

Kelvin, oftewel 0,000 001 K). Pas bij deze lage temperatuur vindt Bose-Einstein condensatie plaats. Hoe dicht dat bij het absolute nulpunt is kan inzichtelijk gemaakt worden door de temperatuurschaal van 0 K tot aan kamertemperatuur te vergelijken met een stuk touw met de lengte van de omtrek van de aarde. Dat touw is dan 40 074 km lang. De temperatuur waarbij Bose-Einstein condensatie optreedt komt overeen met een afstand van slechts 15 cm vanaf het beginpunt van dit touw.

IJLE ATOOMWOLKEN EN VLOEIBAAR HELIUM

Ondanks de voorspelling van Bose en Einstein in 1925 dat er condensatie optreedt in een ijle atoomwolk bij voldoende lage temperatuur duurde het nog 70 jaar voordat de voorspelling experimenteel geïnterpreteerd kon worden. In 1995 lukte het de groep van Cornell en Wieman van het NIST-JILA laboratorium om een wolk rubidiumatomen voldoende af te koelen om een Bose-Einstein condensaat waar te nemen bij een temperatuur van 0,17 μ K. Bijna gelijktijdig slaagde de groep van Ketterle bij het MIT erin een Bose-Einstein condensaat te maken in een wolk natriumatomen bij 2 μ K. In 2001 kregen Cornell, Wieman en Ketterle de Nobelprijs voor de natuurkunde “voor het bereiken van Bose-Einstein condensatie in ijle alkali atoomwolken, en voor de eerste fundamentele onderzoeken naar de eigenschappen van de condensaten”. Deze experimentele prestatie kon worden geleverd dankzij de technieken die vanaf 1970 ontwikkeld zijn om neutrale atomen te koelen met behulp van lasers. Een mijlpaal werd in 1982 bereikt met het aantonen van de magneto-optische val. In 1997 werd de Nobelprijs voor de natuurkunde toegekend aan Chu, Cohen-Tannoudji en Phillips “voor het ontwikkelen van methoden om atomen te koelen en vangen met behulp van laserlicht”. Dankzij deze technieken is de initiële dichtheid van de atomen hoog genoeg om aan de voorwaarde voor efficiënt verdampingskoelen te voldoen: voldoende thermaliserende botsingen.

In een vloeistof bleek het effect van Bose-Einstein condensatie echter al enkele jaren na de voorspelling van Bose en Einstein waargenomen te zijn, alhoewel de verschijnselen pas later als Bose-Einstein condensatie werden geïnterpreteerd. Zo ontdekten zowel Kapitsa als Keesom in 1938 dat vloeibaar helium bij voldoende lage temperatuur, 2,17 K, supervloeibaar wordt. Bij supervloeibaarheid (superfluiditeit) kent een vloeistof helemaal geen wrijving en verliest het elke viscositeit. Het sijpelt door de smalste spleetjes heen en kruipt zelfs tegen de wanden op van het vat waarin het wordt bewaard. Wetenschappers ontdekten niet lang daarna dat de supervloeibaarheid het gevolg is van Bose-Einstein condensatie.

In supervloeibaar helium blijft – afhankelijk van de temperatuur – een gedeelte van de vloeistof een normale, viskeuze vloeistof. De normale en supervloeibare component hebben een onderlinge wisselwerking en dat zorgt voor bijzondere verschijnselen die belangrijk zijn geweest voor het ontwikkelen en toetsen van

(kwantummechanische) theorieën. Door de sterke interacties in vloeibaar helium is het echter niet goed mogelijk deze verschijnselen volledig te verklaren. Dat heeft er onder meer mee te maken dat door de sterke interacties maximaal ongeveer 10% van de vloeistof Bose-Einstein condenseert. Daarnaast blijkt het onmogelijk te zijn het condensaat in vloeibaar helium rechtstreeks waar te nemen. Om die reden zochten wetenschappers naar mogelijkheden om Bose-Einstein condensatie te bereiken in ijle gassen, waar de interacties zwak zijn. In Bose-Einstein condensaten van ijle atoomwolken kunnen de gecondenseerde fractie en de niet-gecondenseerde fractie eenvoudig van elkaar worden onderscheiden. Daarnaast is het mogelijk nagenoeg 100% van de wolk te condenseren. Met het bereiken van Bose-Einstein condensatie in atoomwolken in 1995 is het mogelijk geworden experimenten uit te voeren waarin de interactie tussen de gecondenseerde fractie en de niet-gecondenseerde fractie rechtstreeks bestudeerd wordt. Zulke metingen kunnen onze kennis van kwantummechanische verschijnselen als supervloeibaarheid verdiepen en waarschijnlijk openstaande vragen uit het onderzoek met supervloeibaar helium beantwoorden.

Bose-Einstein condensaten van atoomwolken zijn ondertussen al veelvuldig gebruikt om het dynamische gedrag van een (supervloeibaar) Bose-Einstein condensaat te bestuderen. De meeste van deze metingen vinden plaats bij temperaturen waarbij nagenoeg alle atomen van de atoomwolk Bose-Einstein gecondenseerd zijn: een bijna puur condensaat. Bij hogere temperaturen zijn er ook atomen die niet gecondenseerd zijn. Deze atomen maken deel uit van de zogenoemde *thermische wolk*. Het blijkt dat in het overgrote deel van de experimenten de thermische wolk in het *botsingsloze regime* is: de dichtheid is zo laag dat botsingen een verwaarloosbaar effect hebben op bijvoorbeeld het warmtetransport of de geluidsvoortplanting in de atoomwolk. De thermische wolk heeft dan geen vloeistofachtige eigenschappen. Dat is jammer, omdat een systeem met een supervloeistof en een normale vloeistof – zoals dat bij supervloeibaar helium voorkomt – niet kan worden bereikt. Om de gaswolk meer het gedrag van een vloeistof te laten hebben zijn er veel meer botsingen nodig.

Het regime waarin botsingen een prominente rol spelen wordt het *hydrodynamische regime* genoemd. In het hydrodynamische regime is de afstand die een atoom aflegt tussen twee botsingen, de *vrije weglengte*, veel kleiner dan de afmeting van de atoomwolk. Daardoor wordt het gedrag van de wolk sterk bepaald door de botsingen. Dit regime is nog maar nauwelijks bestudeerd, doordat er bij de hoge dichtheden die nodig zijn om in het hydrodynamische regime te komen verliezen optreden door molecuulvorming. De dichtheid kan daardoor niet te veel worden verhoogd. Het verliesproces leidt in een hydrodynamische wolk tevens tot botsingslawines, waardoor de dichtheid van de wolk nog verder beperkt wordt. Hierdoor wordt het hydrodynamische regime meestal niet bereikt en blijft de thermische wolk in het botsingsloze regime.

Wij zijn erin geslaagd om toch het hydrodynamische regime te bereiken door gebruik te maken van een groot aantal atomen en door te werken met een zeer langgerekte, sigaarvormige val. Door de vorm van de val blijft de dichtheid, en dus de verliezen door molecuulvorming én botsingslawines, beperkt. De wolk heeft bij deze dichtheden een afmeting in de lange richting die vele malen de vrije weglengte van de atomen is. De wolk is daardoor alsnog hydrodynamisch in deze richting. In de andere richtingen heeft de wolk een lengte die veel kleiner is dan de vrije weglengte van de atomen en gedraagt de wolk zich dus nagenoeg botsingsloos. Dat is belangrijk om verlies door botsingslawines te voorkomen.

In de experimenten die wij uitvoeren en die beschreven zijn in dit proefschrift bestuderen wij zo veel mogelijk verschijnselen langs de lange, hydrodynamische as van de wolk, maar we onderzoeken ook hoe het hydrodynamisch-botsingsloze regime verschilt van het volledig hydrodynamische regime. Door de verliesprocessen te onderdrukken hebben wij op het moment van schrijven van dit proefschrift met 300 miljoen gecondenseerde atomen per condensaat tevens het grootste Bose-Einstein condensaat ter wereld, als we condensaten gemaakt met cryogene technieken buiten beschouwing laten.

DIT PROEFSCHRIFT

De metingen die in dit proefschrift beschreven zijn laten het gedrag van een natrium Bose-Einstein condensaat zien in het nauwelijks ontgonnen hydrodynamische regime. Na een inleiding is in **Hoofdstuk 2** de opstelling beschreven die gebruikt is om het hydrodynamische regime te bereiken. In 2004 werd met deze opstelling voor het eerst een Bose-Einstein condensaat waargenomen. De weg naar het bereiken van Bose-Einstein condensatie begint met vast natrium dat in een oventje in het vacuüm verhit wordt tot ongeveer 600 K. De damp wordt door middel van twee diafragma's gecollimeerd tot een atoombundel en komt dan in een *Zeeman slower* terecht. Daar wordt de bundel afgeremd tot ongeveer 30 m/s, voldoende traag om een magneto-optische val mee te laden. Uiteindelijk worden er ongeveer 300 miljard atomen gevangen in de magneto-optische val. Vervolgens worden de atomen overgeladen in een magneetval. Door de hoge overlaad efficiëntie bereiken we een hoge initiële dichtheid in de magneetval en kan de gaswolk zeer efficiënt worden gekoeld met behulp van verdampingskoelen. We bereiken de Bose-Einstein condensatietemperatuur $T_c \approx 1 \mu\text{K}$ met ongeveer een miljard atomen. Het grote aantal koude atomen stelt ons in staat de magneetval sterk te decomprimeren, waardoor we kunnen werken met zeer langgerekte, sigaarvormige atoomwolken. De condensaten worden met het typische aantal atomen in een dergelijke val enkele millimeters lang in de ene richting, en tientallen micrometers lang in de andere richtingen. De vrije weglengte is ongeveer 100 keer groter dan de lange as van de wolk en het hydrodynamische regime is bereikt in de thermische wolk in deze richting. Door nog verder te koelen kunnen

we nagenoeg pure condensaten maken die ruwweg 300 miljoen atomen bevatten. Daarnaast leidt een groot aantal atomen tot een goede signaal/ruis verhouding in de metingen en stabiele condensaten, dag in, dag uit.

Atoomwolken kunnen worden afgebeeld door de schaduw die de wolk veroorzaakt in een laserbundel te registreren op een CCD camera. Deze methode is door verschillende oorzaken niet heel erg nauwkeurig, maximaal ongeveer 20 % in het aantal gecondenseerde atomen, zoals beschreven is in **Hoofdstuk 3**. Een alternatieve methode die in dat hoofdstuk beschreven wordt om koude atoomwolken af te beelden, *phase contrast imaging*, blijkt veel nauwkeuriger te zijn. Met behulp van deze methode kunnen wij het aantal gecondenseerde atomen met een nauwkeurigheid van 5 % bepalen. Daarnaast biedt onze implementatie van deze methode de mogelijkheid de statische interactie tussen de gecondenseerde en niet-gecondenseerde atomen waar te nemen én te vergelijken met verschillende modellen die deze interacties beschrijven.

Naast de statische interacties beïnvloedt de wisselwerking tussen de gecondenseerde en de niet-gecondenseerde atomen de dynamica van gedeeltelijk gecondenseerde wolken, met name als de thermische wolk hydrodynamisch is. In **Hoofdstuk 4** is de dynamica bestudeerd aan de hand van een collectieve excitatie van de wolk: de *quadrupole* modus. We exciteren deze modus zowel boven als onder de Bose-Einstein condensatietemperatuur T_c . Boven T_c , waar we dus alleen een thermische wolk bestuderen, is de *quadrupole* modus een gevoelige maat voor het hydrodynamische gedrag van de wolk. We vergelijken onze metingen met eerder werk uit Amsterdam en tonen aan dat het hydrodynamische regime bereikt is. Door de temperatuur te laten dalen tot onder T_c kunnen we de *quadrupole* modus bestuderen in de aanwezigheid van zowel een condensaat als een hydrodynamische thermische wolk. We concluderen dat de wolk zich nóg meer hydrodynamisch gedraagt zodra een condensaat gevormd is, hetgeen in overeenstemming is met een theoretische beschrijving van de relevante botsingsprocessen. Dit hoofdstuk wordt besloten met een meer exotische excitatie die als een neveneffect van een te sterke excitatie van de *quadrupole* modus kan worden waargenomen.

In **Hoofdstuk 5** is de warmtegeleiding in een atoomwolk boven T_c bij ongeveer 1 μK bestudeerd. Deze wolk is hydrodynamisch langs de lange as en botsingsloos langs de korte assen. De atoomwolk wordt plaatselijk verwarmd en de propagatie van de temperatuurverhoging langs de lange as van de wolk wordt gemeten. Het resultaat is de observatie en identificatie van twee nieuwe, hydrodynamische, modi in de atoomwolk. De eerste modus zorgt voor het warmtetransport. In dit zogenaamd *hydrodynamisch-botsingsloze* regime blijkt het warmtetransport een factor vijf groter te zijn dan de theoretische voorspelling voor een wolk die hydrodynamisch is in alle richtingen. Deze verhoging kan deels worden verklaard door de aanwezigheid van atomen met een groot impulsmoment. Deze atomen spiraliseren om de wolk heen, waar ze nagenoeg botsingsloos bewegen. Het

gevolg is dat deze atomen een zeer grote bijdrage leveren aan het warmtetransport. De tweede modus is geïdentificeerd als het resultaat van een staande geluidsgolf en is de eerste observatie van geluidsvortplanting in koude atoomwolken. Het aantonen van een excessief warmtetransport in het hydrodynamisch-botsingsloze regime heeft belangrijke implicaties voor het maken van een continue atoomlaser. De sterke warmtegeleiding beperkt de koefficiëntie door warmteoverdracht tussen het ongekoelde deel en het reeds gekoelde deel van de atoombundel.

Dit onderzoek biedt tevens een belangrijke opmaat voor metingen onder de condensatietemperatuur, waarin de interactie tussen het Bose-Einstein condensaat en de hydrodynamische thermische wolk bestudeerd wordt. Deze meting is beschreven in **Hoofdstuk 6** en toont de observatie van een zevental hydrodynamische modi. Bij gebrek aan een complete theorie welke de dynamica in dit gebied beschrijft bepreken wij ons tot het analyseren en identificeren van de verschillende modi. Van al deze modi bepalen wij de oscillatiefrequentie en dempingsconstante. Het is de verwachting dat deze metingen de ontwikkeling van theoretische modellen zal aansporen die van toepassing zijn op dit inhomogene, hydrodynamische *two-fluid* systeem.

In **Hoofdstuk 7** is de *out-of-phase dipole* modus van het condensaat ten opzichte van de thermische wolk bestudeerd. We exciteren daarmee de *second sound dipole* modus, analoog aan *second sound* in supervloeibaar helium. Deze modus bestuderen we als functie van de hydrodynamiciteit en de geometrie van de val. We concluderen dat voorspellingen gebaseerd op het botsingsloze mechanisme *Landau damping* goed overeenkomen met de gemeten dempingsconstanten dicht bij het botsingsloze regime. We meten een sterkere demping in het hydrodynamische regime en schrijven dat toe aan demping door botsingsprocessen. Deze metingen kunnen als proeftuin dienen voor verschillende dempingsmechanismen welke in de literatuur zijn voorgesteld.

Naast excitaties met een golflengte van de orde grootte van de afmeting van de wolk bestuderen we ook excitaties met een kortere golflengte. Zolang de golflengte langer blijft dan de *healing* lengte is de dispersierelatie van een Bose-Einstein condensaat lineair voor deze excitaties en deze planten zich voort met de geluidssnelheid. In **Hoofdstuk 8** is een experiment beschreven waarin deze geluidssnelheid in een Bose-Einstein condensaat bepaald wordt. Aangezien de thermische wolk in het hydrodynamische regime is beschrijven we het systeem met een *two-fluid* model. Onder meer door de gevoelige *phase contrast imaging* methode toe te passen kunnen we een kleine dichtheidsverandering observeren en de voortplantingssnelheid daarvan nauwkeurig bepalen. De voortplantingssnelheid van de dichtheidsgolf wordt gebruikt om de geluidssnelheid te bepalen. De gemeten geluidssnelheid blijkt te worden beïnvloed door de thermische wolk. De geluidssnelheid komt zeer goed overeen met de snelheid van *second sound*, gebaseerd op het *Landau two-fluid* model.

Indien een dergelijke dichtheidsgolf met een grotere amplitude wordt aangeslagen zal de voortplanting sterk niet-lineair worden doordat de geluidssnelheid afhankelijk is van de dichtheid; hoe lager de dichtheid, des te lager is de voortplantingssnelheid. In het geval dat de dichtheidsgolf een dichtheidsdepressie is zal de achterkant van de golf (hoge dichtheid) het midden van de golf (lage dichtheid) “inhalen”. Er ontstaat dan een schokgolf. In het experiment dat beschreven is in **Hoofdstuk 9** slaan we dichtheidsgolven aan met een grote amplitude en bestuderen we de formatie van de schokgolven. We nemen zowel *self steepening* als het opbreken van de golf waar. Als gevolg van het opbreken van de golf ontstaan er *fringes* met een afmeting van de orde grootte van de *healing* lengte. Wij zijn erin geslaagd deze kleine structuren af te beelden en te vergelijken met computersimulaties. Deze simulaties zijn uitgevoerd in samenwerking met de groep van Matthew Davis uit Queensland, Australië. Er is aangetoond dat de Gross-Pitaevskii vergelijking de formatie en voortplanting van schokgolven goed voorspelt.

CURRICULUM VITÆ

Robert Meppelink werd geboren op 6 maart 1979 in het Overijsselse Hengelo. Van 1991 tot en met 1997 doorliep hij het voorbereidend wetenschappelijk onderwijs aan de scholengemeenschap *de Amersfoortse Berg* te Amersfoort.

Daarna startte hij de studie Natuurkunde aan de *Universiteit Utrecht* met keuzevakken in de experimentele natuurkunde en de fysische informatica. Ook liep hij stage op een middelbare school in het kader van een keuzevak bij de β -didactiek sectie. Tijdens zijn afstudeeronderzoek verrichtte hij experimenteel onderzoek naar het optisch vangen van atomen met behulp van een gepulste laser, uitgevoerd bij de vakgroep *Atom Optics & Ultrafast Dynamics* onder begeleiding van drs. Lennart Karssen, prof. dr. Peter van der Straten en prof. dr. Jaap Dijkhuis. In 2005 rondde hij zijn doctoraalscriptie getiteld "*Creating an optical dipole trap*" af en behaalde hij zijn doctoraaldiploma.

Aansluitend begon hij bij dezelfde groep als *Onderzoeker in Opleiding* in dienst bij de stichting *Fundamenteel Onderzoek der Materie*. Onder leiding van prof. dr. Peter van der Straten heeft hij onderzoek gedaan naar de hydrodynamische eigenschappen van een Bose-Einstein condensaat. De resultaten van dat onderzoek zijn in dit proefschrift beschreven. Gedurende het promotieonderzoek begeleidde Robert een tweetal studenten bij hun Masteronderzoek. Verder gaf hij werkcolleges van verschillende vakken binnen zijn vakgroep en begeleidde hij de cursus "*Programmeren in Mathematica*". Ook begeleidde hij middelbare scholieren die het onderzoek voor hun profielwerkstuk invulling gaven bij de *Universiteit Utrecht*.

Naast zijn studie- en onderzoekswerkzaamheden was hij bestuurslid van een studenten-volleybalvereniging, een studenten-tennisvereniging en de vereniging van eigenaars van het appartementencomplex waar hij woont.

DANKWOORD

Voor ik vergeet
en ik de feiten en de cijfers
en de namen van de schrijvers
niet meer weet

(Spinvis)

De Universiteit Utrecht adverteert vaak met de slogan “Wetenschap is nooit af”. Het bijzondere is dat een promotieonderzoek wel een eindige tijd beslaat, maar eigenlijk ook nooit af is. Met het drukken van een proefschrift komt er een definitief einde aan het promotieonderzoek. Het is niet alleen de verdienste van de promovendus dat er op dat moment een grotendeels afgerond onderzoek gepresenteerd kan worden. Op deze plaats wil ik de personen bedanken die belangrijk zijn geweest voor de totstandkoming van dit proefschrift.

Allereerst wil ik mijn promotor Peter van der Straten bedanken. Direct na mijn afstudeeronderzoek gaf je mij de mogelijkheid te promoveren op je BEC-opstelling. Ik wil je bedanken voor het vertrouwen en de vrijheid die je me gaf om zelf voor een belangrijk deel invulling te geven aan het onderzoek. De keuze die je rond het jaar 2000 maakte om al je energie, en ook onderzoeksgeld en mankracht te steken in het maken van een BEC is tekenend voor je durf en doorzettingsvermogen. Ik heb daardoor enkele jaren met een *second generation* BEC-opstelling mogen werken en ben je daar zeer dankbaar voor. Je betrokkenheid bij het onderzoek leidde regelmatig tot de gezamenlijke analyse van de bergen meetgegevens die de opstelling produceerde. Ondanks het harde werken heeft de sfeer er nooit onder geleden. Ook bewaar ik goede herinneringen aan de reis naar de VS voor de ICAP conferentie, en de ontvangst die je daar voor ons hebt geregeld.

Frits Ditewig wil ik bedanken voor de dagelijkse begeleiding. In onze eerste week presteerden we het onze samenwerking zó goed af te stemmen dat jij, met de waterkoeling uit, de beveiliging van de magneetspoelen precies overbrugde op het moment dat ik in een softwaretest stroom door de spoelen liet lopen. De spoelen waren gelukkig net niet helemaal gesmolten. Het vervolg van de samenwerking bleek een stuk constructiever. Zowel met de bestaande als de nieuwe elektronica in het lab is geen noemenswaardig probleem geweest en gezien de enorme hoeveelheid specialistische elektronica die jij in de loop der jaren hebt gemaakt is dat een prestatie van formaat.

Toen ik begon met mijn promotieonderzoek was er kort daarvoor voor het eerst een BEC waargenomen met de opstelling waarmee ik zou gaan werken. Geen

van de resultaten in dit proefschrift zouden behaald zijn zonder het werk van de promovendi Dries van Oosten, Erik van Ooijen en Richard van der Stam. Zij hebben de BEC-opstelling opgebouwd én afgeregeld, zodat het eerste condensaat gemaakt kon worden. Richard wil ik daarnaast bedanken voor het inwerken van mij op de opstelling. Je was in de laatste fase van je promotieonderzoek, maar desondanks gunde je me tijd met de opstelling en stond je me toe enkele verbeteringen door te voeren.

Johnny Vogels wil ik bedanken voor zijn onuitputtelijke enthousiasme en ondersteuning bij het onderzoek. Johnny, je theoretische beschrijving van warmtegeleiding in wolken die maar in één richting hydrodynamisch zijn leidde tot een hoofdstuk in dit proefschrift én een mooie publicatie. Bij de verklaring van veel van mijn metingen speelde je een grote rol en daar ben ik je dankbaar voor.

Tijdens mijn promotieonderzoek heb ik twee studenten begeleid bij hun Masteronderzoek. Roel, je hebt mooi werk verricht aan *phase contrast imaging* en je werk ligt aan de basis van Hoofdstuk 3 van dit proefschrift. Daarnaast heb je een belangrijke stap gezet in de optimalisatie van de koude atoomflux. Rob, jou werk aan thermische geleiding ligt aan de basis van Hoofdstuk 5 van dit proefschrift. Ook is het door jou opgezette laservermogen-stabilisatiesysteem zeer belangrijk gebleken voor de metingen die in dit proefschrift beschreven zijn. Heren, jullie inbreng in het lab leidde niet alleen tot mooie resultaten, maar ook tot een prima sfeer. Mijn dank is groot.

Silvio wil ik bedanken voor zijn enorme inzet in het lab tijdens de laatste jaren van mijn promotieonderzoek. Je precisie-uitlijning van *phase contrast imaging* heeft afbeeldingen van koude wolken opgeleverd die waarschijnlijk nergens ter wereld zo mooi gemaakt zouden zijn. Ik hoop dat je de komende tijd je ambitieuze en interessante metingen succesvol af kunt ronden en onze mooie opstelling door kunt geven aan een volgende generatie promovendi. Ik wil je daar succes bij wensen.

Lennart, vanaf het eerste moment dat ik mijn afstudeeronderzoek begon dat jij als OIO begeleidde, heb je mij enthousiast gemaakt voor het *koude atomen* vakgebied. Als onderdeel van de illustere *groep Karssen*, die in haar hoogtijdagen uit wel vijf mensen bestond, heb je me in korte tijd kennis laten maken met alles wat nodig is om een wolk rubidiumatomen te vangen. Ook bracht je mijn *Linux* kennis op een veel hoger niveau. Het nadeel van jou als collega blijkt pas als je een dankwoord schrijft. In elke fase van je promotieonderzoek heb je mij (en vele anderen) geholpen met \LaTeX , *IDL*, het maken van *Makefiles* en het instellen van de juiste parameters voor proefschriftwaardige plaatjes. Met zoveel verdiensten is de ruimte hier te kort voor bijvoorbeeld mooie verhalen over gezamenlijk bezochte conferenties. Wel wil ik je op deze plaats bedanken voor het nauwkeurig doorlezen van een groot deel van mijn manuscript. Daarnaast ben ik vereerd dat je mijn paranimef wil zijn. Peter van Capel was kamergenoot van mij en Lennart tijdens mijn afstudeeronderzoek. Ik wil hem bedanken voor

alle gesprekken over natuurkunde en heel veel andere zaken. Heren, bedankt voor de geweldige tijd!

Peter van Capel, Otto, Lennart en ik vermaakten ons in bepaalde periodes en in wisselende samenstelling met het spelen van tafeltennis. Daarbij introduceerden Peter en ik benamingen voor verschillende slagtechnieken zoals *de Otto*, *de Lennart* en *de Dries*. Literatuuronderzoek in recente proefschriften van onze vakgroep kan inzicht geven in het waardeoordeel dat uit deze benamingen spreekt.

Paul Jurrius wil ik bedanken voor de gezelligheid, de altijd uitgestoken hand en de technische ondersteuning. Paul begrijpt vlekkeloos dat je iets altijd al *vorige week* nodig had, zodra je hem vraagt iets voor je te maken. Zijn oplossingen blijken altijd doeltreffend en zijn er mede de oorzaak van dat ik mijn tijd in het lab optimaal heb kunnen gebruiken. Cees de Kok wil ik bedanken voor het bewaren van allerlei kleurstoflaser-onderdelen. In de loop der jaren heb ik aan deze lasers dusdanig veel moeten versleutelen dat de voorraad én expertise van Cees me enorm hebben geholpen. Voor ondersteuning met de kleurstoflaser ben ik ook Hans Wisman dank verschuldigd.

Jaap Dijkhuis, professor bij “de andere helft” van de vakgroep wil ik bedanken voor zijn enorme enthousiasme en interesse in het BEC onderzoek. Henk Stoof wil ik bedanken voor het inzicht dat hij mij heeft gegeven in de theoretische aspecten van veel van onze experimenten. Verschillende oud-collega’s, collega’s en studenten die nog niet eerder genoemd zijn, waaronder Michiel, Driss, Shan, Dmitry T., Dmitry M., Marijn, Louise, Erik, Lynn, Tim en Radjien bedank ik voor de goede samenwerking.

Promoveren kost een hoop tijd. Gelukkig blijft er genoeg tijd over om andere leuke dingen in te doen. Vele concerten (Joeri, Sam, Rianne), wintersport in landen als Turkije en Andorra (Joeri). Maar ook volleyballen en tennissen, met dank aan mijn teams voor het begrip bij alle keren dat ik bijna op tijd kwam. Wetenschap is nooit af. . . . Sam wil ik bedanken voor de interesse in mijn onderzoek en de goede vriendschap. Martijn bedank ik voor de vele keren eten, de muziek en de goede verhalen. Erg leuk dat je mijn paranimf wil zijn.

De grootste dank gaat uit naar mijn ouders. Gert en Rita, jullie steun, opvoeding en interesse in alles wat ik doe hebben mij in staat gesteld alle stappen te nemen die uiteindelijk tot dit proefschrift hebben geleid. Ik kan mij geen betere ouders voorstellen.

Rianne, de laatste regels van een proefschrift zijn traditiegetrouw voor de persoon die de promovendus het dierbaarst is. Jij hebt me vaak moeten delen met mijn onderzoek. Je steun, interesse en begrip zijn erg belangrijk voor me en hebben me in staat gesteld het onderzoek tot een goed einde te brengen. Lieve Rianne, ik ben blij en gelukkig dat ik met jou aan mijn zijde promoveer!

COLOPHON

This thesis was typeset with $\LaTeX 2_{\epsilon}$ using André Miede's ClassicThesis package (available for \LaTeX via CTAN as "`classicthesis`"), with many customizations by L. C. Karssen and the author. The PDF version was generated using pdf \LaTeX .

The figures were made with Interactive Data Language (IDL), Inkscape, and POV-Ray using routines written by the author. Bib \TeX was used to generate the bibliography. The cover was designed in Adobe's Illustrator CS4 by Maarten Overeem. The photo on the front cover was taken by Ivar Pel in 2008 and features the author working on the Spectra-Physics 380D dye laser. The images on the back cover are those of the propagation of a thermal wave in partly Bose-Einstein condensed hydrodynamic cloud, shown in Fig. 6.2 on page 86.

The manuscript was digitally printed by PrintPartners Ipskamp, Enschede.